The Astrophysical Journal, 708:868–908, 2010 January 1 doi:10.1088/0004-637X/708/1/868

THE LAST EIGHT-BILLION YEARS OF INTERGALACTIC C IV EVOLUTION

Kathy L. Cooksey[1,4], Christopher Thom[2], J. Xavier Prochaska[1,3], and Hsiao-Wen Chen[2,5]
[1] Department of Astronomy, University of California, 1156 High Street, Santa Cruz, CA 95064, USA; kcooksey@space.mit.edu
[2] Department of Astronomy, University of Chicago, 5640 S. Ellis Avenue, Chicago, IL 60637, USA; cthom@stsci.edu, hchen@oddjob.uchicago.edu
[3] UCO/Lick Observatory, University of California, 1156 High Street, Santa Cruz, CA 95064, USA; xavier@ucolick.org
Received 2009 June 17; accepted 2009 November 18; published 2009 December 15

ABSTRACT

We surveyed the *Hubble Space Telescope* UV spectra of 49 low-redshift quasars for $z < 1$ C IV candidates, relying solely on the characteristic wavelength separation of the doublet. After consideration of the defining traits of C IV doublets (e.g., consistent line profiles, other associated transitions, etc.), we defined a sample of 38 definite (group G = 1) and five likely (G = 2) doublets with rest equivalent widths W_r for both lines detected at $\geqslant 3\sigma_{W_r}$. We conducted Monte Carlo completeness tests to measure the unblocked redshift (Δz) and co-moving path length (ΔX) over which we were sensitive to C IV doublets of a range of equivalent widths and column densities. The absorber line density of (G = 1+2) doublets is $d\mathcal{N}_{\rm C\,IV}/dX = 4.1^{+0.7}_{-0.6}$ for $\log N(\rm C^{+3}) \geqslant 13.2$, and $d\mathcal{N}_{\rm C\,IV}/dX$ has not evolved significantly since $z = 5$. The best-fit power law to the G = 1 frequency distribution of column densities $f(N(\rm C^{+3})) \equiv k(N(\rm C^{+3})/N_0)^{\alpha_N}$ has coefficient $k = 0.67^{+0.18}_{-0.16} \times 10^{-14}\,\rm cm^2$ and exponent $\alpha_N = -1.50^{+0.17}_{-0.19}$, where $N_0 = 10^{14}\,\rm cm^{-2}$. Using the power-law model of $f(N(\rm C^{+3}))$, we measured the $\rm C^{+3}$ mass density relative to the critical density: $\Omega_{\rm C^{+3}} = (6.20^{+1.82}_{-1.52}) \times 10^{-8}$ for $13 \leqslant \log N(\rm C^{+3}) \leqslant 15$. This value is a 2.8 ± 0.7 increase in $\Omega_{\rm C^{+3}}$ compared to the error-weighted mean from several $1 < z < 5$ surveys for C IV absorbers. A simple linear regression to $\Omega_{\rm C^{+3}}$ over the age of the universe indicates that $\Omega_{\rm C^{+3}}$ has slowly but steadily increased from $z = 5 \rightarrow 0$, with $d\Omega_{\rm C^{+3}}/dt_{\rm age} = (0.42 \pm 0.2) \times 10^{-8}\,\rm Gyr^{-1}$.

Key words: intergalactic medium – quasars: absorption lines – techniques: spectroscopic

Online-only material: color figures, machine-readable tables

1. INTRODUCTION

With the inception of echelle spectrometers on 10 m class optical telescopes, observers unexpectedly discovered that a significant fraction of the $z > 1.5$ intergalactic medium (IGM; a.k.a. the Lyα forest) was enriched (Cowie et al. 1995; Tytler et al. 1995). The C IV absorption lines have proven to be valuable transitions for studying the enrichment of the IGM since: (1) their rest wavelengths $\lambda\lambda$1548.20, 1550.77 Å are redward of Lyα λ1215.67 Å; (2) they redshift into the optical for $z_{1548} \gtrsim 1.5$; (3) they constitute a doublet with characteristic rest wavelength separation (2.575 Å or 498 km s^{-1}); and (4) have an equivalent width ratio 2:1 for $W_{r,1548} : W_{r,1550}$ in the unsaturated regime.

Quantitative studies based on the C IV doublet measured the enrichment level to be $\approx 10^{-2}$ to 10^{-4} the chemical abundance of the Sun over the range $1.8 \lesssim z \lesssim 5$ (Songaila 2001; Boksenberg et al. 2003; Schaye et al. 2003). No viable model of Big Bang nucleosynthesis can explain this observed level of enrichment; therefore, the metals observed have been produced in stars and transported to the Lyα forest. The mechanisms typically invoked include "primary" enrichment by some of the earliest stars at $z > 6$ (e.g., Madau et al. 2001; Wise & Abel 2008) or "contemporary" injection through galactic feedback processes from $z \approx 6 \rightarrow 2$ (e.g., Scannapieco et al. 2002; Oppenheimer & Davé 2006).

Numerous high-redshift surveys have shown that the mass density of triply ionized carbon relative to the critical density of the universe $\Omega_{\rm C^{+3}} = \rho_{\rm C^{+3}}/\rho_{c,0}$ has *not* evolved substantially from $z = 5$ (≈1 Gyr after the Big Bang) to $z = 1.5$ (≈4 Gyr; e.g., Songaila 2001; Boksenberg et al. 2003; Pettini et al. 2003; Schaye et al. 2003; Songaila 2005). The studies used a variety of techniques, from traditional absorption line surveys (e.g., Songaila 2001; Boksenberg et al. 2003), where hundreds of C IV doublets were analyzed, to variants on the pixel optical depth (POD) method (e.g., Schaye et al. 2003; Songaila 2005), which statistically correlate the amount of flux absorbed to the C IV mass density. Songaila (2001) pioneered modern $\Omega_{\rm C^{+3}}$ studies, and her results for the range $1.5 < z < 5$ have been confirmed by subsequent surveys: $1.6 \times 10^{-8} \lesssim \Omega_{\rm C^{+3}} \lesssim 3 \times 10^{-8}$. (We adjust all $\Omega_{\rm C^{+3}}$ values quoted in this paper to our adopted cosmology: $H_0 = 70\,\rm km\,s^{-1}\,Mpc$, $\Omega_{\rm M} = 0.3$, and $\Omega_\Lambda = 0.7$ and to sample doublets with $13 \leqslant \log N(\rm C^{+3}) \leqslant 15$; see Appendix C for more details.)

Recent studies have focused on increasing the statistics of C IV absorption at $z > 5$, where Songaila (2001) only detected one absorber. These studies had to await the development of near-infrared spectrographs and the discovery of $z \approx 6$ QSOs. With only one or two sightlines, Ryan-Weber et al. (2006) and Simcoe (2006), respectively, measured the $5.4 \lesssim z \lesssim 6.2$ C IV mass density to be consistent with the previous $1.5 < z < 5$ surveys. However, the most recent work by Ryan-Weber et al. (2009) and Becker et al. (2009) observed that $\Omega_{\rm C^{+3}}$ at $5.2 \lesssim z \lesssim 6.2$ is a factor of ≈4 smaller than $\Omega_{\rm C^{+3}}$ at $z < 5$. Although these two studies included two to three times as many sightlines as Simcoe (2006), the results are based on $\lesssim$3 detected C IV doublets. Obviously, the small number statistics at $z > 5$ leave the $\Omega_{\rm C^{+3}}$ measurements more susceptible to cosmic variance.

Cosmological hydrodynamic simulations have been used to understand the interplay between metallicity, feedback, the ionizing background, etc., and the evolution of $\Omega_{\rm C^{+3}}$.

[4] Current address: Department of Physics, Massachusetts Institute of Technology, 77 Massachusetts Avenue, Cambridge, MA 02139, USA.
[5] Current address: Space Telescope Science Institute, 3700 San Martin Dr., Baltimore, MD 21218, USA.

Aguirre et al. (2001) and Springel & Hernquist (2003) argued that most of the metals observed in the IGM were distributed by galactic winds at $3 \leqslant z \leqslant 10$, and observations at $z \approx 2.5$ offer empirical support (e.g., Simcoe et al. 2004). Oppenheimer & Davé (2006) evolved cosmological hydrodynamic simulations from $z = 6 \rightarrow 2$ with a range of prescriptions for galactic winds that enrich the IGM. They found that the increasing cosmic metallicity from $z = 5 \rightarrow 2$ balanced the decreasing fraction of carbon traced by the C IV transition (i.e., changing ionization state of the IGM). Thus, they neatly reproduced the observed lack of $\Omega_{C^{+3}}$ evolution. In their momentum-driven winds simulation (their favored "*vzw*" model), $\Omega_{C^{+3}}$ increased from $z = 6 \rightarrow 5$, consistent with the measurements available at the time (Songaila 2001; Ryan-Weber et al. 2006; Simcoe 2006) and with the more recent results (Ryan-Weber et al. 2009; Becker et al. 2009).

In Oppenheimer & Davé (2008), the authors included feedback from asymptotic giant branch (AGB) stars, in addition to a new method for deriving the velocity dispersion, σ, of galaxies, which defined the momentum-driven wind speed. They compared the evolution of $\Omega_{C^{+3}}$ from $z = 2 \rightarrow 0$ in the simulations with the old and new σ-derived winds with AGB feedback and the new σ-derived winds without AGB feedback. In all three simulations, $\Omega_{C^{+3}}$ did not evolve from $z = 3 \rightarrow 1$ (2–6 Gyr after the Big Bang). In the simulation with the new σ-derived winds and AGB feedback, $\Omega_{C^{+3}}$ increased by 70% from $z = 1 \rightarrow 0$—to $\Omega_{C^{+3}} \approx 7 \times 10^{-8}$—over the last 8 Gyr of the cosmic enrichment cycle. The AGB feedback increased the star formation rate, which increased the mass of carbon in the IGM. This predicted increase in $\Omega_{C^{+3}}$ at $z < 1$ can and should be tested by empirical observation.

The C IV mass density at $z < 1.5$ has not been studied as extensively as at high redshift, where the C IV doublet is redshifted into optical passbands. At low redshift, ultraviolet spectrographs on space-based telescopes are required. Recent studies (e.g., Frye et al. 2003; Danforth & Shull 2008) have leveraged high-resolution, UV echelle spectra to examine the low-redshift IGM: the *Hubble Space Telescope* Space Telescope Imaging Spectrograph and Goddard High-Resolution Spectrograph (*HST* STIS and GHRS, respectively), supplemented by spectra from the *Far Ultraviolet Spectrograph Explorer* (*FUSE*). Through an analysis of nine quasar sightlines observed with the STIS E140M grating, Frye et al. (2003) found six C IV doublets and measured $\Omega_{C^{+3}} \approx 12 \times 10^{-8}$ for $z < 0.1$ from a preliminary analysis. With an expanded survey of 28 sightlines with E140M spectra, Danforth & Shull (2008) detected 24 C IV doublets in 28 sightlines and measured $\Omega_{C^{+3}} = (7.8 \pm 1.5) \times 10^{-8}$ for $z < 0.12$. These low-redshift $\Omega_{C^{+3}}$ measurements are consistent with that predicted by the σ-derived winds with AGB feedback simulation of Oppenheimer & Davé (2008).

These initial studies focused on C IV absorbers at $z \lesssim 0.1$ and did not present comprehensive analysis of their survey completeness, nor did they take advantage of the full set of *HST* archival data. There are currently 69 sightlines in the *HST* archives with UV spectra, where the C IV doublet can be detected at $z < 1$. We have conducted a large survey for C IV systems in these sightlines. We analyzed the $z < 1$ data in a consistent fashion, which allowed for a uniform comparison throughout the eight-billion year interval. We introduced robust search algorithms and constrained the frequency distribution $f(N(C^{+3}))$ for the full sample. Finally, we compared our results with the other low- and high-redshift surveys, focusing on the evolution of $\Omega_{C^{+3}}$.

This paper is organized as follows: we present the spectra, the reduction procedures, and the measurements in Section 2; our sample selection is described in Section 3; Section 4 outlines the completeness tests; we analyze the frequency distribution and the C IV mass density in Section 5; the final discussion is provided in Section 6; and Section 7 is a summary.

2. DATA, REDUCTION, AND MEASUREMENTS

To assemble our target list, we searched the *HST* STIS and GHRS spectroscopic archives for objects with target descriptions including the terms, e.g., QSO, quasar, Seyfert, etc. Our final list included 69 objects with redshifts $0.001 < z_{em} < 2.8$. We retrieved all available spectra from the Multimission Archive at Space Telescope[6] (MAST), including supplementary *FUSE* data, when available (see Table 1[7]). We reduced (in the case of the *FUSE* spectra), co-added, and normalized the spectra with similar algorithms as described in Cooksey et al. (2008). The reduced *HST* spectra were retrieved from MAST directly.

One goal of this study was to search the *entire HST* archive for C IV absorption; thus, we initially included the full archival data set. However, we excluded targets that only had un-normalized spectra with signal-to-noise ratio (S/N) $< 2\,\mathrm{pixel}^{-1}$. The S/N was measured by fitting a Gaussian to the histogram of flux f_λ and noise σ_{f_λ} per pixel, clipping the highest and lowest outliers and demanding $f_\lambda > 0$. Ten sightlines do not meet the S/N criterion: QJ0640–5031; TON34; HE1104–1805A; HE1122–1648; NGC4395; Q1331+170; IR2121–1757; HDFS–223338–603329-QSO; AKN564; and PG2302+029. They are indicated by "Exclude (low S/N)" in Table 1. Q1331+170 has a damped Lyα system, with molecular hydrogen lines, at $z = 1.7765$ (Cui et al. 2005) that made the E230M spectra exceptionally difficult to analyze.[8] Therefore, Q1331+170 was also excluded, though it had $\mathrm{S/N} = 5\,\mathrm{pixel}^{-1}$.

In addition, we excluded the spectra for which higher-resolution spectra covered the same wavelength range (noted as "Exclude (overlap)" in Table 1). Typically, we excluded spectra with resolution $R < 20{,}000$ (FWHM $> 15\,\mathrm{km\,s}^{-1}$). There were 10 targets that had no C IV coverage, given the spectral wavelength range and z_{em}: Q0026+1259, TONS180, PKS0558–504, PG1004+130, HE1029+140, Q1230+0947, PG1307+085, MARK290, Q1553+113, and PKS2005-489.

Ultimately, 49 targets had spectra with usable wavelength coverage and S/N ratios. All reduced, co-added, and normalized spectra are available online,[9] even those not explicitly searched in this paper. The number of spectra covering the C IV doublet redshift range is shown schematically in Figure 1.

2.1. HST STIS and GHRS

The *HST* spectra drive the target selection because its UV instruments, STIS and GHRS, have the wavelength coverage to detect C IV in the $z < 1$ universe. We preferred higher-resolution data over lower-resolution data to resolve the C IV doublets and better distinguish them from coincident Lyα features. The STIS

[6] See http://archive.stsci.edu/.

[7] We have adopted the target name that MAST used. So note: B0312–770 is also PKS0312–770; QSO–123050+011522 is also Q1230–0115; and PHL1811 is also known as FJ2155–092.

[8] Q1331+170 also had a known Mg II system at $z = 0.7450$ (Ellison et al. 2003), which likely had blended C IV absorption.

[9] See http://www.ucolick.org/~xavier/HSTCIV/ for the normalized spectra, the continuum fits, the C IV candidate lists, and the Monte Carlo completeness limits for all sightlines as well as the completeness test results for the full data sample.

Table 1
Observation Summary

(1) Target	(2) R.A. (J2000)	(3) Decl. (J2000)	(4) z_{em}	(5) Instr.	(6) Grating	(7) R (FWHM) (km s^{-1})	(8) S/N (pix^{-1})	(9) λ_{min} (Å)	(10) λ_{max} (Å)	(11) t_{exp} (ks)	(12) PID	(13) Notes
MRK335	00:06:19	+20:12:10	0.0258	STIS	E140M	45800 (7)	7	1141	1710	17	9802	
				GHRS	G160M	20000 (15)	34	1222	1258	15	3584	
				FUSE	LWRS	20000 (15)	$\leqslant 10$	904	1188	99	P101	
Q0026+1259	00:29:13	+13:16:04	0.1450	GHRS	G270M	20000 (15)	5	2785	2831	5	3755	Exclude (coverage)
				FUSE	LWRS	20000 (15)	$\leqslant 2$	904	1188	20	Q206	
TONS180	00:57:20	–22:22:56	0.0620	STIS	G140M	12700 (24)	25	1244	1298	3	7345	Exclude (coverage)
					G230MB	9450 (32)	9	2758	2912	1	9128	Exclude (coverage)
				FUSE	LWRS	20000 (15)	$\leqslant 5$	904	1188	25	D028; P101	
PG0117+213	01:20:17	+21:33:46	1.4930	STIS	E230M	30000 (10)	8	2278	3072	42	8673	
TONS210	01:21:51	–28:20:57	0.1160	STIS	E140M	45800 (7)	6	1141	1710	22	9415	
					E230M	30000 (10)	4	1988	2782	5	9415	
					G230MB	9450 (32)	0	2759	2913	2	9128	Exclude (*R*)
				FUSE	LWRS	20000 (15)	$\leqslant 8$	904	1188	53	P107	

Notes. The targets and spectra are included in the current survey. The targets, their coordinates, and their redshifts are listed in Columns 1–4. The instrument and grating of the archived observations (Columns 5 and 6) are listed with the resolution R (and FWHM in km s^{-1}), exposure time t_{exp}, and the proposal identification number (PID) from the MAST query (Columns 7, 11, and 12). The signal-to-noise ratio (S/N) was measured from the normalized spectra (Column 8). Columns 9 and 10 are the wavelength coverage of each spectrum. The status of the spectra (i.e., whether it was excluded and why) is listed in Column 13.

(This table is available in its entirety in a machine-readable form in the online journal. A portion is shown here for guidance regarding its form and content.)

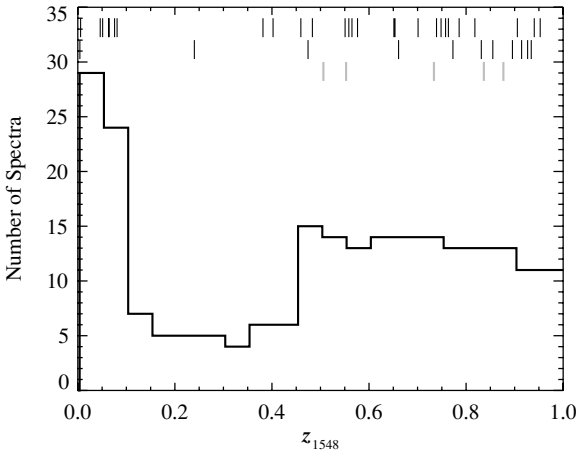

Figure 1. Schematic of redshift coverage for the current survey. The number of spectra with coverage of the C IV doublet is shown as a function of z_{1548}, the redshift of the 1548 line (black histogram). The STIS E140M spectra covered $z_{1548} \lesssim 0.1$. The STIS E230M spectra typically covered $0.4 \lesssim z_{1548} < 1$. The redshift range $0.1 \lesssim z_{1548} \lesssim 0.4$ was covered by some E230M spectra as well as the medium-resolution gratings and GHRS spectra. The redshifts of the doublets detected with $W_r \geqslant 3\sigma_{W_r}$ in both lines are shown with the hashes across the top. The top and middle rows indicate the redshifts of the 27 unsaturated (top) and 11 saturated (middle) doublets in the definite group (G = 1; see Section 3.3). The bottom row shows the redshift of the five unsaturated likely (G = 2) doublets.

echelle gratings were the preferred set-up in most cases, since they were high resolution and covered a large wavelength range.

All STIS observations were reduced with CalSTIS 2.23 on UT 2006 October 6 with On-the-Fly Reprocessing and co-added with XIDL[10] COADSTIS (Cooksey et al. 2008). The STIS long-slit spectra were co-added by re-binning the individual exposures to the same wavelength array and then combining the error-weighted flux. For the echelle data, the observations for each order were co-added separately, in the same manner as the long-slit spectra. Then all of the orders were co-added into a single spectrum.

The STIS echelle gratings E140M and E230M contributed the most to the total path length of this survey. All 49 targets have at least one echelle spectrum. The E140M grating covered the wavelength range 1140 Å $\lesssim \lambda \lesssim$ 1710 Å or $z_{1548} \lesssim 0.1$ and had a resolution of $R = 45{,}000$ (FWHM = 7 km s^{-1}). The E230M grating covered ≈800 Å per tilt over the range 1570 Å $\lesssim \lambda \lesssim$ 3110 Å or $z_{1548} \lesssim 1$. Typically, the observations covered 2280 Å $\lesssim \lambda \lesssim$ 3070 Å or $0.5 \lesssim z_{1548} \lesssim 1$. The E230M grating had resolution $R = 30{,}000$ (10 km s^{-1}). The only other STIS gratings included in the C IV search were G140M and G230M, which have wavelength coverage similar to E140M and E230M, respectively, albeit with less total coverage. For more information about STIS, see Mobasher (2002).

The calibrated GHRS spectra were retrieved from MAST. They were co-added like the STIS long-slit spectra. Observations with central wavelengths that varied by less than 5% of the total wavelength coverage of that grating were co-added into a single spectrum. This avoided the problem of automatic scaling to the highest-S/N spectrum.

The GHRS ECH-A, ECH-B, G160M, G200M, and G270M gratings were used in the final C IV search. The ECH-A and ECH-B gratings had resolution $R = 100{,}000$ (FWHM = 3 km s^{-1}). The G160M, G200M, and G270M gratings had resolution $R = 20{,}000$ (15 km s^{-1}). We excluded all GHRS spectra where there existed STIS coverage since, in general, the STIS data have higher resolution and larger wavelength coverage. For more information about GHRS, see Brandt et al. (1994).

2.2. *Far Ultraviolet Spectroscopic Explorer*

The raw *FUSE* observations were retrieved from MAST. We reduced the spectra with a modified CalFUSE[11] version 3.2 pipeline (see Cooksey et al. 2008). To summarize, the partially

[10] See http://www.ucolick.org/~xavier/IDL/.

[11] See ftp://fuse.pha.jhu.edu/fuseftp/calfuse/.

processed data from the exposures (i.e., intermediate data file or IDF) were combined before the extraction window centroid was determined. Then, the bad pixel masks were generated, and the spectra were optimally extracted.

The observations were co-added with FUSE_REGISTER. The *FUSE* wavelength solutions were *not* shifted to match the STIS wavelength solution. The *FUSE* observations were only searched for absorption lines (e.g., Lyβ, C III, O VI) to supplement candidate C IV systems. The blind doublet search made allowance for offsets in redshift, due to multi-phase absorbers or misaligned wavelength solutions, when it assigned additional absorption lines to the candidate C IV systems (see Section 3.1 for more details).

We excluded *FUSE* spectra with S/N too low for continuum fitting: TON28, NGC4395, QSO–123050+011522, Q1230+0947, NGC5548, PG1444+407, and PG1718+481.

2.3. Continuum Fitting

The continuum for each spectrum was fit semi-automatically with a B-spline. "Semi-automatically" refers to the subjective nature of continuum fitting. The best B-spline was based on the input parameters, primarily, the low- and high-sigma clips and the breakpoint spacing. However, the authors varied these parameters until they agreed the "best" B-spline was a good match to unabsorbed regions.

The breakpoint spacing was typically ≈4–6 Å. The breakpoint spacing was refined to increase in regions where the flux was not varying substantially and to decrease in regions where it was. Regions of great variation were determined by comparing the median flux of each bin to the mean variance-weighted flux of all bins, where the bins are determined by the initial breakpoint spacing. If the difference between the median flux in a bin and the mean flux were more than one standard deviation of the flux bins, the breakpoint spacing was decreased. For most spectra, the low- and high-sigma clips were 2σ and 2.5σ, respectively. The regions masked out by the sigma clipping were increased by 2 pixels on both sides.

The B-spline was iteratively fit to the variance-weighted flux in the bins, with the clipped regions masked out, until the percent difference across the continuum fit was less than 0.001% compared to the previous (converged). For several spectra (e.g., the NGC galaxies), the semi-automatic continuum fit was adjusted by hand.

As mentioned previously, the "best-fit" continuum was a subjective judgment. Several, slightly different continuum fits would have satisfied the authors. To gauge the systematic error introduced by the subjective nature of continuum fitting, we measured the differences due to changing the continuum from the semi-automatic fit to one generated "by hand" for one sightline (see Cooksey et al. 2008). The root-mean-square fractional difference in the observed equivalent width and column density were $\lesssim$10%.

2.4. Redshift, Equivalent Width, and Column Densities

We measured redshifts from the optical depth-weighted central wavelengths; equivalent widths from simple boxcar summation; and column densities from the apparent optical depth method (AODM; Savage & Sembach 1991). To minimize the effect of spurious, outlying pixels on the measurements, the flux was trimmed: $-\sigma_{f_\lambda} \leqslant f_\lambda \leqslant 1 + \sigma_{f_\lambda}$. Outlying flux pixels were set to the appropriate extrema. The trimming affected measurements in the lowest S/N regions of the spectra, typically the edges. It also assisted the identification of absorption lines in the noisy regions by the automated feature search (see Section 3.1), from which the candidate C IV doublets were drawn. When the final C IV sample was defined and the wavelength bounds visually confirmed or changed, this flux trimming had negligible effect. For optical depth measurements, the minimum flux was set, so that: $f_\lambda \geqslant (0.2\sigma_{f_\lambda} > 0.05)$. This prevented the optical depth, $\tau = \ln(1/f_\lambda)$, from being overwhelmingly large for the saturated pixels. These cases were then reported as lower limits to $N(C^{+3})$.

We measured redshifts from the mean optical depth-weighted central wavelengths of the absorption lines and the rest wavelength λ_r of the transition. The wavelengths per pixel λ_i were weighted by their optical depth per pixel $\tau_i = \ln(1/f_{\lambda i})$ within the bounds of the absorption line, defined by the wavelength range: $\lambda_l \leqslant \lambda_i \leqslant \lambda_h$. Thus, the pixels with the strongest absorption dominated the redshift estimate:

$$1 + z_{\rm abs} = \frac{\sum_{\lambda_l}^{\lambda_h} \lambda_i \ln\left(\frac{1}{f_{\lambda i}}\right)}{\lambda_r \sum_{\lambda_l}^{\lambda_h} \ln\left(\frac{1}{f_{\lambda i}}\right)}. \quad (1)$$

The rest equivalent width W_r were measured with a boxcar summation over the wavelength bounds of the feature:

$$W_r = \frac{1}{(1+z_{\rm abs})} \sum_{\lambda_l}^{\lambda_h} (1 - f_{\lambda i}) \delta\lambda_i \quad (2)$$

$$\sigma^2_{W_r} = \frac{1}{(1+z_{\rm abs})^2} \sum_{\lambda_l}^{\lambda_h} {\sigma_{f_\lambda i}}^2 \delta\lambda_i^2,$$

where $\delta\lambda_i$ (Å) is the wavelength pixel scale of the spectrum. The second equation is the variance of the W_r measurement from error propagation. The observed equivalent width $W_{\rm obs}$ and error $\sigma_{W_{\rm obs}}$ were measured with the previous equations but without the $1 + z_{\rm abs}$ factor.

Most of the column densities were measured with the apparent optical depth method (AODM; Savage & Sembach 1991):

$$N_{\rm AOD} = \frac{10^{14.5762}}{f_{\rm osc}\lambda_r} \sum_{\lambda_l}^{\lambda_h} \ln\left(\frac{1}{f_{\lambda i}}\right) \delta v_{\lambda,i} \ ({\rm cm}^{-2}) \quad (3)$$

$$\sigma^2_{N_{\rm AOD}} = \left(\frac{10^{14.5762}}{f_{\rm osc}\lambda_r}\right)^2 \sum_{\lambda_l}^{\lambda_h} \left(\frac{\sigma_{f_\lambda i}}{f_{\lambda i}} \delta v_{\lambda,i}\right)^2 ({\rm cm}^{-4})$$

$$\delta v_{\lambda,i} = c\left(\frac{\delta\lambda_i}{\lambda_r(1+z_{\rm abs})}\right),$$

where $f_{\rm osc}$ (unitless) is the oscillator strength of the transition with rest wavelength λ_r (Å) and $\delta v_{\lambda,i}({\rm km\,s^{-1}})$ is the velocity pixel scale of the spectrum. The atomic data and sources are tabulated in Prochaska et al. (2004). The AOD profiles were used as a diagnostic (see Section 3.2) and were constructed from the unsummed versions of the above equations, smoothed over 3 pixels (see Figure 2).

In some cases, only a column density limit could be set, when the AODM resulted in a measurement $N_{\rm AOD} < 3\sigma_{N_{\rm AOD}}$ (resulting in an upper limit) or the line was saturated (lower limit). In low-S/N spectra, some lines satisfied both criteria

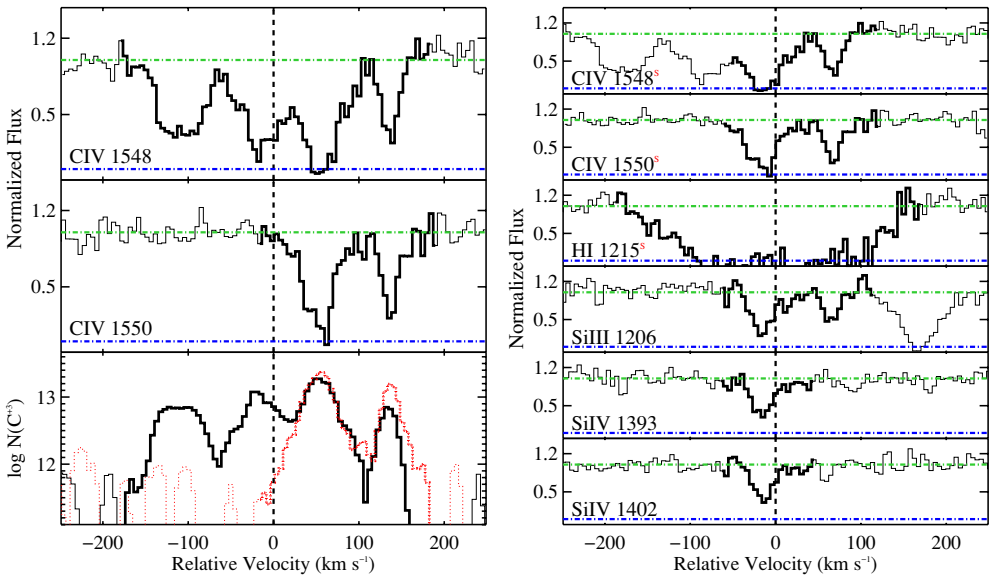

Figure 2. Example of an initial *candidate* C IV doublet and the final $z_{1548} = 0.91440$ system in the PG1630+377 sightline. Two automatically detected absorption features were paired as a candidate C IV doublet based on their wavelength separation (left panel). The wavelength bounds of the candidate 1550 line were expanded to match the range defined by the candidate 1548 line. Several automatically detected features were added to the candidate C IV system as common transitions, based on their observed wavelengths and the redshift of the candidate 1548 line. Finally, we visually inspected the candidate, deemed it a definite system, and modified the transitions and wavelength bounds (right panel). The bottom panel on the left shows the AOD profile of the 1548 and 1550 lines (black solid and red dotted lines, respectively; see Section 3.2). For a description of the velocity plots, see Figure 3.

(A color version of this figure is available in the online journal.)

(e.g., $z_{1548} = 0.40227$ doublet in the PKS0454–22 sightline). In which case, we counted the line as an estimate of the upper limit if $W_r < 3\,\sigma_{W_r}$ and as a lower limit otherwise. Since the column density from the AODM was a poor measurement in the aforementioned instances, we estimated the column density by assuming the W_r reflects the column density from the linear portion of the curve of growth (COG). Then, we use whichever column density measurement resulted in the more extreme limit. For example, if the COG column density was lower than the AODM column density for a saturated, $\geqslant 3\sigma_{W_r}$ feature, the COG column density was used.

For analyses pertaining to the equivalent width, we used $W_{r,1548}$ from the C IV 1548 line. For analyses relating to the column density $N(C^{+3})$ we either used the error-weighted average of N_{1548} and N_{1550} when both were measurements or constrained the value based on the limits of the two doublet lines. The greater lower limit (or the smaller upper limit) was used. In a few cases, N_{1548} and N_{1550} constrained a $N(C^{+3})$ range (see the bracketed values in Table 5). For the column density analyses, we took the average of the limits and used the difference between the average and the values as the errors. For the $z_{1548} = 0.38152$ C IV doublet in the PKS0454–22 sightline, the two line limits did not overlap; we increased/decreased the limits by 1σ to constrain $N(C^{+3})$.

For several sightlines (e.g., the *FUSE* spectra or the two E230M grating tilts for PG1634+706), there were overlapping spectra. We quote measurements from the spectrum where W_r was measured with the higher estimated significance W_r/σ_{W_r}.

3. SAMPLE SELECTION

We conducted a "blind" survey for C IV doublets, where candidate C IV absorbers and any associated lines were identified exclusively by the characteristic wavelength separation of the C IV doublet and the measured redshift of the C IV 1548 line. This eliminated any bias associated with identifying Lyα absorbers first and then searching for associated C IV doublets. Also, for several sightlines, we did not have the wavelength coverage to search for Lyα. Though C IV systems frequently show strong Lyα absorption (Ellison et al. 1999; Simcoe et al. 2004), C IV systems with weak Lyα absorption do occur (Schaye et al. 2007), and they might occur with higher frequency at $z < 1$ if the IGM is more highly enriched. Once we searched for the candidate C IV doublets, we used other diagnostics (see Section 3.2) and visual inspection to define our final sample.

3.1. Automatic Line Detection and Blind Doublet Search

First, we searched for absorption features[12] with observed equivalent widths $W_{\rm obs} \geqslant 3\,\sigma_{W_{\rm obs}}$ with an automated procedure (Cooksey et al. 2008). We convolved the flux with a Gaussian with width equal to the FWHM of the instrument to yield f_G. Then, adjacent convolved pixels with significance $\geqslant 1\sigma_{f_G}$ were grouped into absorption features. The observed equivalent width for all features were measured with the boxcar extraction window defined by the wavelength limits, λ_l and λ_h. The final product was a list of candidate absorption features with $W_{\rm obs} \geqslant 3\,\sigma_{W_{\rm obs}}$, defined by their flux decrement-weighted wavelength centroid and wavelength limits.

Weighting with the flux decrement $1 - f_\lambda$, where $f_\lambda < 1$, was better behaved than weighting with the optical depth $\tau = \ln(1/f_\lambda)$. For strong absorption lines, the two weighting methods result in comparable values. However, for weak absorption lines and noisy absorption features, the flux decrement-weighted centroid was closer to the central wavelength, as defined by the bounds $\lambda_l \leqslant \lambda \leqslant \lambda_h$.

There was no attempt to separate blends at this level. This method automatically recovered nearly all of the features we

[12] We refer to absorption "features" to indicate the results from the automated feature-finding program, which also returned absorption line-like artifacts in the spectrum (e.g., regions with poor continuum fit, multiple pixels with spuriously low flux) in addition to real absorption *lines*.

Table 2
C IV Candidates Summary

(1) z_{1548}	(2) $\delta v_{\rm abs}$ (km s^{-1})	(3) λ_r (Å)	(4) λ_l (Å)	(5) λ_h (Å)	(6) W_r (mÅ)	(7) σ_{W_r} (mÅ)	(8) log N	(9) $\sigma_{\log N}$	(10) Flag
MRK335 ($z_{\rm em} = 0.026$)									
−0.00162	...	1548.19	1545.33	1545.97	<48	...	<13.09	...	157
	−11.7	1550.77	1547.90	1548.54	286	21	>14.39	...	
−0.00092	...	1548.19	1546.49	1547.03	153	20	13.72	0.07	335
	−18.0	1550.77	1549.06	1549.61	<59	...	<13.50	...	
0.00000	...	1548.19	1547.90	1548.54	286	21	>14.09	...	495
	4.2	1550.77	1550.47	1551.12	183	31	14.15	0.09	
PG0117+213 ($z_{\rm em} = 1.493$)									
0.47166	...	1548.19	2278.01	2278.98	691	78	>14.23[a]	...	288
	3.7	1550.77	2281.80	2282.77	<119	...	<13.94	...	
0.47372	...	1548.19	2280.33	2282.56	<191	...	<0.30	...	128
	−23.5	1550.77	2284.12	2286.36	544	73	>14.66	...	
0.47605	...	1548.19	2283.79	2286.36	522	79	>14.35	...	386
	−50.0	1550.77	2287.59	2290.16	978	71	>15.05	...	

Notes. Summary of C IV doublet candidates by target and redshift of C IV 1548. Upper limits are 2σ limits for both W_r and log N. The binary flag is described in Table 3 and Section 3.2.

[a] log N measured by assuming W_r results from the linear portion of the COG.

(This table is available in its entirety in a machine-readable form in the online journal. A portion is shown here for guidance regarding its form and content.)

would have identified visually, but it was not sensitive to broad, shallow features, i.e., $b \gtrsim 50\,{\rm km\,s^{-1}}$. However, Rauch et al. (1996) measured the distribution of Doppler parameters of C IV doublets at high redshift to be $5\,{\rm km\,s^{-1}} \leqslant b \leqslant 20\,{\rm km\,s^{-1}}$. This gives us reason to expect that our algorithms would miss very few (if any) systems.

The automatically detected features were paired into candidate C IV doublets based purely on the characteristic wavelength separation (2.575 Å or 498 km s^{-1} in the rest frame). Every feature with $\lambda_{\rm cent}$ between λ_{1548} and $\lambda_{1548}(1 + z_{\rm em})$ was assumed to be C IV 1548 absorption.[13] If there were an automatically detected feature between the wavelength limits (λ_l, λ_h) at the location of the C IV 1550 line, it was assumed to be C IV 1550 absorption (see Figure 2). Otherwise, the region that would have included C IV 1550 was used to give an estimate of the upper limit of the column density and equivalent width. The C IV 1550 region was set by the wavelength bounds of C IV 1548:

$$\lambda_{l,1550} = \lambda_{l,1548}\left(\frac{\lambda_{r,1550}}{\lambda_{r,1548}}\right) \qquad (4)$$
$$\lambda_{h,1550} = \lambda_{h,1548}\left(\frac{\lambda_{r,1550}}{\lambda_{r,1548}}\right).$$

Similarly, the wavelength bounds of the candidate doublet were adjusted so that they were aligned (e.g., $v_{l,1548} = v_{l,1550}$).

The doublet search was then performed in reverse, where automatically detected features were assumed to be C IV 1550 lines, if not already included. The corresponding region for the C IV 1548 absorption yielded an estimate for the upper limit of the column density and equivalent width.

Automatically detected features at the expected locations, defined by the redshift of the C IV 1548 lines, of several common transitions were added to the candidate C IV systems. The common transitions were: Lyα; Lyβ; C III 977; O VI 1031, 1037; Si II 1260; Si III 1206; Si IV 1393, 1402; N III 989; and N V 1238, 1242. If there were no automatically detected candidate Lyα absorption, the region where the Lyα line would have been was included as an estimate of the upper limit of the column density and equivalent width, if the wavelength coverage existed.

There were some automatically detected features with $\lambda_{1548} \leqslant \lambda \leqslant \lambda_{1548}(1 + z_{\rm em})$ that were more than 498 km s^{-1} wide, which is the characteristic separation of the C IV doublet. For example, there is a damped Lyα system in the spectrum of PG1206+459 at $z_{\rm abs} = 0.92677$, which has a strong, multi-component C IV doublet that is 633 km s^{-1} wide, and the doublet lines 1548 and 1550 are blended with each other (see Appendix A). These cases were visually evaluated and included as candidate C IV doublets, since no automated attempt was made to separate blended absorption features. The search for common transitions then proceeded as described previously.

Finally, the redshifts, rest equivalent widths, column densities, and errors were measured for all transitions in the candidate C IV systems (see Section 2.4). The measured quantities for the candidate doublets are listed in Table 2.

3.2. Machine-generated Diagnostics

We assembled several thousand candidate C IV systems by the process described in the previous section. We then used machine-generated diagnostics to assist in identifying the true C IV systems visually. The candidate systems were assigned flags based on nine criteria that leveraged our knowledge of the C IV doublet and other desirable characteristics (see Table 3). The criteria were the following: C IV 1548 and 1550 had $W_r \geqslant 3\,\sigma_{W_r}$ (flags = 256 and 128, respectively); the W_r ratio of 1548 to 1550 was between 1:1 and 2:1, accounting for the error (64, see Equation (5)); the redshifts of the doublet lines were within 10 km s^{-1} (32, see Equation (6)); there was a candidate Lyα absorber detected with $W_r \geqslant 3\,\sigma_{W_r}$ (16); C IV 1548 was outside the Lyα and the H_2 forest (8 and 4, respectively); the apparent optical depth profiles of the doublet were in agreement

[13] Actually, we searched for doublets at higher redshifts than $z_{\rm em}$ as a secondary check to the adopted values of $z_{\rm em}$. We did not find any C IV doublets with $z_{1548} > z_{\rm em}$.

(2); and other candidate transitions beside Lyα were detected with $W_r \geqslant 3\,\sigma_{W_r}$ (1).

The equivalent width ratio of C IV 1548 to 1550 was measured as follows:

$$R_W = \frac{W_{r,1548}}{W_{r,1550}} \tag{5}$$
$$\sigma^2_{R_W} = R^2_W\left(\left(\frac{\sigma_{W_r,1548}}{W_{r,1548}}\right)^2 + \left(\frac{\sigma_{W_r,1550}}{W_{r,1550}}\right)^2\right),$$

where the variance $\sigma^2_{R_W}$ resulted from the propagation of errors. The actual diagnostic flag = 64 applied to doublets where $1 - \sigma_{R_W} \leqslant R_W \leqslant 2 + \sigma_{R_W}$. The upper limit was set by the characteristic ratio for an unsaturated doublet, and the expected ratio decreases for increasingly saturated doublets until $W_{r,1548} = W_{r,1550}$, hence, the lower limit.

The redshift of the 1548 line z_{1548} must equal the redshift of the 1550 line z_{1550} for an unblended C IV doublet, detected with infinite S/N and infinite resolution. To accommodate blending and the range of S/N ratios and resolutions of the spectra, the binary diagnostic flag = 32 applied to doublets with $|\delta v_{\rm C\,IV}| \leqslant 10\,{\rm km\,s^{-1}}$, where

$$\delta v_{\rm C\,IV} = c\left(\frac{z_{1550} - z_{1548}}{1 + z_{1548}}\right). \tag{6}$$

A candidate system was outside the Lyα forest when $\lambda_{1548}(1+z_{1548}) \geqslant \lambda_\alpha(1+z_{\rm em})$ (flag = 8). Similarly, a candidate was outside the H_2 forest when $\lambda_{1548}(1+z_{1548}) \geqslant \lambda_{H_2}(1+z_{\rm em})$ (flag = 4), where $\lambda_{H_2} = 1138.867$ Å for H_2 B0-0P(7), the last H_2 transition considered (see Prochaska et al. 2004, for atomic and molecular line data).

The profiles of the 1548 and 1550 lines were considered to have matched when they agreed within 1σ for 68.3% of the range λ_l to λ_h (flag = 2). The profiles were defined by the apparent optical depth (AOD) column densities, similar to Equation (3):

$$N_i = \frac{10^{14.5762}}{f_{\rm osc}\lambda_r}\ln\left(\frac{1}{f_{\lambda i}}\right)\delta v_{\lambda,i}\ ({\rm cm^{-2}}) \tag{7}$$
$$\sigma^2_{N_i} = \left(\frac{10^{14.5762}}{f_{\rm osc}\lambda_r}\frac{\sigma_{f_\lambda i}}{f_{\lambda i}}\delta v_{\lambda,i}\ ({\rm cm^{-2}})\right)^2,$$

where i indicates the pixels between λ_l and λ_h. The profiles were smoothed over 3 pixels to minimize the effects of spurious pixels and noisy spectra. C IV doublets with the diagnostic flag = 2 have

$$|N_{i,1548} - N_{i,1550}| \leqslant \sqrt{\sigma^2_{N_{i,1548}} + \sigma^2_{N_{i,1550}}} \tag{8}$$

for more than 68.3% of the range λ_l to λ_h. The AOD profiles were computed only for the candidate C IV doublets.

The flags are binary and sum uniquely. They are ordered so that doublets satisfying more of the diagnostic criteria have higher flag values. For the current study, we focus on the doublets with both lines detected at $\geqslant 3\sigma_{W_r}$, or flag $\geqslant$ 384.

3.3. Final C IV Sample

The 319 candidate C IV systems with $W_{r,1548} \geqslant 3\sigma_{W_r,1548}$, R_W within the expected range, and $|\delta v_{\rm C\,IV}| \leqslant 10\,{\rm km\,s^{-1}}$ were visually evaluated by multiple authors. The remaining systems were reviewed by at least one author. We assessed the likelihood of each candidate, utilizing the diagnostics described in the previous section. Then we agreed upon two groups of intervening C IV systems that had z_{1548} more than $1000\,{\rm km\,s^{-1}}$ redward of the Milky Way Galaxy ($z = 0$) and more than $3000\,{\rm km\,s^{-1}}$ blueward of the background source ($z = z_{\rm em}$): 44 definite systems (G = 1) and 19 likely systems (G = 2). The detailed information about all G = 1+2 systems is listed in Table 4 and the summary of the doublets is listed in Table 5. An example velocity plot of a C IV doublet is given in Figure 3, and the full complement of velocity plots are in Appendix A. The cumulative distribution of column densities and equivalent widths are given in Figure 4.

Table 3
C IV Diagnostic Flags

Flag	Description
256	$W_{r,1548} \geqslant 3\sigma_{W_r,1548}$
128	$W_{r,1550} \geqslant 3\sigma_{W_r,1548}$
64	$1 - \sigma_{R_W} \leqslant R_W \leqslant 2 + \sigma_{R_W}$
32	$\lvert\delta v_{\rm C\,IV}\rvert \leqslant 10\,{\rm km\,s^{-1}}$
16	Candidate Lyα with $W_{r,1215} \geqslant 3\sigma_{W_r,1215}$
8	C IV 1548 outside Lyα forest
4	C IV 1548 outside H_2 forest
2	$\geqslant$68.3% AOD profile per element (pixel) in 1σ agreement
1	Other candidate absorption lines with $W_r \geqslant 3\sigma_{W_r}$

Note. Binary diagnostic flags for C IV doublets. (For more information, see Section 3.2.)

The final, visual evaluation of the candidates was subjective. We required consensus among the authors in defining our final sample. Typically, the definite (G = 1) systems show other transitions, usually Lyα and/or Si IV. When there was no coverage of the other transitions, which had lower rest wavelengths, the G = 1 C IV doublets were multi-component with matching AOD profiles.

Typically, the G = 2 systems include the C IV doublets detected in regions where the S/N was low, so the comparison of the profiles was less conclusive, and there were not enough other positive diagnostics (e.g., detection of Lyα) to boost the confidence of the identification.

For all C IV systems, we confirmed that the C IV doublet was not a higher-redshift O I 1302, Si II 1304 pair, which has rest wavelength separation similar to that of the doublet, by checking whether Si II 1260 existed and was much stronger than the 1304 line. We also confirmed that the doublet and the other transitions were not other, common transitions at different redshifts.

We adjusted the wavelength limits (λ_l, λ_h) as necessary to correct for blending. For example, in Figure 2, the wavelength bounds for the C IV 1548 line was reduced.

For the remaining analyses, we restrict our intergalactic C IV sample to the systems where both lines of the doublet were detected with $W_r \geqslant 3\,\sigma_{W_r}$.[14] This left 38 G = 1 systems and five G = 2 systems.

4. SURVEY SENSITIVITY

4.1. Monte Carlo Completeness Tests

We used Monte Carlo tests to determine the column density and equivalent width limit, as a function of the redshift, where we recovered 95% of the simulated C IV doublets for each

[14] We list all G = 1+2 C IV systems in Table 4 for the community and any future analyses with different criteria.

Table 4
C IV Systems Summary

(1) z_{1548}	(2) $\delta v_{\rm abs}$ (km s^{-1})	(3) λ_r (Å)	(4) λ_l (Å)	(5) λ_h (Å)	(6) W_r (mÅ)	(7) σ_{W_r} (mÅ)	(8) log N	(9) $\sigma_{\log N}$	(10) G	(11) Flag
PG0117+213 ($z_{\rm em} = 1.493$)										
0.51964	...	1548.19	2352.30	2353.07	94	24	13.47	0.11	2	288
	−3.5	1550.77	2356.21	2356.98	<45	...	< 13.39	...		
0.57632	...	1548.19	2439.35	2441.47	728	28	> 14.56	...	1	450
	12.6	1550.77	2443.41	2445.24	442	25	14.52	0.03		
PKS0232–04 ($z_{\rm em} = 1.440$)										
0.73910	...	1548.19	2691.50	2693.40	372	34	14.16	0.08	1	450
	18.7	1550.77	2695.98	2697.88	359	41	> 14.43	...		
0.86818	...	1548.19	2891.94	2892.69	69	22	< 13.13	...	2	358
	−5.6	1550.77	2896.75	2897.50	<37	...	< 13.32	...		
PKS0405–123 ($z_{\rm em} = 0.573$)										
0.36071	...	1548.19	2106.28	2107.05	86	17	13.37	0.09	1	383
	6.4	1550.77	2109.79	2110.55	<35	...	< 13.27	...		
	53.0	1215.67	1653.80	1655.51	769	35	> 14.47	...		
	15.7	1025.72	1395.47	1396.23	270	10	> 14.93	...		
	8.7	977.02	1329.24	1329.69	142	9	> 13.68	...		
	19.9	1206.50	1641.62	1641.94	73	12	12.70	0.09		
PKS0454–22 ($z_{\rm em} = 0.534$)										
0.20645	...	1548.19	1867.44	1868.12	142	24	13.64	0.08	2	366
	0.9	1550.77	1870.54	1871.23	81	26	13.70	0.14		
0.24010	...	1548.19	1919.35	1920.52	644	57	> 14.20[a]	...	1	494
	7.7	1550.77	1922.54	1923.71	495	54	> 14.39[a]	...		
0.27797	...	1548.19	1978.18	1979.04	274	52	> 13.83[a]	...	1	366
	−9.6	1550.77	1981.47	1982.33	<104	...	< 14.20	...		
0.38152	...	1548.19	2138.54	2139.20	96	32	< 13.55	...	1	494
	1.2	1550.77	2142.10	2142.76	110	27	> 13.73[a]	...		
	3.8	1215.67	1679.22	1679.74	<466	...	< 14.23[a]	...		
0.40227	...	1548.19	2170.55	2171.37	177	29	< 13.72	...	1	494
	1.7	1550.77	2174.16	2174.99	140	31	> 13.84[a]	...		
	−5.4	1215.67	1704.35	1704.99	<458	...	< 14.23[a]	...		
0.42955	...	1548.19	2212.93	2213.58	81	25	< 13.20	...	2	366
	9.0	1550.77	2216.61	2217.26	<50	...	< 13.44	...		
	−1.6	1215.67	1737.63	1738.14	<269	...	< 13.97	...		
	2.0	977.02	1396.51	1396.92	<259	...	< 13.90[a]	...		
0.47436	...	1548.19	2281.82	2283.46	645	37	> 14.55	...	1	511
	−6.2	1550.77	2285.62	2287.25	524	33	> 14.75	...		
	105.2	1215.67	1790.54	1795.92	2768	327	> 14.71[a]	...		
	7.3	1206.50	1778.44	1779.41	581	126	> 13.43[a]	...		
	8.1	1260.42	1857.67	1859.04	617	31	> 14.03	...		
	−0.0	1393.76	2054.25	2055.56	635	52	> 13.84[a]	...		
	−1.7	1402.77	2067.54	2068.85	475	56	> 14.02[a]	...		
0.48328	...	1548.19	2295.80	2296.92	246	27	14.04	0.08	1	511
	−3.4	1550.77	2299.61	2300.74	183	29	14.12	0.09		
	28.5	1215.67	1802.80	1803.92	599	105	> 14.04[a]	...		
	−0.2	1206.50	1789.01	1790.12	631	124	> 13.47[a]	...		
	0.4	1260.42	1869.08	1869.97	233	21	> 13.52	...		
HE0515–4414 ($z_{\rm em} = 1.710$)										
0.50601	...	1548.19	2330.91	2332.37	448	28	> 14.36	...	2	482
	−0.8	1550.77	2334.79	2335.94	333	21	14.39	0.04		
0.73082	...	1548.19	2679.29	2679.99	27	9	12.86	0.14	2	354
	−0.1	1550.77	2683.74	2684.44	<17	...	< 12.96	...		
0.94042	...	1548.19	3003.24	3005.31	365	20	> 14.27	...	1	499
	2.1	1550.77	3008.24	3010.31	242	23	14.24	0.05		
	32.9	1215.67	2357.83	2360.83	1052	29	> 14.68	...		
	20.0	1206.50	2340.48	2342.09	190	18	13.08	0.05		
	10.9	1260.42	2445.09	2446.77	122	19	13.00	0.07		
	6.9	1393.76	2703.77	2705.23	233	13	13.58	0.03		
	7.3	1402.77	2721.26	2722.73	56	11	13.15	0.08		
HS0624+6907 ($z_{\rm em} = 0.370$)										
0.06351	...	1548.19	1646.18	1646.78	106	10	13.54	0.04	1	503

Table 4
(Continued)

(1) z_{1548}	(2) $\delta v_{\rm abs}$ (km s^{-1})	(3) λ_r (Å)	(4) λ_l (Å)	(5) λ_h (Å)	(6) W_r (mÅ)	(7) σ_{W_r} (mÅ)	(8) log N	(9) $\sigma_{\log N}$	(10) G	(11) Flag
	−7.7	1550.77	1648.92	1649.52	61	10	13.55	0.07		
	−16.2	1215.67	1292.28	1293.28	594	11	> 14.43	...		
	−20.7	1025.72	1090.36	1091.20	357	23	> 15.09	...		
	−1.6	1206.50	1282.91	1283.30	150	9	13.05	0.04		
0.07574	...	1548.19	1665.24	1665.72	53	6	13.19	0.05	1	503
	5.4	1550.77	1668.01	1668.49	32	8	13.23	0.11		
	0.9	1215.67	1307.45	1308.15	300	10	> 14.09	...		
	1.3	1025.72	1103.16	1103.68	127	28	14.49	0.12		
HS0747+4259 ($z_{\rm em} = 1.897$)										
0.83662	...	1548.19	2842.55	2844.22	303	25	> 14.11	...	2	481
	−0.7	1550.77	2847.27	2848.95	232	30	14.20	0.06		
	−19.8	1215.67	2232.02	2233.33	<86	...	< 13.39	...		
HS0810+2554 ($z_{\rm em} = 1.510$)										
0.83135	...	1548.19	2834.27	2836.40	774	49	> 14.63	...	1	499
	2.8	1550.77	2838.99	2841.12	724	53	> 14.89	...		
	62.4	1215.67	2225.35	2228.26	1242	106	> 14.61	...		
	36.6	1206.50	2209.27	2210.36	380	62	> 13.25[a]	...		
	13.1	1393.76	2551.82	2553.29	262	30	13.67	0.08		
	13.0	1402.77	2568.32	2569.80	271	31	13.91	0.06		
0.87687	...	1548.19	2905.00	2906.32	219	55	> 13.73[a]	...	2	486
	−7.8	1550.77	2909.83	2911.15	162	49	< 13.94	...		
	−24.5	1215.67	2281.20	2282.09	<98	...	< 0.30	...		
PG0953+415 ($z_{\rm em} = 0.234$)										
0.06807	...	1548.19	1653.40	1653.77	136	26	> 13.53[a]	...	1	383
	−2.7	1550.77	1656.15	1656.52	<50	...	< 13.63	...		
	3.7	1215.67	1298.15	1298.74	281	8	> 14.08	...		
	−12.3	1025.72	1095.32	1095.81	129	8	14.44	0.03		
	−0.2	977.02	1043.41	1043.65	74	7	13.21	0.05		
	−3.1	1031.93	1102.00	1102.31	108	7	14.13	0.03		
	−5.1	1037.62	1108.08	1108.39	74	7	14.27	0.04		
	−3.4	1238.82	1322.98	1323.29	48	7	13.49	0.06		
	3.0	1242.80	1327.24	1327.55	29	7	13.49	0.10		
MARK132 ($z_{\rm em} = 1.757$)										
0.70776	...	1548.19	2643.55	2644.28	29	9	12.88	0.13	2	354
	0.4	1550.77	2647.95	2648.68	<17	...	< 12.93	...		
0.74843	...	1548.19	2706.10	2707.69	318	13	14.13	0.03	1	482
	−0.4	1550.77	2710.60	2712.20	165	12	14.08	0.03		
0.76352	...	1548.19	2729.63	2730.92	110	11	13.53	0.05	1	482
	−1.4	1550.77	2734.17	2735.46	75	16	13.64	0.09		
3C249.1 ($z_{\rm em} = 0.312$)										
0.02616	...	1548.19	1588.55	1588.81	24	7	12.81	0.14	2	375
	−7.6	1550.77	1591.19	1591.45	<13	...	< 12.81	...		
	−33.4	1215.67	1246.76	1247.75	317	15	13.95	0.03		
	−31.2	977.02	1002.15	1002.74	524	78	> 13.91[a]	...		
PG1206+459 ($z_{\rm em} = 1.155$)										
0.60072	...	1548.19	2477.60	2478.89	185	25	13.74	0.07	2	358
	−5.4	1550.77	2481.72	2483.01	<45	...	< 13.38	...		
0.73377	...	1548.19	2683.80	2684.56	176	7	13.80	0.02	2	494
	−2.1	1550.77	2688.26	2689.02	83	9	13.68	0.05		
0.92677	...	1548.19	2979.54	2985.83	2363	59	> 15.15	...	1	477
	−75.8	1550.77	2984.50	2990.79	2156	54	> 15.39	...		
	−15.0	1215.67	2339.49	2345.04	2384	30	> 15.07	...		
	66.8	1206.50	2321.60	2326.84	983	40	> 13.97	...		
	−94.8	1238.82	2384.15	2388.91	876	39	> 14.85	...		
	−98.9	1242.80	2391.82	2396.59	496	34	14.82	0.03		
	100.2	1260.42	2427.17	2430.55	431	25	> 13.73	...		
	21.7	1393.76	2682.52	2687.93	778	18	14.08	0.01		
	58.3	1402.77	2699.87	2705.31	402	28	14.06	0.03		
0.93425	...	1548.19	2993.93	2995.25	259	22	> 14.18	...	1	511
	0.5	1550.77	2998.91	3000.23	200	20	> 14.34	...		

Table 4
(Continued)

(1) z_{1548}	(2) $\delta v_{\rm abs}$ (km s^{-1})	(3) λ_r (Å)	(4) λ_l (Å)	(5) λ_h (Å)	(6) W_r (mÅ)	(7) σ_{W_r} (mÅ)	(8) log N	(9) $\sigma_{\log N}$	(10) G	(11) Flag
	−14.4	1215.67	2350.48	2352.09	552	21	> 14.42	...		
	2.6	1206.50	2333.27	2334.11	133	15	> 13.13	...		
	5.9	1393.76	2695.43	2696.40	143	11	> 13.51	...		
	3.6	1402.77	2712.87	2713.84	98	11	13.60	0.06		
PG1211+143 ($z_{\rm em} = 0.081$)										
0.05114	...	1548.19	1626.83	1627.67	264	10	> 14.07	...	1	509
	3.8	1550.77	1629.54	1630.38	147	10	14.01	0.03		
	36.0	1215.67	1276.98	1279.19	1214	7	> 14.74	...		
	20.8	1025.72	1077.59	1078.89	823	103	> 15.33	...		
	−50.1	977.02	1026.58	1027.04	304	85	> 13.67[a]	...		
	13.5	1206.50	1268.07	1268.37	123	3	12.94	0.01		
	21.6	1260.42	1324.88	1325.05	24	2	12.29	0.04		
	12.0	1393.76	1464.88	1465.29	66	4	12.96	0.03		
	12.3	1402.77	1474.35	1474.76	44	5	13.04	0.05		
0.06439	...	1548.19	1647.56	1648.21	71	9	13.29	0.05	1	511
	−6.9	1550.77	1650.30	1650.95	31	9	13.24	0.12		
	36.4	1215.67	1293.48	1295.26	861	5	> 14.55	...		
	30.6	1025.72	1091.36	1092.50	448	12	> 15.14	...		
	−6.4	977.02	1039.69	1040.14	144	9	13.52	0.03		
	58.3	1031.93	1098.13	1099.07	183	11	14.26	0.03		
	60.6	1037.62	1104.19	1105.13	67	11	14.09	0.07		
	−4.4	1206.50	1283.96	1284.43	29	4	12.17	0.06		
	38.5	1260.42	1341.58	1341.96	10	3	11.85	0.12		
MRK205 ($z_{\rm em} = 0.071$)										
0.00427	...	1548.19	1554.46	1555.20	292	23	> 14.14	...	1	511
	8.6	1550.77	1557.05	1557.78	196	23	> 14.17	...		
	11.3	1215.67	1220.38	1221.47	807	32	> 14.53	...		
	13.3	1025.72	1029.68	1030.64	486	29	> 15.23	...		
	−6.7	977.02	980.81	981.56	382	46	> 14.13	...		
	4.6	989.80	993.68	994.38	301	41	> 14.51[a]	...		
	8.4	1206.50	1211.42	1211.97	263	32	> 13.09[a]	...		
	8.3	1260.42	1265.57	1266.25	240	11	> 13.54	...		
	3.7	1393.76	1399.43	1400.00	122	11	13.25	0.04		
	1.3	1402.77	1408.48	1409.05	75	13	13.33	0.07		
QSO–123050+011522 ($z_{\rm em} = 0.117$)										
0.00574	...	1548.19	1556.92	1557.24	65	11	13.34	0.07	1	511
	−0.2	1550.77	1559.51	1559.75	36	9	13.33	0.11		
	−9.0	1215.67	1222.14	1223.32	684	21	> 14.48	...		
	−9.9	1206.50	1213.19	1213.59	175	34	> 12.91[a]	...		
	−12.6	1260.42	1267.41	1267.77	74	11	12.83	0.07		
	−4.9	1393.76	1401.47	1401.92	66	8	12.96	0.05		
	−7.9	1402.77	1410.54	1410.99	63	9	13.21	0.06		
PG1241+176 ($z_{\rm em} = 1.283$)										
0.48472	...	1548.19	2298.17	2299.23	305	46	> 13.88[a]	...	2	352
	−8.9	1550.77	2302.00	2303.05	<93	...	< 14.15	...		
0.55070	...	1548.19	2399.44	2402.21	852	44	> 14.60	...	1	450
	12.8	1550.77	2403.43	2406.21	580	50	14.60	0.05		
0.55842	...	1548.19	2412.41	2413.21	230	33	> 13.75[a]	...	1	482
	−4.9	1550.77	2416.42	2417.23	204	29	14.26	0.10		
0.75776	...	1548.19	2721.08	2721.63	100	13	13.58	0.07	1	486
	−0.1	1550.77	2725.61	2726.06	50	12	13.47	0.11		
0.78567	...	1548.19	2763.64	2765.44	134	14	13.58	0.05	1	486
	1.4	1550.77	2768.23	2770.04	71	13	13.59	0.08		
0.89546	...	1548.19	2934.10	2934.86	106	25	> 13.42[a]	...	1	509
	−1.5	1550.77	2938.98	2939.74	126	27	> 13.79[a]	...		
	−5.6	1215.67	2303.47	2304.94	510	42	> 13.97[a]	...		
	−3.4	1206.50	2286.53	2287.17	79	23	< 12.76	...		
PG1248+401 ($z_{\rm em} = 1.032$)										
0.55277	...	1548.19	2403.65	2404.35	52	15	13.16	0.13	2	486
	8.5	1550.77	2407.64	2408.35	64	17	13.56	0.12		
0.56484	...	1548.19	2422.25	2423.16	97	14	13.51	0.06	1	484

Table 4
(Continued)

(1) z_{1548}	(2) $\delta v_{\rm abs}$ (km s^{-1})	(3) λ_r (Å)	(4) λ_l (Å)	(5) λ_h (Å)	(6) W_r (mÅ)	(7) σ_{W_r} (mÅ)	(8) log N	(9) $\sigma_{\log N}$	(10) G	(11) Flag
	4.9	1550.77	2426.27	2427.19	80	13	13.71	0.07		
0.70104	...	1548.19	2633.11	2633.97	108	24	13.64	0.13	1	492
	−0.3	1550.77	2637.49	2638.35	76	22	13.72	0.13		
0.77291	...	1548.19	2743.91	2745.76	619	33	> 14.56	...	1	495
	3.7	1550.77	2748.48	2750.33	564	29	> 14.77	...		
	6.2	1393.76	2470.19	2471.84	426	14	> 13.98	...		
	4.7	1402.77	2486.17	2487.83	315	12	14.02	0.02		
0.85508	...	1548.19	2870.57	2873.99	826	39	> 14.59	...	1	463
	−11.5	1550.77	2875.34	2878.77	567	41	> 14.65	...		
	−79.1	1260.42	2336.91	2338.58	196	29	13.34	0.11		
	−33.2	1393.76	2584.38	2585.96	226	22	13.52	0.05		
	−45.9	1402.77	2601.10	2602.69	137	32	13.59	0.10		
PG1259+593 ($z_{\rm em} = 0.478$)										
0.04615	...	1548.19	1619.46	1619.85	103	21	> 13.41[a]	...	1	499
	0.9	1550.77	1622.16	1622.54	74	19	13.71	0.11		
	34.8	1215.67	1271.17	1272.78	1043	18	> 14.65	...		
	−11.3	1025.72	1072.39	1073.64	748	35	> 15.40	...		
	−7.2	977.02	1021.61	1022.67	411	22	> 14.14	...		
	35.0	1206.50	1261.91	1262.83	220	13	13.14	0.03		
PKS1302–102 ($z_{\rm em} = 0.278$)										
0.00438	...	1548.19	1554.81	1555.14	32	8	12.94	0.11	1	383
	−6.5	1550.77	1557.40	1557.73	<18	...	< 12.98	...		
	−1.3	1215.67	1220.75	1221.23	300	18	> 14.15	...		
	−0.1	1025.72	1029.83	1030.58	240	14	> 14.88	...		
	−17.3	977.02	980.89	981.60	234	34	> 13.91	...		
CSO873 ($z_{\rm em} = 1.014$)										
0.66089	...	1548.19	2569.87	2572.23	424	37	> 14.24	...	1	494
	3.7	1550.77	2574.14	2576.51	272	34	> 14.31	...		
0.73385	...	1548.19	2683.86	2684.74	77	19	13.38	0.10	1	366
	−2.2	1550.77	2688.33	2689.21	<39	...	< 13.33	...		
PG1630+377 ($z_{\rm em} = 1.476$)										
0.75420	...	1548.19	2715.42	2716.22	49	14	13.17	0.11	2	354
	−1.2	1550.77	2719.94	2720.74	<27	...	< 13.15	...		
0.91440	...	1548.19	2963.34	2965.06	384	16	> 14.28	...	1	469
	10.3	1550.77	2968.17	2969.99	317	18	> 14.43	...		
	−2.0	1215.67	2325.82	2328.60	1076	33	> 14.69	...		
	8.9	1206.50	2309.25	2310.59	142	19	12.99	0.07		
	−12.6	1393.76	2667.64	2668.60	123	15	13.26	0.06		
	−12.5	1402.77	2684.89	2685.86	98	12	13.47	0.06		
0.95269	...	1548.19	3022.00	3023.84	560	21	> 14.43	...	1	477
	−24.3	1550.77	3027.02	3028.87	276	22	14.27	0.04		
	70.6	1215.67	2372.75	2376.16	1434	25	> 14.83	...		
	8.9	1206.50	2355.41	2356.56	157	19	13.00	0.06		
	3.9	1260.42	2460.75	2461.78	43	13	12.54	0.13		
	14.7	1393.76	2720.92	2722.40	202	15	13.49	0.04		
	23.1	1402.77	2738.52	2740.01	136	21	13.59	0.07		
PG1634+706 ($z_{\rm em} = 1.334$)										
0.41935	...	1548.19	2197.10	2197.71	44	11	13.07	0.11	2	354
	0.4	1550.77	2200.76	2201.37	<22	...	< 13.06	...		
0.65126	...	1548.19	2556.26	2556.77	67	6	13.33	0.04	1	496
	−3.0	1550.77	2560.51	2560.94	67	6	13.61	0.04		
	0.3	1215.67	2007.05	2007.67	78	21	13.25	0.12		
0.65355	...	1548.19	2559.31	2560.62	393	9	> 14.29	...	1	499
	2.0	1550.77	2563.57	2564.88	284	10	14.34	0.02		
	0.9	1215.67	2009.41	2010.92	630	30	> 14.45	...		
	−63.3	1206.50	1993.91	1995.48	502	28	> 13.71	...		
	−7.2	1393.76	2303.95	2305.30	145	11	13.30	0.04		
	0.1	1402.77	2318.85	2320.21	73	10	13.26	0.06		
0.81814	...	1548.19	2814.55	2815.30	90	4	13.51	0.02	1	501

Table 4
(Continued)

(1) z_{1548}	(2) $\delta v_{\rm abs}$ (km s^{-1})	(3) λ_r (Å)	(4) λ_l (Å)	(5) λ_h (Å)	(6) W_r (mÅ)	(7) σ_{W_r} (mÅ)	(8) log N	(9) $\sigma_{\log N}$	(10) G	(11) Flag
	−0.1	1550.77	2819.23	2819.98	67	4	13.61	0.03		
	−0.2	1215.67	2209.74	2210.75	201	10	> 13.92	...		
	−23.7	1206.50	2193.22	2193.83	115	7	12.88	0.03		
	−2.4	1260.42	2291.25	2291.88	21	6	12.21	0.13		
	−1.0	1393.76	2533.54	2534.40	<15	...	< 12.25	...		
	−3.4	1402.77	2549.93	2550.79	21	7	12.71	0.13		
0.90560	...	1548.19	2949.76	2950.74	198	7	14.04	0.04	1	509
	−0.5	1550.77	2954.66	2955.65	165	7	14.20	0.03		
	−1.6	1215.67	2316.12	2317.05	315	6	> 14.16	...		
	−5.3	1025.72	1954.23	1955.01	180	20	> 14.39[a]	...		
	−4.3	1031.93	1966.01	1966.81	104	22	14.08	0.10		
	−7.1	1037.62	1976.85	1977.66	67	18	14.11	0.12		
	−2.7	1206.50	2298.85	2299.38	61	6	12.58	0.05		
	1.3	1238.82	2360.43	2360.98	67	6	13.57	0.04		
	−8.8	1242.80	2368.02	2368.57	52	5	13.74	0.05		
	−21.3	1260.42	2401.59	2402.15	107	4	13.09	0.03		
	7.0	1393.76	2655.64	2656.26	259	5	13.82	0.03		
	−3.1	1402.77	2672.82	2673.44	40	6	13.01	0.06		
0.91144	...	1548.19	2958.77	2959.74	34	7	12.96	0.09	2	383
	−2.8	1550.77	2963.69	2964.66	<17	...	< 12.92	...		
	18.3	1215.67	2322.48	2324.84	660	11	> 14.48	...		
	1.6	1025.72	1959.76	1961.33	311	25	> 14.91	...		
HS1700+6416 ($z_{\rm em} = 2.736$)										
0.08077	...	1548.19	1673.11	1673.40	289	90	> 13.80	...	2	371
	−1.5	1550.77	1675.90	1676.18	<154	...	< 14.40	...		
	4.7	1215.67	1313.28	1314.36	661	28	> 14.43	...		
PG1718+481 ($z_{\rm em} = 1.084$)										
0.45953	...	1548.19	2259.21	2259.97	147	13	13.68	0.04	1	480
	−8.6	1550.77	2262.97	2263.72	120	13	13.83	0.05		
H1821+643 ($z_{\rm em} = 0.297$)										
0.22503	...	1548.19	1895.74	1897.42	137	23	13.61	0.07	1	381
	3.0	1550.77	1898.90	1900.57	<47	...	< 13.38	...		
	−51.7	1215.67	1488.23	1489.74	834	13	> 14.60	...		
	−33.7	1025.72	1255.90	1256.80	496	9	> 15.24	...		
	−17.9	977.02	1196.50	1197.22	306	13	> 13.99	...		
	−11.5	1031.93	1263.72	1264.45	172	9	14.26	0.02		
	−12.0	1037.62	1270.68	1271.42	106	9	14.30	0.04		
	−4.0	1206.50	1477.75	1478.19	88	7	12.79	0.04		
0.24531	...	1548.19	1927.27	1928.76	75	22	13.32	0.12	2	383
	−1.2	1550.77	1930.47	1931.97	<44	...	< 13.35	...		
	3.2	1215.67	1513.68	1514.08	47	8	13.01	0.07		
	−25.3	1025.72	1277.01	1277.51	55	8	13.95	0.06		
	1.1	1031.93	1284.86	1285.28	50	7	13.67	0.06		
	3.8	1037.62	1291.94	1292.37	29	5	13.70	0.07		
PHL1811 ($z_{\rm em} = 0.190$)										
0.08091	...	1548.19	1673.01	1673.74	189	25	> 13.93	...	1	511
	−0.6	1550.77	1675.79	1676.53	129	22	14.03	0.10		
	−27.8	1215.67	1313.15	1314.77	904	9	> 14.64	...		
	−36.0	1025.72	1108.19	1109.04	622	8	> 15.36	...		
	−19.7	977.02	1055.61	1056.31	338	9	> 14.07	...		
	11.7	989.80	1069.72	1070.02	137	7	> 14.47	...		
	10.9	1206.50	1303.98	1304.27	179	4	> 13.31	...		
	2.2	1260.42	1362.31	1362.60	172	4	> 13.44	...		

Notes. C IV systems by target and redshift of C IV 1548. Upper limits are 2σ limits for both W_r and log N. The column densities were measured by the AODM, unless "COG" indicated, in which case, the limit is from assuming W_r results from the linear portion of the COG. The definite C IV doublets are labeled group G = 1, while the likely doublets are G = 2. The binary flag is described in Table 3 and Section 3.2.
[a] COG.

Table 5
C IV Doublet Summary

(1) Target	(2) G	(3) z_{1548}	(4) $W_{r,1548}$ (mÅ)	(5) $W_{r,1550}$ (mÅ)	(6) $\log N_{1548}$	(7) $\log N_{1550}$	(8) $\log N(C^{+3})$
PG0117+213	2	0.51964	94 ± 24	<45	13.47 ± 0.11	<13.39	13.47 ± 0.11
	1	0.57632	728 ± 28	442 ± 25	>14.56	14.52 ± 0.03	14.52 ± 0.03
PKS0232–04	1	0.73910	372 ± 34	359 ± 41	14.16 ± 0.08	>14.43	14.16 ± 0.08
	2	0.86818	69 ± 22	<37	<13.13	<13.32	<13.13
PKS0405–123	1	0.36071	86 ± 17	<35	13.37 ± 0.09	<13.27	13.37 ± 0.09
PKS0454–22	2	0.20645	142 ± 24	81 ± 26	13.64 ± 0.08	13.70 ± 0.14	13.65 ± 0.07
	1	0.24010	644 ± 57	495 ± 54	>14.20[a]	>14.39[a]	>14.39
	1	0.27797	274 ± 52	<104	>13.83[a]	<14.20	[13.83, 14.14]
	1	0.38152	96 ± 32	110 ± 27	<13.55	>13.73[a]	[13.43, 13.77][b]
	1	0.40227	177 ± 29	140 ± 31	<13.72	>13.84[a]	[13.84, 13.88]
	2	0.42955	81 ± 25	<50	<13.20	<13.44	<13.44
	1	0.47436	645 ± 37	524 ± 33	>14.55	>14.75	>14.75
	1	0.48328	246 ± 27	183 ± 29	14.04 ± 0.08	14.12 ± 0.09	14.07 ± 0.06
HE0515–4414	2	0.50601	448 ± 28	333 ± 21	>14.36	14.39 ± 0.04	14.39 ± 0.04
	2	0.73082	27 ± 9	<17	12.86 ± 0.14	<12.96	12.86 ± 0.14
	1	0.94042	365 ± 20	242 ± 23	>14.27	14.24 ± 0.05	14.24 ± 0.05
HS0624+6907	1	0.06351	106 ± 10	61 ± 10	13.54 ± 0.04	13.55 ± 0.07	13.54 ± 0.03
	1	0.07574	53 ± 6	32 ± 8	13.19 ± 0.05	13.23 ± 0.11	13.20 ± 0.04
HS0747+4259	2	0.83662	303 ± 25	232 ± 30	>14.11	14.20 ± 0.06	14.20 ± 0.06
HS0810+2554	1	0.83135	774 ± 49	724 ± 53	>14.63	>14.89	>14.89
	2	0.87687	219 ± 55	162 ± 49	>13.73[a]	<13.94	[13.73, 14.11]
PG0953+415	1	0.06807	136 ± 26	<50	>13.53[a]	<13.63	[13.53, 13.77]
MARK132	2	0.70776	29 ± 9	<17	12.88 ± 0.13	<12.93	12.88 ± 0.13
	1	0.74843	318 ± 13	165 ± 12	14.13 ± 0.03	14.08 ± 0.03	14.10 ± 0.02
	1	0.76352	110 ± 11	75 ± 16	13.53 ± 0.05	13.64 ± 0.09	13.55 ± 0.04
3C249.1	2	0.02616	24 ± 7	<13	12.81 ± 0.14	<12.81	12.81 ± 0.14
PG1206+459	2	0.60072	185 ± 25	<45	13.74 ± 0.07	<13.38	13.74 ± 0.07
	2	0.73377	176 ± 7	83 ± 9	13.80 ± 0.02	13.68 ± 0.05	13.77 ± 0.02
	1	0.92677	2363 ± 59	2156 ± 54	>15.15	>15.39	>15.39
	1	0.93425	259 ± 22	200 ± 20	>14.18	>14.34	>14.34
PG1211+143	1	0.05114	264 ± 10	147 ± 10	>14.07	14.01 ± 0.03	14.01 ± 0.03
	1	0.06439	71 ± 9	31 ± 9	13.29 ± 0.05	13.24 ± 0.12	13.28 ± 0.05
MRK205	1	0.00427	292 ± 23	196 ± 23	>14.14	>14.17	>14.17
QSO–123050+011522	1	0.00574	65 ± 11	36 ± 9	13.34 ± 0.07	13.33 ± 0.11	13.34 ± 0.06
PG1241+176	2	0.48472	305 ± 46	<93	>13.88[a]	<14.15	[13.88, 14.01]
	1	0.55070	852 ± 44	580 ± 50	>14.60	14.60 ± 0.05	14.60 ± 0.05
	1	0.55842	230 ± 33	204 ± 29	>13.75[a]	14.26 ± 0.10	14.26 ± 0.10
	1	0.75776	100 ± 13	50 ± 12	13.58 ± 0.07	13.47 ± 0.11	13.54 ± 0.06
	1	0.78567	134 ± 14	71 ± 13	13.58 ± 0.05	13.59 ± 0.08	13.58 ± 0.04
	1	0.89546	106 ± 25	126 ± 27	>13.42[a]	>13.79[a]	>13.79
PG1248+401	2	0.55277	52 ± 15	64 ± 17	13.16 ± 0.13	13.56 ± 0.12	13.25 ± 0.09
	1	0.56484	97 ± 14	80 ± 13	13.51 ± 0.06	13.71 ± 0.07	13.57 ± 0.05
	1	0.70104	108 ± 24	76 ± 22	13.64 ± 0.13	13.72 ± 0.13	13.68 ± 0.09
	1	0.77291	619 ± 33	564 ± 29	>14.56	>14.77	>14.77
	1	0.85508	826 ± 39	567 ± 41	>14.59	>14.65	>14.65
PG1259+593	1	0.04615	103 ± 21	74 ± 19	>13.41[a]	13.71 ± 0.11	13.71 ± 0.11
PKS1302–102	1	0.00438	32 ± 8	<18	12.94 ± 0.11	<12.98	12.94 ± 0.11
CSO873	1	0.66089	424 ± 37	272 ± 34	>14.24	>14.31	>14.31
	1	0.73385	77 ± 19	<39	13.38 ± 0.10	<13.33	13.38 ± 0.10
PG1630+377	2	0.75420	49 ± 14	<27	13.17 ± 0.11	<13.15	13.17 ± 0.11
	1	0.91440	384 ± 16	317 ± 18	>14.28	>14.43	>14.43
	1	0.95269	560 ± 21	276 ± 22	>14.43	14.27 ± 0.04	14.27 ± 0.04
PG1634+706	2	0.41935	44 ± 11	<22	13.07 ± 0.11	<13.06	13.07 ± 0.11
	1	0.65126	67 ± 6	67 ± 6	13.33 ± 0.04	13.61 ± 0.04	13.40 ± 0.03
	1	0.65355	393 ± 9	284 ± 10	>14.29	14.34 ± 0.02	14.34 ± 0.02
	1	0.81814	90 ± 4	67 ± 4	13.51 ± 0.02	13.61 ± 0.03	13.54 ± 0.02
	1	0.90560	198 ± 7	165 ± 7	14.04 ± 0.04	14.20 ± 0.03	14.12 ± 0.03
	2	0.91144	34 ± 7	<17	12.96 ± 0.09	<12.92	12.96 ± 0.09
HS1700+6416	2	0.08077	289 ± 90	<154	>13.80	<14.40	[13.80, 14.06]
PG1718+481	1	0.45953	147 ± 13	120 ± 13	13.68 ± 0.04	13.83 ± 0.05	13.73 ± 0.03
H1821+643	1	0.22503	137 ± 23	<47	13.61 ± 0.07	<13.38	13.61 ± 0.07
	2	0.24531	75 ± 22	<44	13.32 ± 0.12	<13.35	13.32 ± 0.12
PHL1811	1	0.08091	189 ± 25	129 ± 22	>13.93	14.03 ± 0.10	14.03 ± 0.10

Notes. Summary of C IV doublets by target and redshift of C IV 1548. The definite C IV doublets are labeled group G = 1, while the likely doublets are G = 2. Upper limits are 2σ limits for both W_r and $\log N$. The adopted column density for the C IV doublets are listed in the last column (see Section 2.4).

[a] $\log N$ measured by assuming W_r results from the linear portion of the COG.

[b] Limits set by doublet lines increased/decreased by 1σ to set $\log N(C^{+3})$ range.

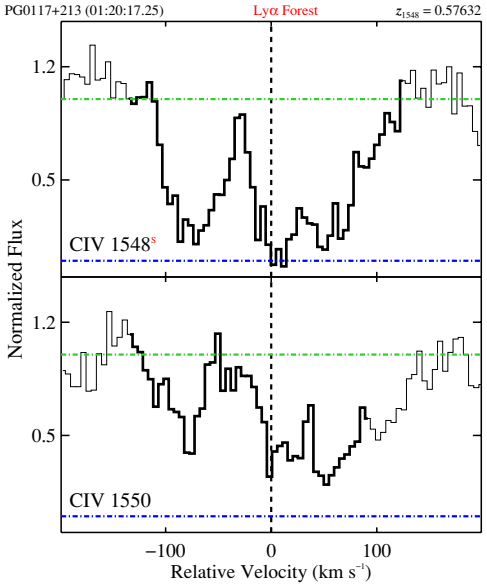

Figure 3. Velocity plot of G = 1 C IV system in the PG0117+213 sightline. The regions of spectra around each absorption line are aligned in velocity space with respect to the rest wavelength of the transition and $z_{1548} = 0.49907$. Saturated transitions are indicated with the (red) "S." The regions used to measure W_r and $\log N(C^{+3})$ are shown by the dark outline. The flux at zero and unity are shown with the dash–dot lines (blue and green, respectively); the vertical dashed line indicates $v = 0$ km s^{-1} corresponding to the optical depth-weighted velocity centroid of the C IV 1548 transition. (The velocity plots for all G = 1 and G = 2 absorbers are in Appendix A.)

(A color version of this figure is available in the online journal.)

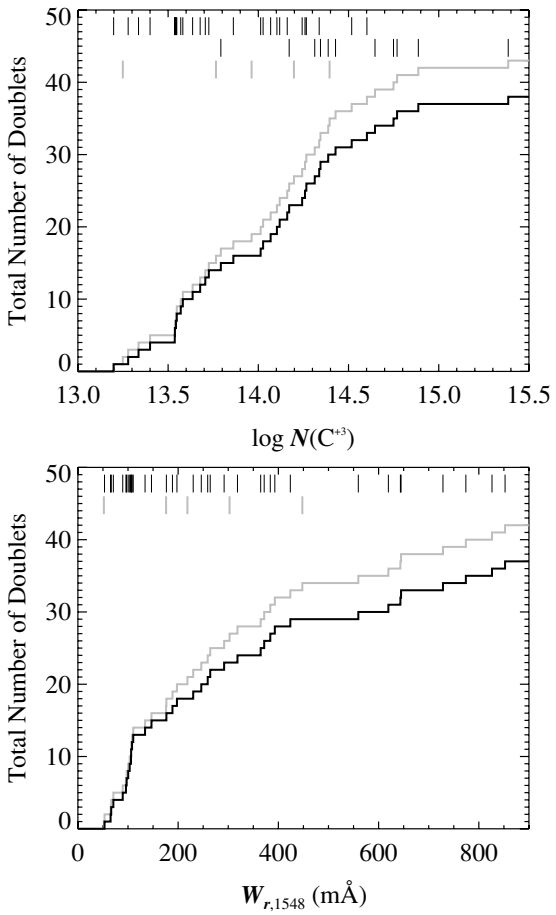

Figure 4. Cumulative column density and equivalent width distributions for the $W_r \geqslant 3\sigma_{W_r}$ G = 1 and G = 2 samples. The black and gray curves are the G = 1 and G = 1+2 groups, respectively. For each absorber, $\log N(C^{+3})$ and $W_{r,1548}$ are indicated with the hashes across the top, with the color indicating the sample. As in Figure 1, the saturated doublets are shown in the middle row of hashes in the top panel. The $z_{1548} = 0.92677$ C IV doublet associated with the DLA in the PG1206+459 sightline, with $W_{r,1548} = 2364$ mÅ, is not shown in the $W_{r,1548}$ plot (bottom panel).

spectrum. From these sensitivity functions, we estimated the unblocked co-moving absorption path lengths $\Delta X(N(C^{+3}))$ and $\Delta X(W_{r,1548})$ for our survey, as defined below.

The simulated C IV doublets were single- or multi-component Voigt profiles. Each Voigt profile was defined by a randomly selected redshift, column density, and Doppler parameter. For the multi-component simulated doublets, each component was assigned a decreasing fraction of the total column density and a velocity offset from the assigned redshift. For each column density bin, $\Delta \log N(C^{+3}) = 0.1$, in the range $12.7 \leqslant \log N(C^{+3}) \leqslant 14.3$, one-hundred randomly generated Voigt profiles were added to the spectrum for each redshift bin, $\delta z = 0.005$, in the range covered by the spectrum. The one-hundred simulated doublets were distributed in a manner that avoided blending. The simulated doublets had Doppler parameters $5\,\mathrm{km\,s^{-1}} \leqslant b \leqslant 25\,\mathrm{km\,s^{-1}}$ and from one to five components in the range $-100\,\mathrm{km\,s^{-1}} \leqslant \delta v_{\mathrm{abs}} \leqslant 100\,\mathrm{km\,s^{-1}}$. We visually inspected the synthetic doublets to verify our model profiles resembled observations of $z > 2$ C IV doublets.

The profiles were added to the "cleaned" spectrum with the appropriate noise. The cleaned spectrum was the original spectrum with all automatically detected absorption features replaced with continuum and noise. The noise was randomly sampled from the neighboring pixels, not in the absorption features. We elected to modify the original spectra (as opposed to generating completely synthetic spectra) to keep the pixel-by-pixel S/N properties of the spectra realistic. The minimum flux level (i.e., the flux at line black) for the optically thick Voigt profiles was measured empirically from the troughs of the strongest absorption lines, typically Galactic, in the original spectrum.

The blind doublet search described in Section 3.1 was conducted on the synthetic spectra. The recovered doublets were matched to the input simulated doublets. The 95% completeness limits $\log N_{\mathrm{lim}}(C^{+3})$ and $W_{r,\mathrm{lim}}$ (for the 1548 line) were measured for each redshift bin. For each redshift bin, we fit a fourth-order polynomial to the percentage of simulated C IV doublets recovered and solved for $\log N_{\mathrm{lim}}(C^{+3})$ and $W_{r,\mathrm{lim}}$ (see Figures 5 and 6, respectively).

4.2. Search Path Length

The sensitivity functions were constructed for every sightline by the previously described Monte Carlo method. From these, we measured the co-moving absorption path lengths $\Delta X(N(C^{+3}))$ and $\Delta X(W_{r,1548})$ (see Figure 7). We converted the sensitivity functions from redshift space ($\delta z = 0.005$ from the Monte Carlo tests) to path length space as follows:

$$X(z) = \frac{2}{3\Omega_{\mathrm{M}}}\sqrt{\Omega_{\mathrm{M}}(1+z)^3 + \Omega_{\Lambda}} \qquad (9)$$
$$\delta X(z) = X(z + 0.5\delta z) - X(z - 0.5\delta z),$$

where $\Omega_{\mathrm{M}} = 0.3$ and $\Omega_{\Lambda} = 0.7$ for our adopted cosmology. The total path length as a function of column density $\Delta X(N(C^{+3}))$

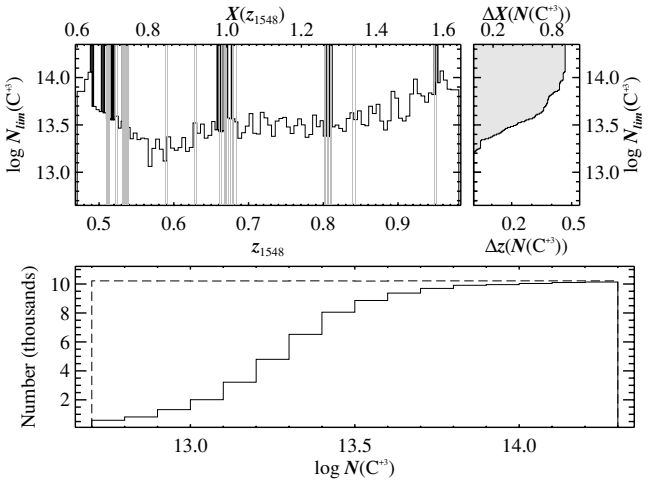

Figure 5. Example Monte Carlo completeness test for $\log N_{\rm lim}(C^{+3})$. The column density limit where our survey was 95% complete is shown for the E230M spectrum of CSO873 (top, left panel). The bottom axis is the redshift of the 1548 line, and the top axis is the corresponding co-moving absorption path length from Equation (9). The general trend follows the S/N profile of the spectrum whose peak sensitivity lies at $\lambda \approx 2600$ Å, corresponding to $z_{1548} \approx 0.68$. The redshift ranges excluded due to Galactic lines are shaded (gray); each Galactic line is counted twice, as a contaminant to both C IV lines. The abrupt, narrow spikes to infinity are the excluded saturated pixels in the Lyα forest. The total path length as a function of $N(C^{+3})$ to which the survey is 95% complete, $\Delta X(N(C^{+3}))$, is shown for this single sightline (top, right panel). For clarity, the gray shaded region lays *under* the $\Delta X(N(C^{+3}))$ curve (also see the total distribution shown in Figure 7). Also shown is the total number of simulated doublets tested (dashed line) compared to the number of recovered doublets (solid line) as a function of $\log N(C^{+3})$ (bottom panel).

is the sum of the bins δX where the 95% completeness limit is $\leqslant N(C^{+3})$:

$$\Delta X(N(C^{+3})) = \sum_{N_{\rm lim} \leqslant N_i} \delta X(N_i) \qquad (10)$$

$$\sigma^2_{\Delta X} = \sigma^2_{\sigma_{N(C^{+3})}} + \sigma^2_{\delta N}.$$

The error $\sigma_{\Delta X}$ reflects the uncertainty induced by the uncertainty in $N(C^{+3})$ and the interpolation of ΔX due to the column density bins δN. The aforementioned also applies to the path length as a function of equivalent width $\Delta X(W_{r,1548})$. For example, in Figure 5, the bins where $\log N_{\rm lim}(C^{+3}) \leqslant 13.5$ totaled $\Delta X(N(C^{+3})) = 0.44$ for CSO873 ($z_{\rm em} = 1.014$). Similarly, we found $\Delta X(W_{r,1548}) = 0.44$ for $W_{r,\rm lim} \leqslant 83$ mÅ. The total absorption path length, $\Delta X(N(C^{+3}))$ (or $\Delta X(W_{r,1548})$) is the sum (Equation (10)) over all sightlines.

We masked out common Galactic lines, which we determined from stacked STIS E140M, E230M, and G230M spectra. We measured the wavelength bounds (λ_l, λ_h) of the common Galactic lines in the stacked spectra. We buffered the redshift range excluded due to Galactic lines by ±20% of the width of the lines (see Figures 5 and 6). Each Galactic line affected the search path twice, as a contaminant to both C IV lines. We excluded the regions 1000 km s^{-1} redward of the Galaxy and 3000 km s^{-1} blueward of the background source.

We also masked out the saturated regions in the Lyα forest for each spectrum. We excluded pixels with $f_{\lambda i} < \sigma_{f_\lambda i}$, and ±3 neighboring pixels, in all features detected by the automatic feature-finding algorithm (see Section 3.1). The excluded pixels included ones from the strongest C IV doublets, but this amounted to a small fraction (<1%) of the total ΔX.

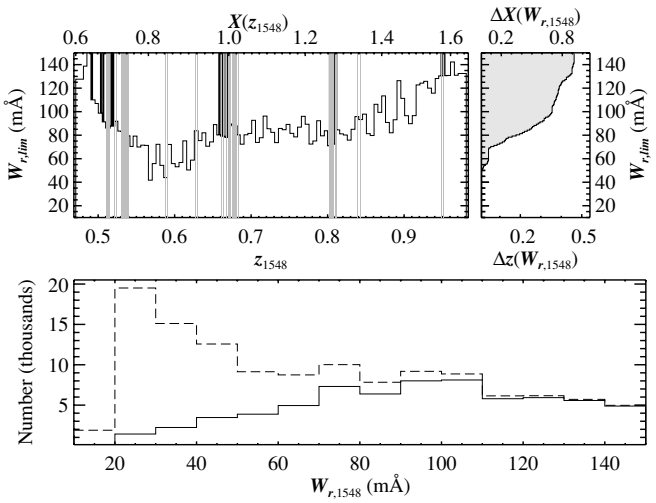

Figure 6. Example Monte Carlo completeness test for $W_{r,\rm lim}$, similar to Figure 5. The rest equivalent width limit for the C IV 1548 line where our survey was 95% complete is shown for the E230M spectrum of CSO873 (top, left panel). The total number of simulated C IV doublets per $W_{r,1548}$ bin was not constant because the simulated doublets were assigned randomly drawn $N(C^{+3})$ and b (bottom panel).

4.3. Lyα Forest Contamination

The Lyα forest was the largest contamination in the C IV doublet survey. Approximately 60% of the total path length resides in the Lyα forest. For most of these systems, the detection of associated transitions such as Lyα absorption or the Si IV doublet lent credibility to the C IV identification. For several of our systems, however, we did not have coverage of other transitions. An example of this scenario is the G = 1 doublet at $z_{1548} = 0.74843$ in the MARK132 sightline (which also had a nondescript profile; see Appendix A). For cases such as this, one must consider the possibility that a pair of Lyα lines mimicked a C IV doublet by chance. Instead of excluding systems where we did not have the wavelength coverage or data quality to detect associated transitions, we accounted for the contamination by considering the rate at which Lyα transitions masquerade as C IV.

In principle, the contamination rate could be addressed in a variety of ways. While we could have considered random lines of sight through cosmological simulations, our purpose was first to identify if contamination by Lyα was significant. We thus adopted the simpler approach of generating synthetic spectra from the known properties of Lyα statistics and searched this pure Lyα spectrum for putative C IV doublets. This approach had the advantages that artificial spectra were generated very quickly and we could assess our contamination in a Monte Carlo sense. Since the higher redshift E230M data were far more susceptible to contamination (the Lyα forest lies in the range $0.8 \lesssim z \lesssim 1.5$ in these data), we took the E230M wavelength range as our template.

In order to generate the spectra, we took the statistics of the Lyα forest from Janknecht et al. (2006). In the redshift range of interest, there was only very weak evolution of the Lyα line density, so for simplicity, we adopted a fixed line density[15] $d\mathcal{N}_{\rm Ly\alpha}/dz = 150$ for $13 \leqslant \log N_{\rm H\,I} \leqslant 16.5$. The column density and Doppler parameter distributions were taken to be a power law and truncated Gaussian, respectively, with

[15] Above $z \sim 1.5$, the Lyα line density evolves strongly (compare Kim et al. 2001).

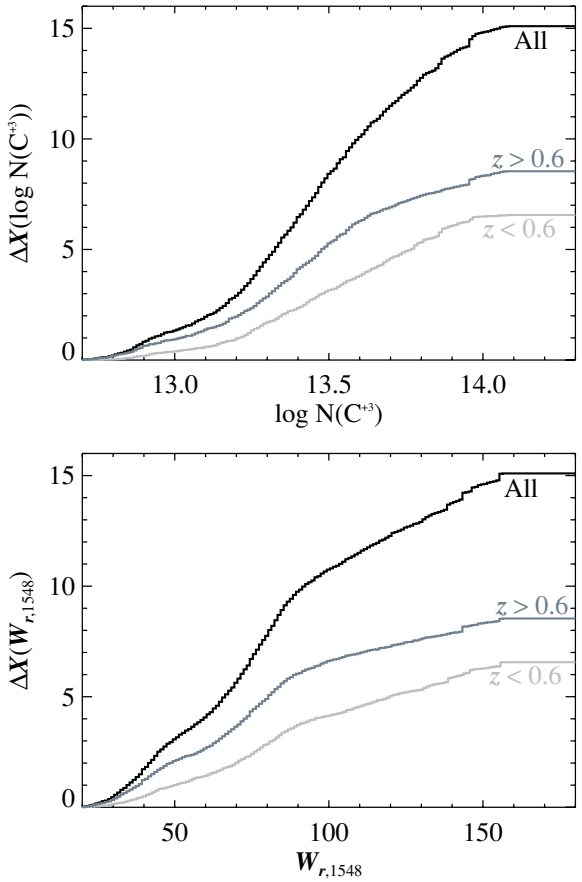

Figure 7. Redshift path length $\Delta X(\log N(C^{+3}))$ and $\Delta X(W_{r,1548})$ as a function of C IV 1548 column density (top) and equivalent width respectively (bottom). The black curve is for the full redshift ($z < 1$ sample), the light gray for $z < 0.6$, and the dark gray for $z \geqslant 0.6$. These estimates are based on Monte Carlo analysis and correspond to 95% completeness limits.

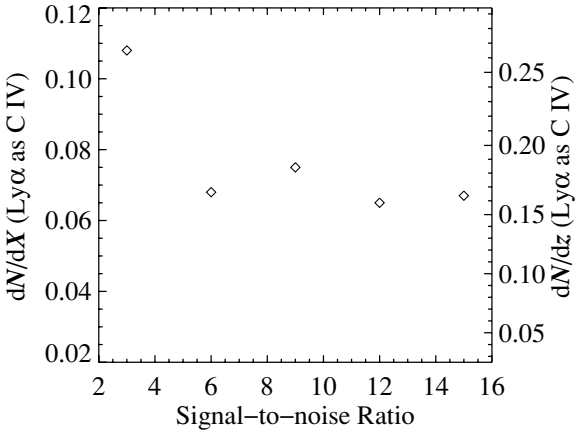

Figure 8. Rate of coincident Lyα forest lines misidentified as C IV doublets as a function of S/N. The Lyα forest at $0.8 \leqslant z \leqslant 1.5$ was simulated in a Monte Carlo fashion, and the incidence of Lyα forest lines that were "observed" to have similar line profiles and wavelength separation as a C IV doublet was estimated for a range of S/N.

the parameters from Janknecht et al. (2006). The placement of the Lyα lines was somewhat less clear. At high redshift, strong Lyα absorbers, identified in high-resolution data by the presence of C IV absorption, have been shown to be highly clustered (Fernández-Soto et al. 1996). By using heavier carbon atoms to trace the underlying gas component structure, those authors showed Lyα absorption to be highly clustered on small velocity scales. In the E230M data, however, we did not have the resolution to resolve such small-scale structure, and this was reflected in the lack of clustering detected in the UV data of Janknecht et al. (2006). In order to reproduce the observed trend as closely as possible, we thus distributed our Lyα lines in a uniform fashion. Further, since the observed statistics did not account for the small-scale blending mentioned above, we imposed a minimum separation for two lines $|\Delta z| > 7 \times 10^{-5}$. Finally, we added to our spectra the corresponding higher-order Lyman lines stronger than a nominal detection level of 15 mÅ, since they too could contribute to the contamination rate.

The line lists generated in the above fashion, which could be generated very quickly, constituted the full information available in a "spectrum." We thus adopted a Monte Carlo approach, which was appropriate for both low- and high-contamination rates. An automated set of criteria was used to select pairs of lines that could be misidentified as C IV doublets. We selected pairs of lines that lay within 30 km s^{-1} of the expected position, had b-values within 10 km s^{-1} of each other, and had an equivalent-width ratio between 2:1 and 1:1. These fake doublets were saved for further examination, and the simulation was iterated 1000 times.

For each misidentified doublet, an actual spectrum was generated, and noise added at the given S/N level. All the candidates were visually inspected to exclude clearly mismatched line pairs. The final number of accepted doublets was averaged over the 1000 simulation iterations, yielding $d\mathcal{N}_{\rm C\,IV}/dX$ for misidentified doublets. Since lines could be quickly generated, and noise easily added, we assessed the contamination rate at several S/N levels that spanned the range of typical values in our survey, with the results shown in Figure 8. In all cases, the contamination rate was not a significant effect, but in Section 6.5, we discuss several G = 2 C IV doublets that might be the result of Lyα forest contamination.

5. ANALYSIS

5.1. Frequency Distributions

The frequency distribution is the number of absorbers $\mathcal{N}$ per column density $N(C^{+3})$ or equivalent width $W_{r,1548}$ bin per absorption path length sensitive to those absorbers (see Section 4.1):

$$f(N(C^{+3})) \equiv \frac{\Delta\mathcal{N}}{\Delta N(C^{+3})\,\Delta X(N(C^{+3}))} \tag{11}$$

and

$$f(W_r) \equiv \frac{\Delta\mathcal{N}}{\Delta W_r\,\Delta X(W_r)}. \tag{12}$$

This quantity represents a nearly full description of an absorption line survey and is akin to the luminosity function as used in galaxy studies.

We chose to model the frequency distributions with power-law functions because it approximated the frequency distributions well. The power-law functions are of the form

$$f(N(C^{+3})) = k_{14}\left(\frac{N(C^{+3})}{N_0}\right)^{\alpha_N} \tag{13}$$

and

$$f(W_r) = k_3\left(\frac{W_r}{W_{r,0}}\right)^{\alpha_W}, \tag{14}$$

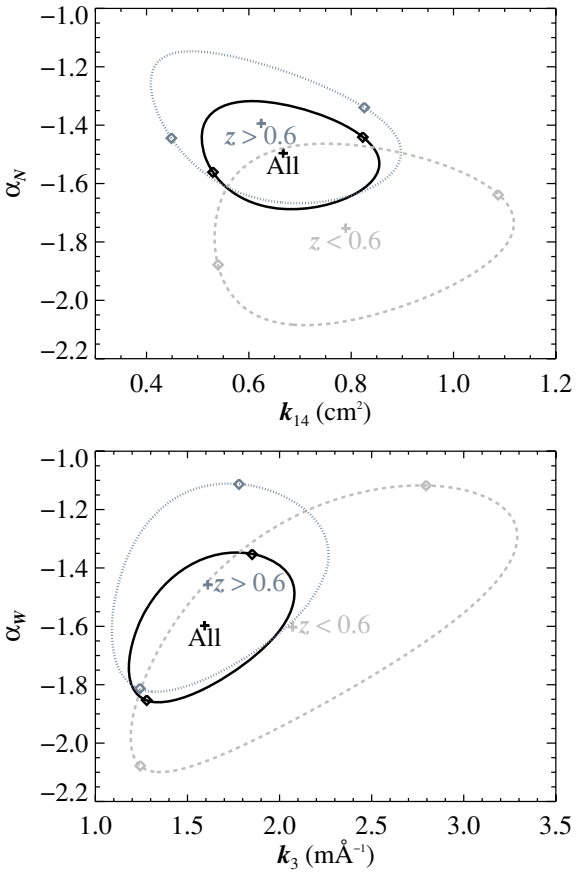

Figure 9. $f(N(C^{+3}))$ and $f(W_{r,1548})$ 1σ ellipses from the maximum likelihood analysis of the G = 1 sample. The sample was divided by redshift: $z < 1$ (black ellipse and points), $z < 0.6$ (light gray, dashed), and $0.6 \leqslant z < 1$ (gray, dotted). The plus signs indicate the best-fit values (see Tables 6 and 7). The diamonds indicate the coefficient and exponent that define the 1σ error on the integrated $\Omega_{C^{+3}}$ and/or $d\mathcal{N}_{C\,IV}/dX$. The coefficient k_{14} and the exponent α_N were not highly correlated for $f(N(C^{+3}))$ (top panel) due to the treatment of saturated absorbers in the maximum likelihood analysis (see Appendix B). The values were highly correlated for $f(W_{r,1548})$ (bottom panel).

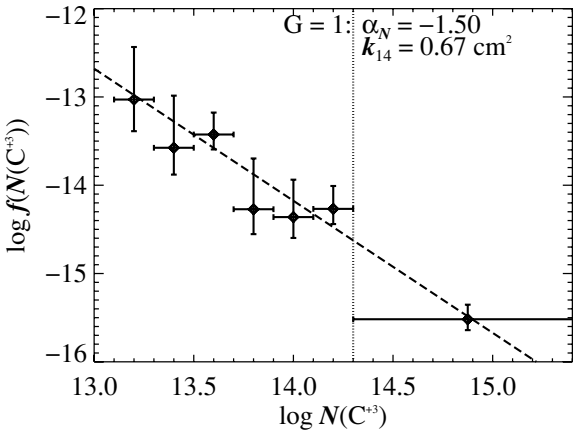

Figure 10. Column density frequency distribution for the full $z < 1$ sample. The G = 1 observations are the black diamonds, and the long-dash line indicates the best power-law fit. The observed and fitted G = 1+2 $f(N(C^{+3}))$ agrees very well. The AODM column densities are lower limits for saturated systems; our adopted saturation limit log $N(C^{+3}) = 14.3$ is indicated (vertical, dotted line).

where $N_0 = 10^{14}\,\mathrm{cm}^{-2}$ and $W_{r,0} = 400\,\mathrm{mÅ}$ and the subscripts on the coefficients k indicate the normalization (e.g., $k_{14} = k/10^{14}\,\mathrm{cm}^2$). We used the conjugate gradient method to maximize the likelihood function $\mathcal{L}$ and to simultaneously fit for the coefficient k and exponent α. From the 1σ error ellipse where $\ln\mathcal{L} - \ln\mathcal{L}_{\max} \geqslant -1.15$,[16] we estimated the errors in k and α (see Figure 9).

We derived $\mathcal{L}$ in a similar manner to that outlined in Storrie-Lombardi et al. (1996) and detailed in our Appendix B. The main difference was to include the observed number of strong, saturated absorbers, where we only had a lower-limit estimate of $N(C^{+3})$, as a constraint in $\mathcal{L}$. The best-fit power law must allow for a number of strong (saturated) absorbers consistent with the observed number. We set the saturation limit to log $N(C^{+3}) = 14.3$, which we determined empirically (see Figure 4). In the maximum likelihood analysis, the unsaturated doublets with log $N(C^{+3}) \geqslant 14.3$ were counted as saturated absorber, and the two saturated (G = 1+2) doublets with log $N(C^{+3}) < 14.3$ were excluded. Without the saturation term in $\mathcal{L}$, the best-fit α would have been significantly steeper, depending on the integration limits, since it would have been a strong statistical statement to not detect *any* strong absorbers.

For the same reason, the choice of integration limits in the maximum likelihood analysis influenced the result. We set the lower integration limit to the smallest observed value less 1σ for the sample analyzed, e.g., $N_{\min} - \sigma_{N,\min}$. For $f(N(C^{+3}))$, the saturation limit was $10^{14.3}\,\mathrm{cm}^{-2}$ and the upper limit "infinity" was $10^{16}\,\mathrm{cm}^{-2}$. For $f(W_{r,1548})$, the upper limit was the largest observed value plus $1\sigma\, W_{r,\max} + \sigma_{W_r,\max}$.

The best-fit power-law $f(N(C^{+3}))$ for the G = 1 and the G = 1+2 samples are shown in Figure 10 and enumerated in Table 6. For the results of the maximum likelihood analysis of $f(W_{r,1548})$, see Table 7. They were consistent within the errors. To examine the temporal evolution of C IV absorbers in our survey, we divided the G = 1 sample into two redshift bins, defined by, approximately, the median redshift: $z_{1548} < 0.6$ and $0.6 \leqslant z < 1$ (see Figure 11).

We performed a jack-knife re-sampling analysis to estimate the errors of and correlation between k and α from our maximum likelihood analyses. For the jack-knife, each C IV doublet i was excluded from the full sample of $\mathcal{N}$ absorbers. Then, the frequency distributions $f(N(C^{+3}))$ and $f(W_{r,1548})$ were re-fit with integration limits set as described previously. This was done for the G = 1 and G = 1+2 samples for all three redshift cuts ($z_{1548} < 1$, < 0.6, and $\geqslant 0.6$; see Table 8). The variance in the, e.g., coefficient distribution k_i from the jack-knife is

$$\sigma_{k_i}^2 = \frac{1}{\mathcal{N}-1}\sum_i^{\mathcal{N}}(k_i - \langle k\rangle)^2, \tag{15}$$

where $\langle k\rangle$ is the mean of the best-fit values from the re-sampling analysis. The same applies to the exponent distribution α_i. The mean coefficients and exponents from the maximum likelihood analyses to the various redshift samples agreed with the results from the analyses of the full samples (i.e., compare Tables 6 and 7 with Table 8).

The correlation between the parameters k_i and α_i is the ratio of the covariance to the product of σ_{k_i} and σ_{α_i}:

$$r_{k_i,\alpha_i} = \frac{\mathcal{N}-1}{\mathcal{N}}\frac{\sum_i^{\mathcal{N}}(k_i - \langle k\rangle)(\alpha_i - \langle\alpha_i\rangle)}{\sigma_{k_i}\sigma_{\alpha_i}}. \tag{16}$$

[16] We empirically determined the $\ln\mathcal{L} - \ln\mathcal{L}_{\max} \geqslant -1.15$ constraint. This limit defines a contour that contains 68.3% of the likelihood surface. For a Gaussian distribution, the 1σ contour would be defined by $\ln\mathcal{L} - \ln\mathcal{L}_{\max} \geqslant -0.5$.

Table 6
$f(N(C^{+3}))$, $d\mathcal{N}_{C\,IV}/dX$, and $\Omega_{C^{+3}}$ Summary

(1) G	(2) $\langle z\rangle$	(3) z_l	(4) z_h	(5) $\mathcal{N}$	(6) $\log N(C^{+3})$	(7) $d\mathcal{N}_{C\,IV}/dz$	(8) $d\mathcal{N}_{C\,IV}/dX$	(9) $\Omega_{C^{+3}}$ (10^{-8})	(10) k_{14} (cm^2)	(11) α_N	(12) P_{KS}
Samples by Redshift											
1	0.65355	0.00574	0.95269	36	(13.15, 16.00)	$8.0^{+2.5}_{-2.0}$	$4.2^{+1.3}_{-1.0}$	$6.20^{+1.82}_{-1.52}$	$0.67^{+0.18}_{-0.16}$	$-1.50^{+0.17}_{-0.19}$	0.364
	0.65355	0.00427	0.95269	27	(13.20, 15.39)	$6.0^{+1.2}_{-1.0}$	$3.5^{+0.7}_{-0.6}$	>3.43	...	...	...
1+2	0.65355	0.00574	0.95269	41	(13.15, 16.00)	$9.3^{+2.7}_{-2.2}$	$4.9^{+1.4}_{-1.1}$	$6.99^{+1.91}_{-1.61}$	$0.76^{+0.20}_{-0.17}$	$-1.52^{+0.16}_{-0.18}$	0.484
	0.65355	0.00427	0.95269	32	(13.20, 15.39)	$7.0^{+1.3}_{-1.1}$	$4.1^{+0.7}_{-0.6}$	>4.13	...	...	...
1	0.38152	0.00574	0.57632	17	(13.15, 16.00)	$9.3^{+5.3}_{-3.4}$	$5.9^{+3.4}_{-2.2}$	$6.24^{+2.88}_{-2.14}$	$0.79^{+0.32}_{-0.25}$	$-1.75^{+0.28}_{-0.33}$	0.234
	0.38152	0.00427	0.57632	15	(13.20, 14.75)	$6.8^{+2.1}_{-1.6}$	$5.0^{+1.5}_{-1.2}$	>4.81	...	...	...
1+2	0.40227	0.00574	0.57632	19	(13.15, 16.00)	$10.5^{+5.6}_{-3.7}$	$6.6^{+3.5}_{-2.3}$	$7.01^{+3.05}_{-2.30}$	$0.88^{+0.33}_{-0.27}$	$-1.74^{+0.28}_{-0.31}$	0.049
	0.40227	0.00427	0.57632	17	(13.20, 14.75)	$8.0^{+2.3}_{-1.9}$	$6.0^{+1.7}_{-1.4}$	>5.64	...	...	...
1	0.78567	0.65126	0.95269	19	(13.37, 16.00)	$8.1^{+3.7}_{-2.5}$	$3.9^{+1.8}_{-1.2}$	$6.35^{+2.52}_{-1.99}$	$0.62^{+0.27}_{-0.21}$	$-1.39^{+0.24}_{-0.27}$	0.268
	0.81814	0.65126	0.95269	12	(13.40, 15.39)	$5.6^{+1.6}_{-1.2}$	$2.7^{+0.8}_{-0.6}$	>2.48	...	...	...
1+2	0.81814	0.65126	0.95269	22	(13.37, 16.00)	$9.8^{+4.4}_{-3.0}$	$4.7^{+2.1}_{-1.4}$	$7.23^{+2.65}_{-2.14}$	$0.75^{+0.28}_{-0.23}$	$-1.45^{+0.23}_{-0.25}$	0.263
	0.81814	0.65126	0.95269	15	(13.40, 15.39)	$6.4^{+1.6}_{-1.3}$	$3.1^{+0.8}_{-0.6}$	>3.10	...	...	...
Samples by Instrument											
E140M	0.06351	0.00574	0.08091	7	(13.15, 14.25)	$10.5^{+11.8}_{-5.4}$	$9.6^{+10.7}_{-4.9}$	$5.65^{+11.79}_{-2.91}$	$0.73^{+1.05}_{-0.51}$	$-2.19^{+0.88}_{-0.95}$	0.281
	0.06351	0.00427	0.08091	7	(13.20, 14.17)	$7.7^{+3.9}_{-2.7}$	$7.2^{+3.6}_{-2.6}$	>3.74	...	...	...
E230M	0.73910	0.24010	0.95269	34	(13.14, 16.00)	$9.2^{+2.7}_{-2.2}$	$4.6^{+1.4}_{-1.1}$	$7.51^{+2.18}_{-1.83}$	$0.73^{+0.22}_{-0.18}$	$-1.38^{+0.17}_{-0.19}$	0.160
	0.73910	0.24010	0.95269	25	(13.25, 15.39)	$6.9^{+1.4}_{-1.2}$	$3.6^{+0.7}_{-0.6}$	>4.32	...	...	...

Notes. Parameters from the maximum likelihood analysis for $f(N(C^{+3})) = k_{14}\,(N(C^{+3})/N_0)^{\alpha_N}$, where $\log N_0 = 14$. The C IV doublets were divided into several subsamples by the group G and the redshift range. For each subsample, the first line refers to the maximum likelihood analysis and the second line, to the observed quantities. $d\mathcal{N}_{C\,IV}/dX$, listed in the first subsample row, is the integral of $f(N(C^{+3}))$ from $\log N(C^{+3}) = 13$ to infinity with the best-fit k_{14} and α_N (see Equation (18)). Also in the first subsample row, the integrated $d\mathcal{N}_{C\,IV}/dz \equiv d\mathcal{N}_{C\,IV}/dX \cdot dX/dz$, where the latter term is the derivative of Equation (9), evaluated at $\langle z\rangle$. The observed $d\mathcal{N}_{C\,IV}/dz$ and $d\mathcal{N}_{C\,IV}/dX$ are from the sum of the *total* number of doublets, weighted by the path length available to detect the doublet (based on its $N(C^{+3})$; see Equation (17)). $\Omega_{C^{+3}}$, listed in the first subsample row, is the integral of $f(N(C^{+3})) \cdot N(C^{+3})$ from $13 \leqslant \log N(C^{+3}) \leqslant 15$ with the best-fit k_{14} and α_N (see Equation (22)). The observed $\Omega_{C^{+3}}$ were from the sum of the *unsaturated* doublets, as given by $\mathcal{N}$ (see Equation (20)). P_{KS} is the significance of the one-sided K–S statistic of the best-fit power law.

The coefficient and exponent were strongly correlated for the $f(W_{r,1548})$ power-law fits (i.e., $r_{k_i,\alpha_i} \approx 1$). By accounting for the saturated doublets in the maximum likelihood function, k_{14} and α_N were less correlated for the $f(N(C^{+3}))$ fits.

Since C IV absorbers cluster (Fernández-Soto et al. 1996), we also performed a jack-knife of the sightline and iteratively fit the frequency distributions after excluding all absorbers from each sightline. The results are compiled in Table 9; they agree well with results for the full sample (Tables 6 and 7). We did not re-estimate ΔX without the excluded sightline since each sightline contributes $\lesssim$10% to ΔX of any redshift range.

5.2. C IV Absorber Line Density

We measured the density of C IV doublets with a minimum column density as follows:

$$\frac{d\mathcal{N}_{C\,IV}}{dX}(N(C^{+3}) \geqslant N_{lim}) = \sum_{N_i \geqslant N_{lim}} \frac{1}{\Delta X(N_i)} \qquad (17)$$

$$\sigma^2_{d\mathcal{N}/dX} = \sum_{N_i \geqslant N_{lim}} \left(\frac{\sigma_{\Delta X}}{\Delta X(N_i)^2}\right)^2.$$

The absorber line density can be measured for any equivalent width limit in a similar fashion. We estimated the contribution of the low-number statistics in $\mathcal{N}$ by adding the Poisson counting variance to $\sigma^2_{d\mathcal{N}/dX}$. In Figure 12, we show $d\mathcal{N}_{C\,IV}/dX$ for the full G = 1 and G = 1+2 samples as functions of column density (top panel) and equivalent width (bottom panel). The weakest system we found had $\log N(C^{+3}) = 13.2$ and $W_{r,1548} = 52$ mÅ. At this limit, $d\mathcal{N}_{C\,IV}/dX = 4.1^{+0.7}_{-0.6}$ for the G = 1+2 sample.

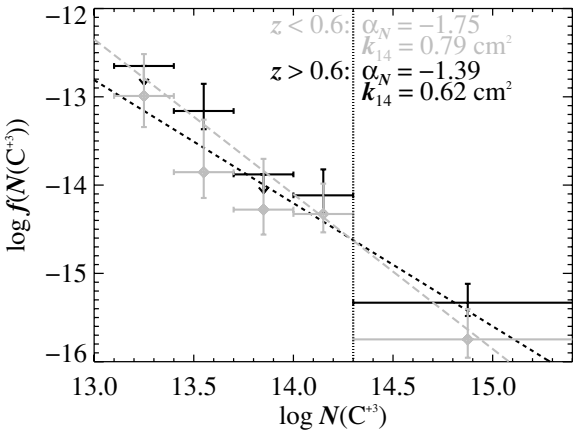

Figure 11. Column density frequency distribution for two redshift bins of the G = 1 sample. The best-fit α_N for the $z_{1548} < 0.6$ $f(N(C^{+3}))$ (black, long-dash line) is steeper than that for the $0.6 \leqslant z_{1548} < 1$ bin (gray, dashed line). As in Figure 10, the best-fit α_N and k_{14} from the maximum likelihood analysis are shown, as is the saturation limit $\log N(C^{+3}) = 14.3$ (vertical, dotted line).

In Figure 12, we extrapolated our $d\mathcal{N}_{C\,IV}/dX$ to lower $N(C^{+3})$ and W_r by integrating the power-law fits of the frequency

Table 7
$f(W_{r,1548})$ and $d\mathcal{N}_{\rm C\,IV}/dX$ Summary

(1) G	(2) $\langle z\rangle$	(3) z_l	(4) z_h	(5) $\mathcal{N}$	(6) $W_{r,1548}$ (mÅ)	(7) $d\mathcal{N}_{\rm C\,IV}/dz$	(8) $d\mathcal{N}_{\rm C\,IV}/dX$	(9) k_3 (mÅ^{-1})	(10) α_W	(11) $P_{\rm KS}$
Samples by Redshift										
1	0.65355	0.00427	0.95269	38	(47, 2423)	$7.0^{+1.9}_{-1.6}$	$3.7^{+1.0}_{-0.8}$	$1.59^{+0.47}_{-0.40}$	$-1.60^{+0.25}_{-0.26}$	0.714
					(53, 2363)	$5.7^{+1.1}_{-0.9}$	$3.4^{+0.7}_{-0.6}$	...	...	...
1+2	0.65355	0.00427	0.95269	43	(37, 2423)	$7.8^{+2.3}_{-1.7}$	$4.1^{+1.2}_{-0.9}$	$1.78^{+0.53}_{-0.42}$	$-1.57^{+0.22}_{-0.23}$	0.374
					(52, 2363)	$6.7^{+1.2}_{-1.1}$	$3.9^{+0.7}_{-0.6}$	...	...	...
1	0.38152	0.00427	0.57632	18	(47, 896)	$7.5^{+11.5}_{-2.4}$	$4.8^{+7.3}_{-1.6}$	$2.07^{+1.21}_{-0.88}$	$-1.60^{+0.48}_{-0.49}$	0.200
					(53, 852)	$6.2^{+1.9}_{-1.5}$	$4.6^{+1.4}_{-1.1}$	...	...	...
1+2	0.40227	0.00427	0.57632	20	(37, 896)	$8.4^{+11.0}_{-2.6}$	$5.3^{+6.9}_{-1.7}$	$2.29^{+1.26}_{-0.91}$	$-1.58^{+0.44}_{-0.45}$	0.038
					(52, 852)	$7.7^{+2.3}_{-1.9}$	$5.7^{+1.7}_{-1.4}$	...	...	...
1	0.81814	0.65126	0.95269	20	(61, 2423)	$7.6^{+9.0}_{-2.4}$	$3.6^{+4.3}_{-1.1}$	$1.61^{+0.65}_{-0.52}$	$-1.46^{+0.34}_{-0.36}$	0.501
					(67, 2363)	$5.5^{+1.5}_{-1.2}$	$2.7^{+0.8}_{-0.6}$	...	...	...
1+2	0.81814	0.65126	0.95269	23	(61, 2423)	$8.7^{+6.2}_{-2.5}$	$4.1^{+2.9}_{-1.2}$	$1.83^{+0.69}_{-0.55}$	$-1.49^{+0.32}_{-0.34}$	0.624
					(67, 2363)	$6.3^{+1.6}_{-1.3}$	$3.1^{+0.8}_{-0.6}$	...	...	...
Samples by Instrument										
E140M	0.06351	0.00427	0.08091	8	(47, 315)	≈ 7.4	≈ 6.7	$2.36^{+6.29}_{-1.87}$	$-1.89^{+1.09}_{-1.11}$	0.248
					(53, 264)	$6.6^{+3.6}_{-2.5}$	$6.1^{+3.4}_{-2.3}$	...	...	...
E230M	0.73910	0.24010	0.95269	35	(37, 2423)	$8.7^{+5.1}_{-2.2}$	$4.3^{+2.5}_{-1.1}$	$1.90^{+0.56}_{-0.48}$	$-1.42^{+0.24}_{-0.25}$	0.355
					(52, 852)	$5.2^{+1.3}_{-1.1}$	$2.7^{+0.7}_{-0.6}$	...	...	...

Notes. Parameters from the maximum likelihood analysis for $f(W_r) = k_3\,(W_r/W_{r,0})^{\alpha_W}$, where $W_{r,0} = 400$ mÅ. The tabulated information is similar to that presented in Table 6, except that the integrated line density limit is $W_r = 50$ mÅ.

Table 8
$f(N(\mathrm{C}^{+3}))$ and $f(W_{r,1548})$ Correlation Matrices by Absorber

G	z	$f(N(\mathrm{C}^{+3}))$ $\langle k_{14}\rangle$ (cm^2)	$\langle\alpha_N\rangle$	r_{k_i,α_i}	$f(W_{r,1548})$ $\langle k_3\rangle$ (mÅ^{-1})	$\langle\alpha_W\rangle$	r_{k_i,α_i}
1	<1	0.65 ± 0.04	−1.50 ± 0.12	−0.63	1.57 ± 0.62	−1.59 ± 0.33	0.97
1+2	<1	0.75 ± 0.04	−1.52 ± 0.12	−0.69	1.76 ± 0.72	−1.56 ± 0.33	0.97
1	<0.6	0.75 ± 0.05	−1.76 ± 0.21	0.43	1.96 ± 0.49	−1.60 ± 0.34	0.99
1+2	<0.6	0.84 ± 0.05	−1.74 ± 0.22	0.33	2.18 ± 0.51	−1.58 ± 0.31	0.99
1	>0.6	0.60 ± 0.11	−1.40 ± 0.17	−0.78	1.57 ± 0.66	−1.44 ± 0.38	0.87
1+2	>0.6	0.72 ± 0.13	−1.46 ± 0.16	−0.76	1.79 ± 0.81	−1.47 ± 0.41	0.88

Notes. Mean values and correlation coefficient from jack-knife analysis of power-law fit to $f(N(\mathrm{C}^{+3}))$ and $f(W_r)$. Each absorber was iteratively excluded from the maximum likelihood analysis of the frequency distributions.

Table 9
$f(N(\mathrm{C}^{+3}))$ and $f(W_{r,1548})$ Correlation Matrices by Sightline

G	z	$f(N(\mathrm{C}^{+3}))$ $\langle k_{14}\rangle$ (cm^2)	$\langle\alpha_N\rangle$	r_{k_i,α_i}	$f(W_{r,1548})$ $\langle k_3\rangle$ (mÅ^{-1})	$\langle\alpha_W\rangle$	r_{k_i,α_i}
1	<1	0.63 ± 0.11	−1.50 ± 0.10	−0.12	1.54 ± 0.62	−1.58 ± 0.31	0.88
1+2	<1	0.73 ± 0.11	−1.52 ± 0.10	−0.14	1.73 ± 0.67	−1.55 ± 0.32	0.92
1	<0.6	0.72 ± 0.20	−1.76 ± 0.27	0.70	1.89 ± 0.80	−1.61 ± 0.39	0.94
1+2	<0.6	0.81 ± 0.20	−1.75 ± 0.27	0.45	2.11 ± 0.79	−1.58 ± 0.37	0.91
1	>0.6	0.56 ± 0.11	−1.40 ± 0.18	−0.72	1.52 ± 0.60	−1.43 ± 0.37	0.82
1+2	>0.6	0.69 ± 0.09	−1.46 ± 0.14	−0.39	1.75 ± 0.65	−1.46 ± 0.41	0.90

Notes. Mean values and correlation coefficient from jack-knife analysis of power-law fit to $f(N(\mathrm{C}^{+3}))$ and $f(W_r)$. All absorbers from each sightline were iteratively excluded from the maximum likelihood analysis of the frequency distributions.

distribution over, e.g., $N_{\rm lim} \leqslant N(\mathrm{C}^{+3}) < \infty$:

$$\frac{d\mathcal{N}_{\rm C\,IV}}{dX}(N(\mathrm{C}^{+3}) \geqslant N_{\rm lim}) = -\frac{k_{14}}{1+\alpha_N}\frac{N_{\rm lim}^{1+\alpha_N}}{N_0^{\alpha_N}}. \qquad (18)$$

The summed and integrated C IV absorber line density by $N(\mathrm{C}^{+3})$ and $W_{r,1548}$ are listed in Tables 6 and 7, respectively. The error in $d\mathcal{N}_{\rm C\,IV}/dX$ from the power-law model of $f(N(\mathrm{C}^{+3}))$

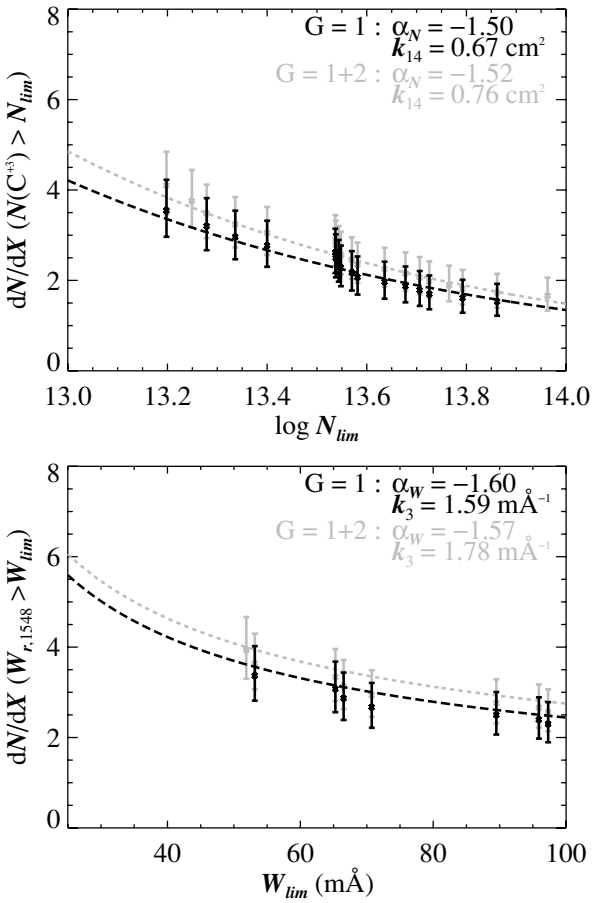

Figure 12. Absorber line density as a function of $N(C^{+3})$ and $W_{r,1548}$. The summed $d\mathcal{N}_{CIV}/dX$ from the G = 1 and 1+2 groups are shown with the solid black and gray crosses, respectively (see Equation 17). The dashed lines show the integrated $d\mathcal{N}_{CIV}/dX$ from the fits to $f(N(C^{+3}))$ and $f(W_{r,1548})$ (see Equation (18)).

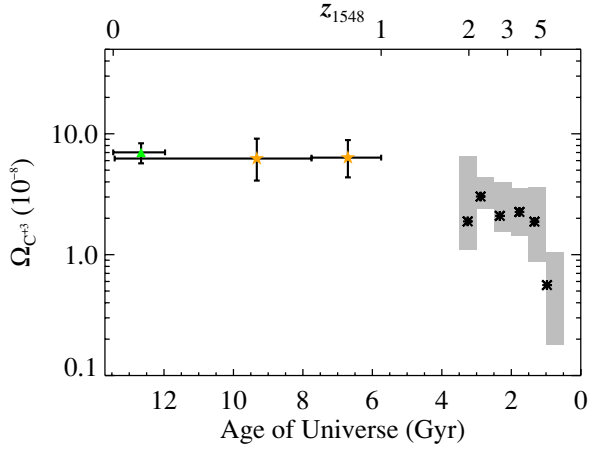

Figure 13. C^{+3} mass density relative to the critical density over age of universe. The integrated $\Omega_{C^{+3}}$ (see Equation 22) for the G = 1 sample, divided by redshift, are the (orange) stars. The value from Danforth & Shull (2008) is the (green) triangle and is not an independent measurement of $\Omega_{C^{+3}}$. The gray boxes indicate the binned, cosmology-adjusted $\Omega_{C^{+3}}$ from several high-redshift studies: Songaila (2001); Pettini et al. (2003); Boksenberg et al. (2003); Scannapieco et al. (2006); Becker et al. (2009); and Ryan-Weber et al. (2009) (see Appendix C). The horizontal extent of the boxes indicate the bin size. The vertical extent represents the maximum range spanned by $\Omega_{C^{+3}} \pm \sigma_\Omega$ (the published errors were adjusted to be 1σ, as necessary). The average time and error-weighted $\Omega_{C^{+3}}$ per bin are shown with black asterisks.

(A color version of this figure is available in the online journal.)

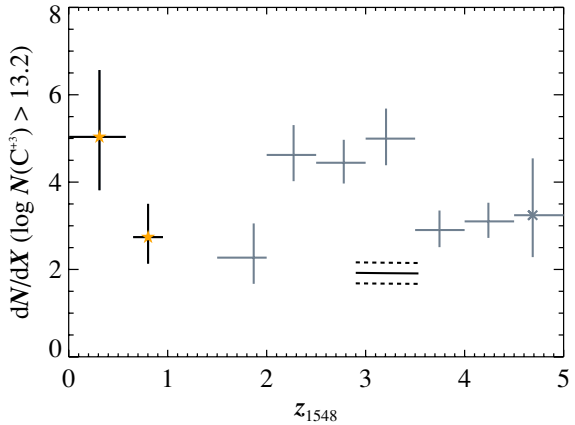

Figure 14. $d\mathcal{N}_{CIV}/dX$ as a function of redshift. The number density of C IV absorbers has not changed significantly since $z = 5$. The (orange) stars are our summed $z < 1$ values for $\log N(C^{+3}) \geqslant 13.2$ (see Equation 17). The solid and dashed horizontal lines are the integrated $d\mathcal{N}_{CIV}/dX$ and 1σ error, respectively, from the best-fit $f(N)$ from Songaila (2001). She only fit her $2.9 \leqslant z \leqslant 3.54$ observations, but the result agreed with the full $1.5 \leqslant z \leqslant 5$ sample. For reference, $d\mathcal{N}_{CIV}/dX \equiv \mathcal{N}/\Delta X$ from the tabulated $\mathcal{N}$ and ΔX in Songaila (2001, $12 \leqslant \log N(C^{+3}) \leqslant 14.9$) and Pettini et al. (2003, $12.5 \leqslant \log N(C^{+3}) \leqslant 14$) are shown with the gray pluses and cross, respectively; the error bars assume Poisson counting statistics on $\mathcal{N}$. We have adjusted ΔX for differences in cosmology (see Appendix C).

(A color version of this figure is available in the online journal.)

was defined by the error ellipse in the maximum likelihood analysis. However, the extrema in $d\mathcal{N}_{CIV}/dX$ allowed by the 1σ ellipse did not occur at the extrema of k_{14} and α_N. As shown in Figure 9 (bottom panel), the extrema in the 1σ-allowed values of $d\mathcal{N}_{CIV}/dX$ occurred on the sides of the ellipse where k_{14} and α_N were maximized (or minimized). Again, the equations are similar for line density as a function of equivalent width.

5.3. C^{+3} Mass Density

In principle, $\Omega_{C^{+3}}$ is the ratio of the mass in C^{+3} ions relative to the critical density $\rho_{c,0}$. In practice, the observations limit $\Omega_{C^{+3}}$ to include only C IV absorbers within a range of column densities. The lower $N(C^{+3})$ bound reflects the limit where the observations can confidently detect and identify C IV doublets, typically $N_{min} \approx 10^{13}$ cm^{-2}. The upper bound is usually $N_{max} = 10^{15}$ cm^{-2}. Doublets with $\log N(C^{+3}) > 15$ are rare and often associated with galaxies (for example, the DLA C IV doublet toward PG1206+459 with $\log N(C^{+3}) > 15.4$). In addition, there has been no observed break in $f(N(C^{+3}))$, so the integrated $\Omega_{C^{+3}}$ is infinite.

The metallicity and ionizing background of the intergalactic medium affect the C^{+3} mass density, and the observed evolution of $\Omega_{C^{+3}}$ over time (or redshift) add a constraint to the changes in the cosmic metallicity and ionizing background. While one expects that the former increases monotonically with time, the latter is believed to be decreasing since $z \approx 1$. $\Omega_{C^{+3}}$ is the integrated column density-"weighted" frequency distribution $f(N(C^{+3}))$:

$$\Omega_{C^{+3}} = \frac{H_0\, m_C}{c\, \rho_{c,0}} \int_{N_{min}}^{N_{max}} f(N(C^{+3}))\, N(C^{+3})\, d\, N(C^{+3}), \qquad (19)$$

where $H_0 = 70$ km s^{-1} Mpc^{-1} is the Hubble constant today; $m_C = 2 \times 10^{-23}$ g is the mass of the carbon atom; c is the speed of light; and $\rho_{c,0} = 3H_0^2(8\pi G)^{-1} = 9.26 \times 10^{-30}$ g cm^{-3} for our assumed Hubble constant.

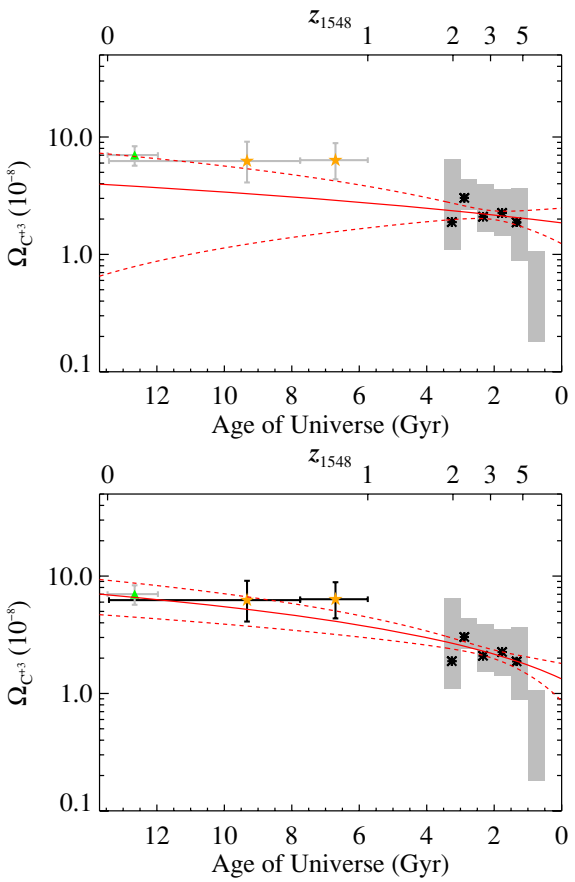

Figure 15. Linear regressions of $\Omega_{C^{+3}}$ over age of universe. The (red) dashed lines are the χ^2-minimization fit to subsets of the data described in Figure 13, and the (red) dotted lines indicate the 1σ range of the model. In the upper panel, the slope for the $1 < z < 5$ fit is consistent with no evolution $a_1 = (0.15 \pm 0.3) \times 10^{-8}$ Gyr^{-1}. For $z < 5$, in the lower panel, the slope is $a_1 = (0.42 \pm 0.2) \times 10^{-8}$ Gyr^{-1}. The evidence that the C^{+3} mass density has been slowly increasing since ≈1 Gyr requires the measurements at low redshift. (A color version of this figure is available in the online journal.)

The observed $\Omega_{C^{+3}}$ can be approximated by the sum of the detected C IV absorbers:

$$\Omega_{C^{+3}} = \frac{H_0\, m_C}{c\, \rho_{c,0}} \sum_{\mathcal{N}} \frac{N(C^{+3})}{\Delta X(N(C^{+3}))} \tag{20}$$

$$\sigma_\Omega^2 = \left(\frac{H_0\, m_C}{c\, \rho_{c,0}}\right)^2 \left(\sum_{\mathcal{N}} \left(\frac{\sigma_{N(C^{+3})}}{\Delta X(N(C^{+3}))} \right)^2 + \sum_{\mathcal{N}} \left(\frac{N(C^{+3})\sigma_{\Delta X}}{\Delta X(N(C^{+3}))} \right)^2 \right) \tag{21}$$

(Lanzetta et al. 1991). We list the summed $\Omega_{C^{+3}}$ values for various redshift samples in Table 6. We only include absorbers that are unsaturated in at least one line, typically with $\log N(C^{+3}) < 14.3$, because we only have a lower limit to $N(C^{+3})$ for saturated absorbers. Therefore, the *summed* $\Omega_{C^{+3}}$ is a lower limit, since some saturated absorbers may have $\log N(C^{+3}) \leqslant 15$ and could have been included in the $\Omega_{C^{+3}}$ sum.

To measure a value for $\Omega_{C^{+3}}$, we use our best-fit $f(N(C^{+3}))$ power law (Equation (13)) and integrate Equation (19) analytically:

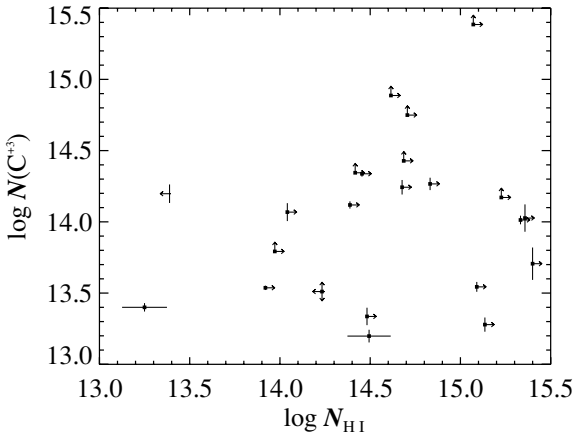

Figure 16. C^{+3} and H I column densities. The symbols indicate the location or limit of all C IV doublets with both lines detected at $W_r \geqslant 3\sigma_{W_r}$ and with Lyα coverage. When possible, the H I column densities included the constraint given by Lyβ detection. The G = 1 sample are highlighted by the filled black square. The upper limits are 2σ.

$$\Omega_{C^{+3}} = \frac{H_0\, m_C}{c\, \rho_{c,0}} \frac{10^{-14} k_{14}}{2+\alpha_N} \left(\frac{N_{max}^{2+\alpha_N} - N_{min}^{2+\alpha_N}}{N_0^{\alpha_N}} \right). \tag{22}$$

With this, we can measure $\Omega_{C^{+3}}$ over the column density range of unsaturated and saturated absorbers or even extrapolate the model to different ranges. Like the errors for $d\mathcal{N}_{C\,IV}/dX$ (see Section 5.2, the errors for the integrated $\Omega_{C^{+3}}$ were taken as the extrema of the 1σ $f(N(C^{+3}))$ error ellipses (see top panel, Figure 9).

The choice for the limits of integration N_{min} to N_{max} was critical, since there has been no observed downturn in $f(N(C^{+3}))$, measured at any redshift. We used $13 \leqslant \log N(C^{+3}) \leqslant 15$ in our analysis (see Table 6 and Figures 13 and 15) because this range reflects that of the observed column densities and overlapped with the majority of studies used for comparison (e.g., Songaila 2001). The integrated $\Omega_{C^{+3}}$ is most influenced by the strongest absorbers, because they contain substantially more mass. For example, according to Equation 22 and with $\alpha_N = -1.5$, the $14.3 \leqslant \log N(C^{+3}) \leqslant 15$ component contributes ≈60% of $\Omega_{C^{+3}}$, integrated over the range $13 \leqslant \log N(C^{+3}) \leqslant 15$. In comparison, the $13 \leqslant \log N(C^{+3}) \leqslant 13.7$ component accounts for ≈14%. The proportions change as the power-law exponent changes, increasing the lower column density contribution as α_N decreases. A detailed discussion of the effects of the column density range on the summed $\Omega_{C^{+3}}$ is given in Appendix C.

6. DISCUSSION

6.1. Comparisons with Previous Results

In Danforth & Shull (2008), $d\mathcal{N}_{C\,IV}/dz = 10^{+4}_{-2}$ for $W_r \geqslant 30$ mÅ. They measured the absorber line density by summing their observed number of doublets (24) and dividing by the unblocked redshift path length ($\Delta z = 2.42$). They estimated Δz by identifying regions of the spectra where the C IV 1548 line could be detected at $W_r \geqslant 4\sigma_{W_r}$ and 1550 at $\geqslant 2\sigma_{W_r}$. We measure $d\mathcal{N}_{C\,IV}/dz = 6.2^{+1.9}_{-1.6}$ for the $z < 0.6$, G = 1 doublets with $W_{r,1548} \geqslant 53$ mÅ (see Table 6). The $>1\sigma$ difference between our $d\mathcal{N}_{C\,IV}/dz$ values is largely due to the equivalent width limit. For $W_r \geqslant 50$ mÅ, $d\mathcal{N}_{C\,IV}/dz = 7^{+3}_{-2}$ (C. Danforth 2009, private

A. Velocity Plots

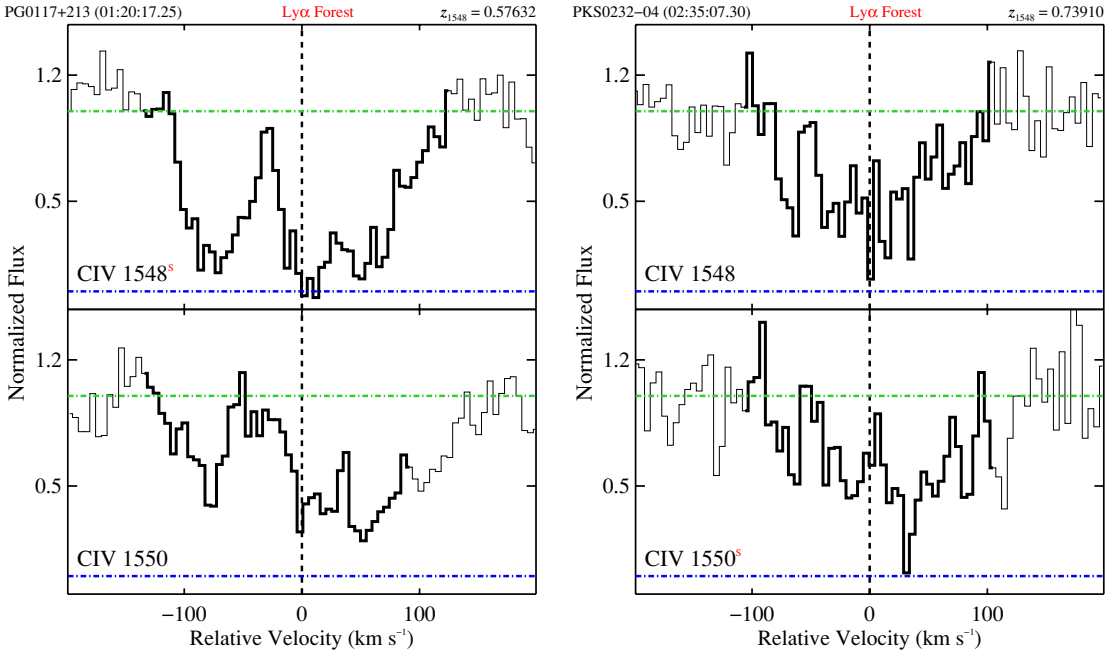

Figure 17. Velocity plots of G = 1 C IV systems. The regions of spectra around each absorption line are aligned in velocity space with respect to the rest wavelength of the transition and z_{1548}. Saturated transitions are indicated with the (red) "S"; transitions with $N(C^{+3}) < 3\sigma_{N(C^{+3})}$ are indicated with the (red) "W." The regions used to measure W_r and log N are shown by the dark outline. The flux at zero and unity are shown with the dash–dot lines (blue and green, respectively); the (black) vertical dashed line indicates $v = 0\,\mathrm{km\,s^{-1}}$.

(A color version of this figure is available in the online journal.)

communication), which is within 0.3σ of our value. Another source for the discrepancy is the detection criterion used (e.g., both lines detected with $W_r \geqslant 3\sigma_{W_r}$), which would affect the number of doublets included and the unblocked redshift path length.[17]

The C IV absorber line density has not changed significantly since $z = 5$ for $\log N(C^{+3}) \geqslant 13$ absorbers. Songaila (2001) and Boksenberg et al. (2003) did not detect any redshift evolution for $\log N(C^{+3}) \geqslant 13$ doublets over $1.5 \lesssim z \lesssim 4.5$; they measured $d\mathcal{N}_{\mathrm{CIV}}/dX \approx 3$. In Figure 14, we compare the $d\mathcal{N}_{\mathrm{CIV}}/dX$ measurements from Songaila (2001) with the current study. In order to compare $d\mathcal{N}_{\mathrm{CIV}}/dX$ for $\log N(C^{+3}) \geqslant 13.2$, we use the best-fit coefficient ($k_{14} = 0.63\,\mathrm{cm}^2$) and exponent ($\alpha_N = -1.8 \pm 0.1$) from Songaila (2001) in Equation (18): $d\mathcal{N}_{\mathrm{CIV}}/dX = 1.9 \pm 0.2$ (adjusted for cosmology). For the current survey, the summed absorber line density is $d\mathcal{N}_{\mathrm{CIV}}/dX = 3.4^{+0.7}_{-0.6}$ at $\langle z \rangle = 0.654$. This is a 1.8 ± 0.4 increase over the integrated $d\mathcal{N}_{\mathrm{CIV}}/dX$ value from Songaila (2001). However, since she did not provide an error for the coefficient, we likely underestimate her error on $d\mathcal{N}_{\mathrm{CIV}}/dX$ above.

The best-fit $\alpha_N = -1.75^{+0.28}_{-0.331}$ for the lower-redshift bin was consistent with $\alpha_N = -1.79 \pm 0.17$ from Danforth & Shull (2008), which covered $z_{1548} < 0.12$.

There has been no consensus on the best power-law exponent for $f(N(C^{+3}))$ at $z > 1$. Songaila (2001) and Boksenberg et al. (2003) conducted surveys similar to the current study, and they measured $\alpha_N = -1.8 \pm 0.1$ ($2.9 \leqslant z \leqslant 3.54$) and $\alpha_N = -1.6$ ($1.6 \leqslant z \leqslant 4.4$), respectively. For our $0.6 \leqslant z_{1548} < 1$ sample, the best-fit $\alpha_N = -1.39^{+0.24}_{-0.27}$ agreed better with Boksenberg et al. (2003) but was consistent with both studies at the 2σ level.

More detailed comparison with other studies of C IV absorbers at $z < 1$ are given in Appendix D.

6.2. $\Omega_{C^{+3}}$ Evolution

We have measured a statistically significant increase in $\Omega_{C^{+3}}$ at $z < 1$ compared to the roughly constant value observed at $1 < z < 5$. The error-weighted average of the $1 < z < 5$ measurements in Figure 13 is $\overline{\Omega}_{C^{+3}} = (2.2 \pm 0.2) \times 10^{-8}$ at $\overline{z} = 3.240$. Our integrated $\Omega_{C^{+3}} = (6.20^{+1.82}_{-1.52}) \times 10^{-8}$ at $\langle z \rangle = 0.654$ is a 2.8 ± 0.7 increase. We recognize the significance of the increase in $\Omega_{C^{+3}}$ at $z < 1$ because we have carefully adjusted the $1 < z < 5$ values of other authors (see Appendix C). Danforth & Shull (2008) stated that their $\Omega_{C^{+3}}$ value agreed with that of Scannapieco et al. (2006) without considering the effect of the column density limits. Frye et al. (2003) interpreted their $z < 0.1$ $\Omega_{C^{+3}}$ value as an increase but without comment on its significance.

To estimate the rate of evolution of the C^{+3} mass density, we adopt a simple linear model:

$$\Omega_{C^{+3}} = a_0 + a_1 t_{\mathrm{age}} \qquad (23)$$
$$\sigma^2_\Omega = \sigma^2_{a_0} + t^2_{\mathrm{age}}\sigma^2_{a_1} + 2t_{\mathrm{age}}\mathrm{COV}_{01},$$

where t_{age} is the age of the universe and COV_{01} is the covariance of the intercept a_0 and the slope a_1. The observed 1σ uncertainties in $\Omega_{C^{+3}}$ were used in the χ^2-minimization algorithm. The results of the linear regression for the $1 < z < 5$ ($1\,\mathrm{Gyr} \leqslant t_{\mathrm{age}} \leqslant 6\,\mathrm{Gyr}$) and $z < 5$ ($t_{\mathrm{age}} > 1\,\mathrm{Gyr}$) samples are shown in Figure 15. We included the following $\Omega_{C^{+3}}$ measurements, adjusted for cosmology and/or column density range

[17] We measure $\Delta z = 2.2$ for the E140M spectra.

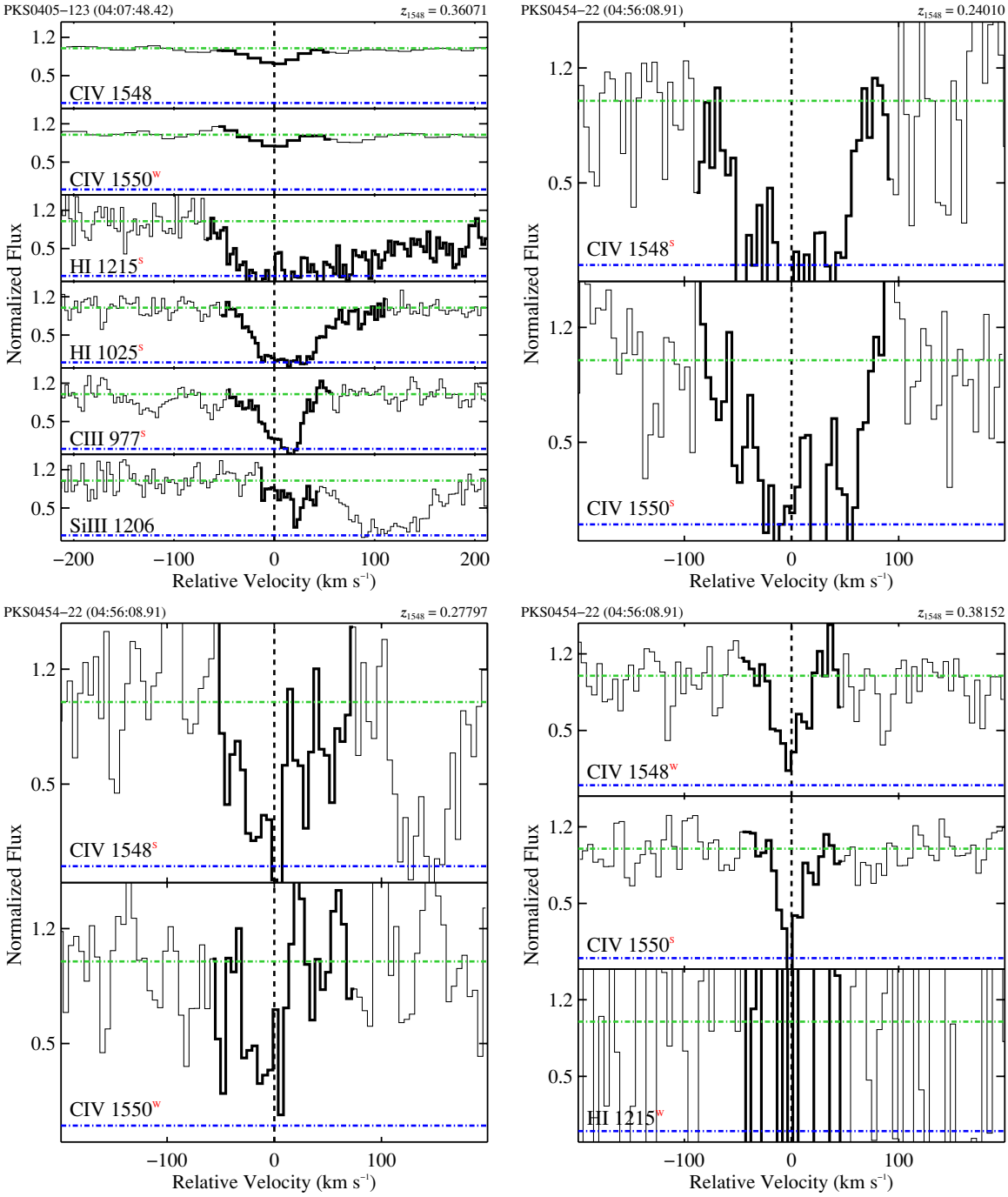

Figure 17. (Continued)

(see Appendix C): Songaila (2001, $1.5 < z < 4.5$);[18] Pettini et al. (2003, as revision of Songaila (2001) $z \approx 4.7$ value); Boksenberg et al. (2003); Scannapieco et al. (2006); and the current study.[19]

Whether or how $\Omega_{C^{+3}}$ evolves from $z = 5 \rightarrow 1$ is not statistically constrained, assuming the simple linear model. The best-fit slope for this range was $a_1 = (0.15 \pm 0.3) \times 10^{-8}$ Gyr^{-1} with the intercept $a_0 = (1.9 \pm 0.6) \times 10^{-8}$ (at $t_{age} = 0$ Gyr) and χ^2 probability $P_{\chi^2} = 34\%$.

The linear regression for the $z < 5$ data indicates a statistically significant trend in $\Omega_{C^{+3}}$ evolution. The fitted parameters are consistent with $\Omega_{C^{+3}}$ evolving slightly: $a_1 = (0.42 \pm 0.2) \times 10^{-8}$ Gyr^{-1} and intercept $a_0 = (1.33 \pm 0.5) \times 10^{-8}$ ($P_{\chi^2} = 36\%$). Several high-redshift studies (Songaila 2001; Pettini et al. 2003; Boksenberg et al. 2003) concluded that $\Omega_{C^{+3}}$ evolved very little to not at all for $z \approx 5 \rightarrow 1$, which is consistent with the previous linear regression of the $1 < z < 5$ data. Incorporating the new $z < 1$ measurements, there is evidence that $\Omega_{C^{+3}}$ has slowly but steadily increased since $z \approx 5$, at the 97% confidence level.

[18] The results from Pettini et al. (2003) are considered a revision to the $4.5 \leqslant z < 5$ bin since Pettini et al. (2003) used higher S/N data. The $5 \leqslant z < 5.5$ bin from Songaila (2001), which only included one detected absorber, was excluded.

[19] We excluded the Danforth & Shull (2008) measurement since our $z < 0.6$ measurement includes the E140M data.

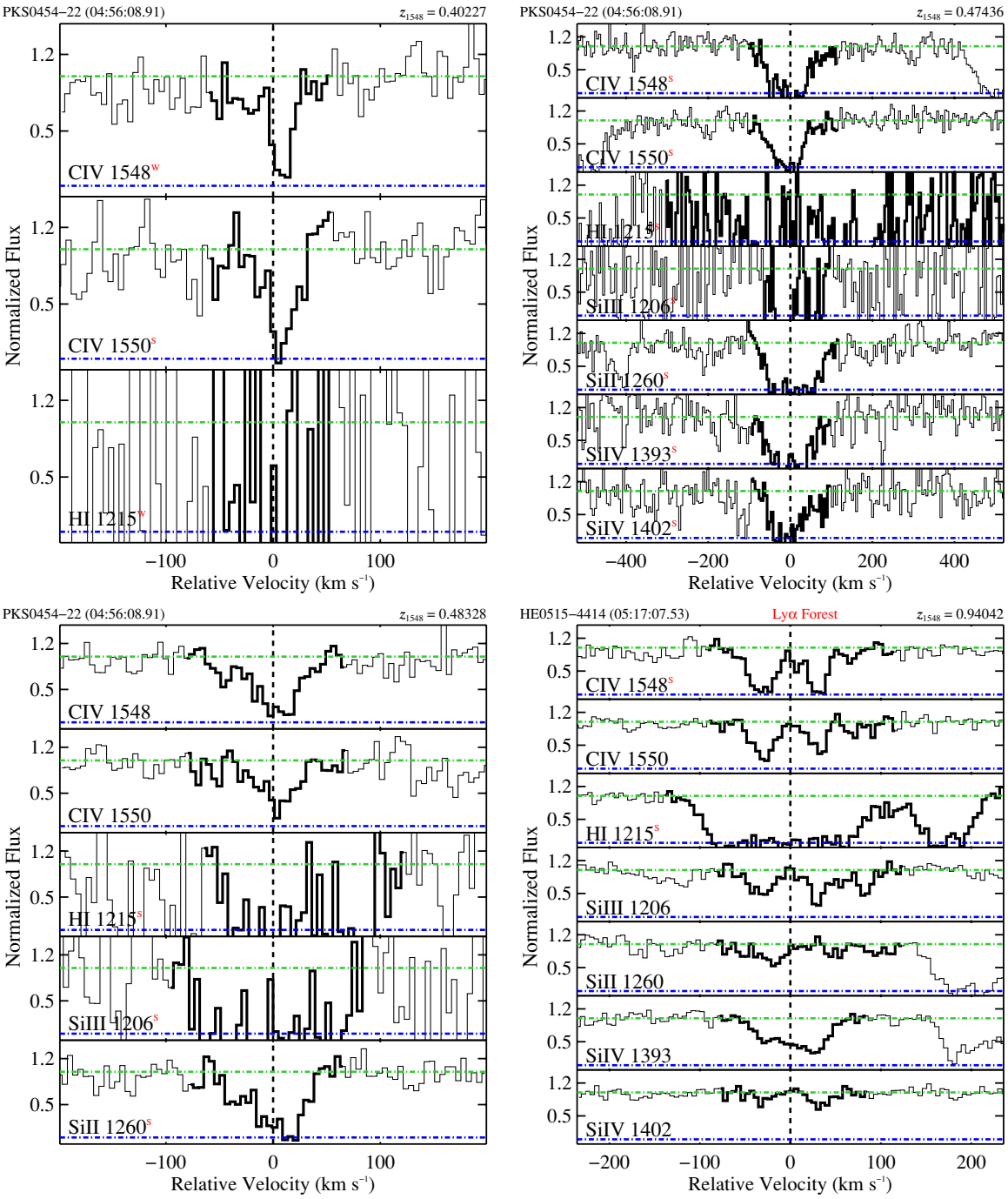

Figure 17. (Continued)

We acknowledge that our accounting for differences in cosmology and column density range were imperfect. However, whether or not we adjust for differences in the $N(C^{+3})$ range does not significantly affect the previous results: our $\Omega_{C^{+3}}$ value is still a statistically significant increase over $\overline{\Omega}_{C^{+3}}$, and the rate of evolution (a_1) from $z = 5 \rightarrow 0$ is also significant, assuming the simple linear model.

We emphasize that Equation (23) was *not* physically motivated. The temporal evolution of $\Omega_{C^{+3}}$ is influenced by multiple, complex physical processes (e.g., star formation, UV background). In addition, only C IV absorbers with $13 \leqslant \log N(C^{+3}) \leqslant 15$ are included in the measurements of $\Omega_{C^{+3}}$. However, as we discuss in Section 6.3, the physical nature of doublets in this column density range likely changes over the 12 Gyr from $z = 5 \rightarrow 0$. The linear regression analysis was simply a secondary way to gauge whether our observed $\Omega_{C^{+3}}$ values suggest a significant increase compared to the $z > 1$ values. In the context of this simple model, we rule out null evolution at high confidence.

6.3. Changing Nature of C IV Absorbers

In Section 6.1, we noted that $d\mathcal{N}_{C\,IV}/dX$ for $\log N(C^{+3}) \geqslant 13$ has not evolved with redshift (see Figure 14). However, there is evidence for evolution of $d\mathcal{N}_{C\,IV}/dX$ when only the strong systems ($W_{r,1548} \geqslant 150$ mÅ and $\log N(C^{+3}) \gtrsim 13.7$) are included (Steidel 1990; Misawa et al. 2002; Boksenberg et al.

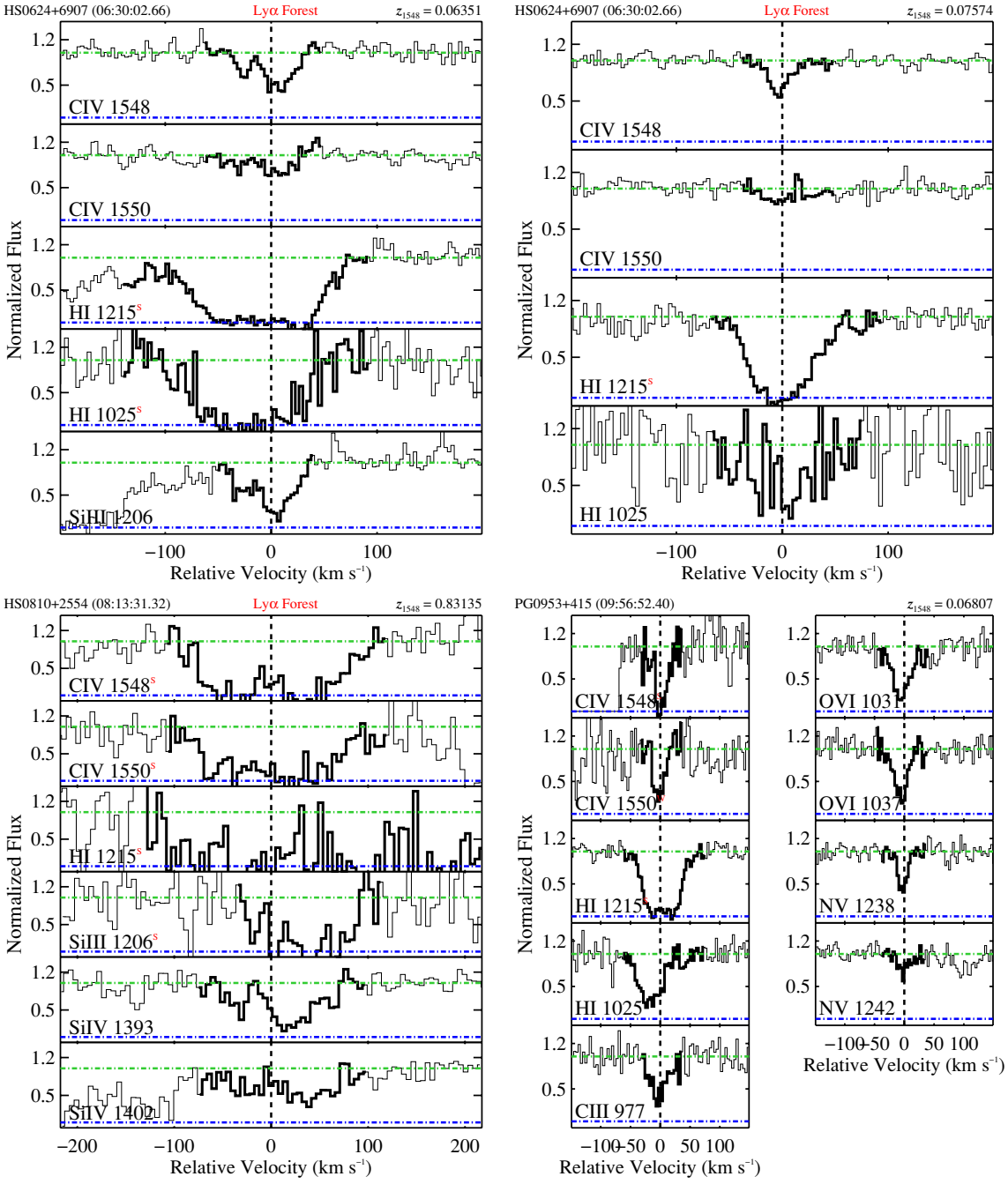

Figure 17. (Continued)

2003). The weak systems dominate the number counts, resulting in no evolution of $d\mathcal{N}_{\rm C\,IV}/dX$ for the full sample. Since the stronger doublets dominate the C^{+3} mass density, we observe the increased number of strong C IV doublets in the significant increase of $\Omega_{C^{+3}}$ at $z < 1$.

Even without limiting redshift-evolution analysis to the strongest absorbers, Boksenberg et al. (2003) noted that complex C IV systems have higher mean column densities at lower redshift, where "complex" indicates that the number of Voigt profile components is $\geqslant$7. Misawa et al. (2002) predicted this result by tying their observed increase of high-W_r doublets at low redshift with Petitjean & Bergeron (1994) observations that higher W_r systems have more components. From visual inspection of the $W_{r,1548} \geqslant 150$ mÅ doublets, we see that more than half have multiple, prominent components.

Perhaps the trend to higher column density, more multi-component C IV absorbers at low redshift supports the claim that ≈50% of $\log N(C^{+3}) > 13.3$ doublets are associated with galactic outflows (Songaila 2006). Alternatively, the strong absorbers might trace infall or high-velocity cloud-like halo gas. In either case, the complex profiles might be a result of the heterogeneous nature of outflowing or infalling gas. Observations at low-redshift have indicated that C IV absorption often reside in galaxy halos, on ≈100 kpc scales (Chen et al. 2001).

What C IV absorption traces at all redshifts affects the interpretation of the evolution of $\Omega_{C^{+3}}$. In Section 6.2, we discussed

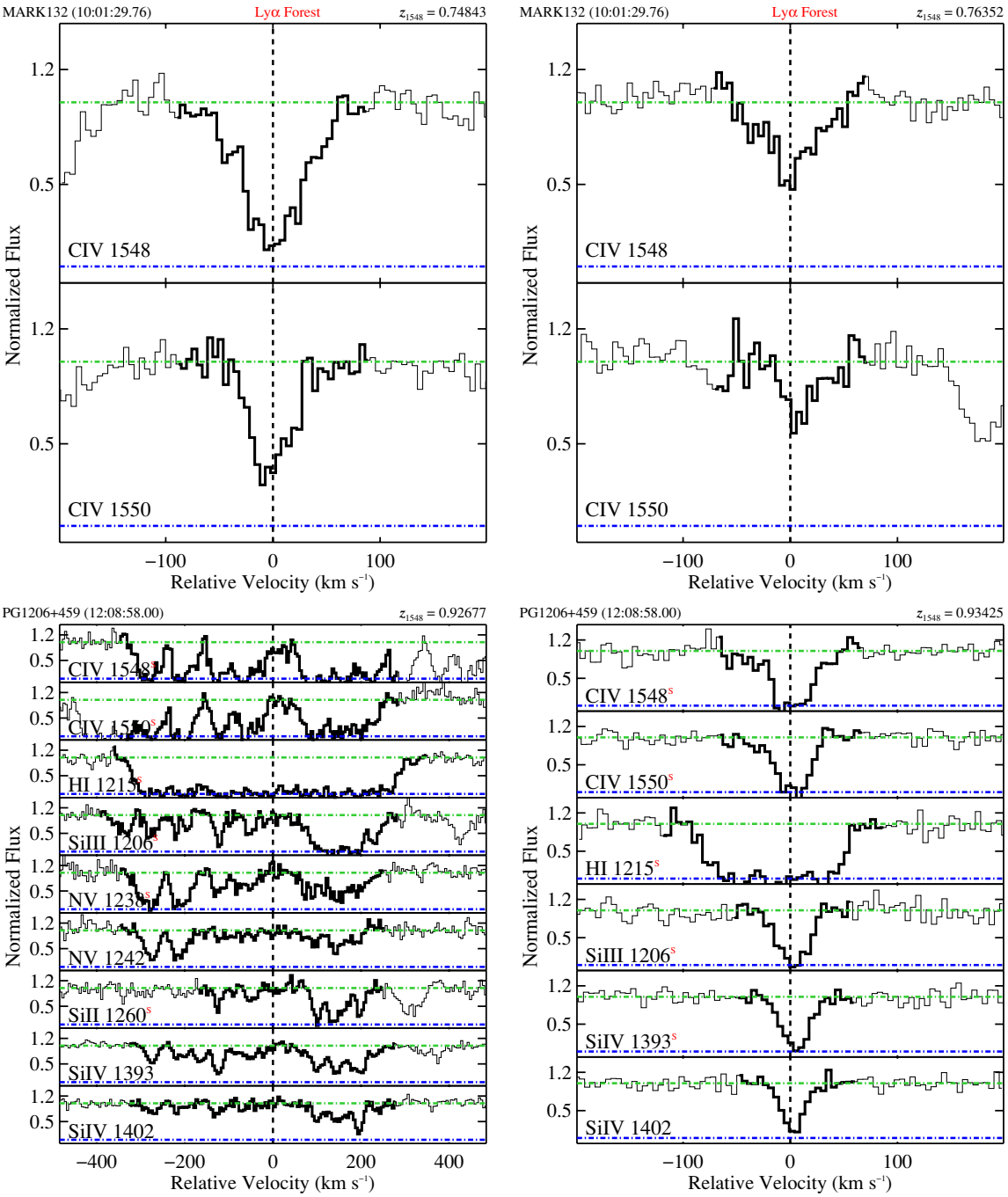

Figure 17. (Continued)

the time evolution of $\Omega_{C^{+3}}$ for $13 \leqslant \log N(C^{+3}) \leqslant 15$ doublets at $z < 5$, and we showed that there has been a significant increase at $z < 1$ and that null evolution is ruled out. However, if the majority of $13 \leqslant \log N(C^{+3}) \leqslant 15$ C IV doublets are (low-density) intergalactic at $z > 1$ while the majority are circumgalactic at $z < 1$, then the $\Omega_{C^{+3}}$ observations at high and low redshift are not directly comparable. In a future paper, we will explore the changing nature of C IV doublets by comparing the properties and environments of C IV absorption in cosmological hydrodynamic simulations[20] with observations (also see Cooksey 2009).

[20] The simulations are from the OverWhelmingly Large Simulations project (Schaye et al. 2009).

6.4. Sightline Selection Bias

Several sightlines in our sample were originally observed for reasons that increase the likelihood that C IV absorption would be detected. For example, there were quasars targeted because intergalactic Mg II absorption was observed in optical spectra. Studies have shown that Mg II absorbers frequently exhibit C IV absorption (Churchill et al. 1999a). Including such sightlines in our survey might have increased our detected doublets and biased our results to have more C IV doublets than would be observed in an *un*biased survey of the IGM. On the other hand, the sensitivity limits of high-resolution spectrometers on *HST* (prior to the installation of the Cosmic Origins Spectrograph)

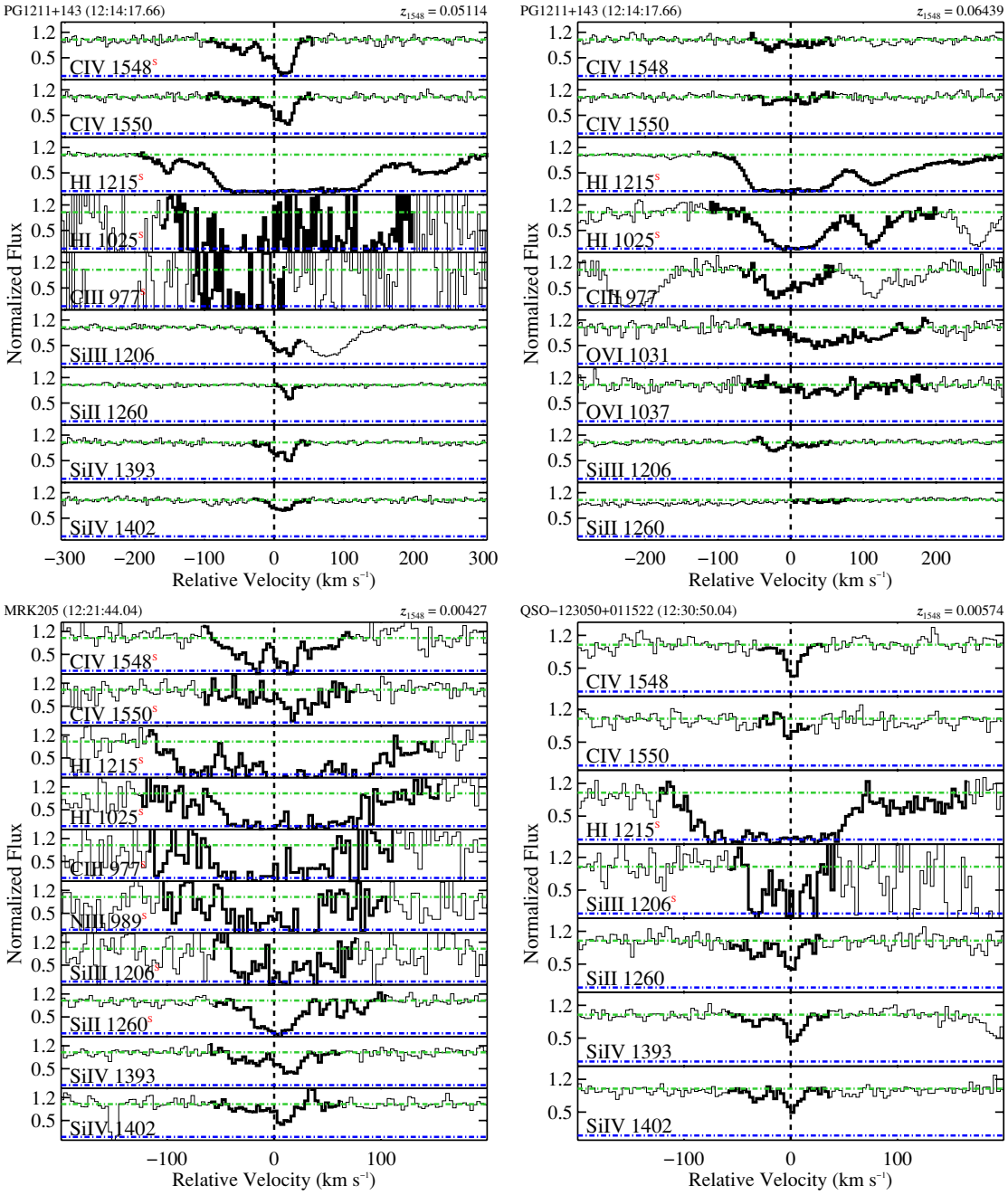

Figure 17. (Continued)

imply only a small number of quasars could have been observed, independent of known absorbers.

To explore the bias in our survey due to the sightline selection criteria, we compared our C IV absorber line density $d\mathcal{N}_{\rm C\,IV}/dz$ with Barlow & Tytler (1998), who performed a survey for strong C IV absorbers in 15 sightlines from the *HST* Faint Object Spectrograph (FOS) archives at the redshifts of known Lyα absorbers. The FOS quasar key line project targeted bright quasars, without prior knowledge of, e.g., Mg II, damped Lyα, or Lyman limit systems (Bahcall et al. 1993). Barlow & Tytler (1998) measured $d\mathcal{N}_{\rm C\,IV}/dz = 2.3 \pm 0.9$ for $W_r > 400$ mÅ and $0.2 < z_{1548} < 0.8$ (six doublets).

We detected six G = 1 C IV doublets that met the Barlow & Tytler (1998) criteria and find for this subsample, $d\mathcal{N}_{\rm C\,IV}/dz = 1.3^{+0.8}_{-0.5}$. Thus, our measured absorber line density agreed with the unbiased result within 1σ. Despite including sightlines observed with prior knowledge about the IGM, we agreed with an unbiased survey and, in fact, record a smaller incidence of strong C IV absorbers.

As a second check for sightline bias, we reanalyzed our survey after excluding 11 G = 1 C IV doublets that were possibly associated with targeted Mg II absorbers, DLAs, or LLS (see Table 10).[21] For this subsample, $d\mathcal{N}_{\rm C\,IV}/dz = 0.4^{+0.6}_{-0.3}$ for the two G = 1 C IV doublets with $W_r > 400$ mÅ and $0.2 < z_{1548} <$

[21] Several sightlines were targeted for a specific absorption system but the archival spectra did not cover the C IV doublet. The following are the sightlines and bias: PKS0454–22, Mg II at $z_{\rm abs} = 0.6248$ and 0.9315 (Churchill & Le Brun 1998); HE0515–4414, DLA at $z_{\rm abs} = 1.15$; MARK132, LLS at $z_{\rm abs} = 1.7306$; and PKS1127–145, DLA at $z_{\rm abs} = 0.312$. The PG1634+706 sightline was also targeted for a D/H study and Mg II absorber at $z_{\rm abs} = 0.9902$, but we did not include that echelle order in our co-added spectra.

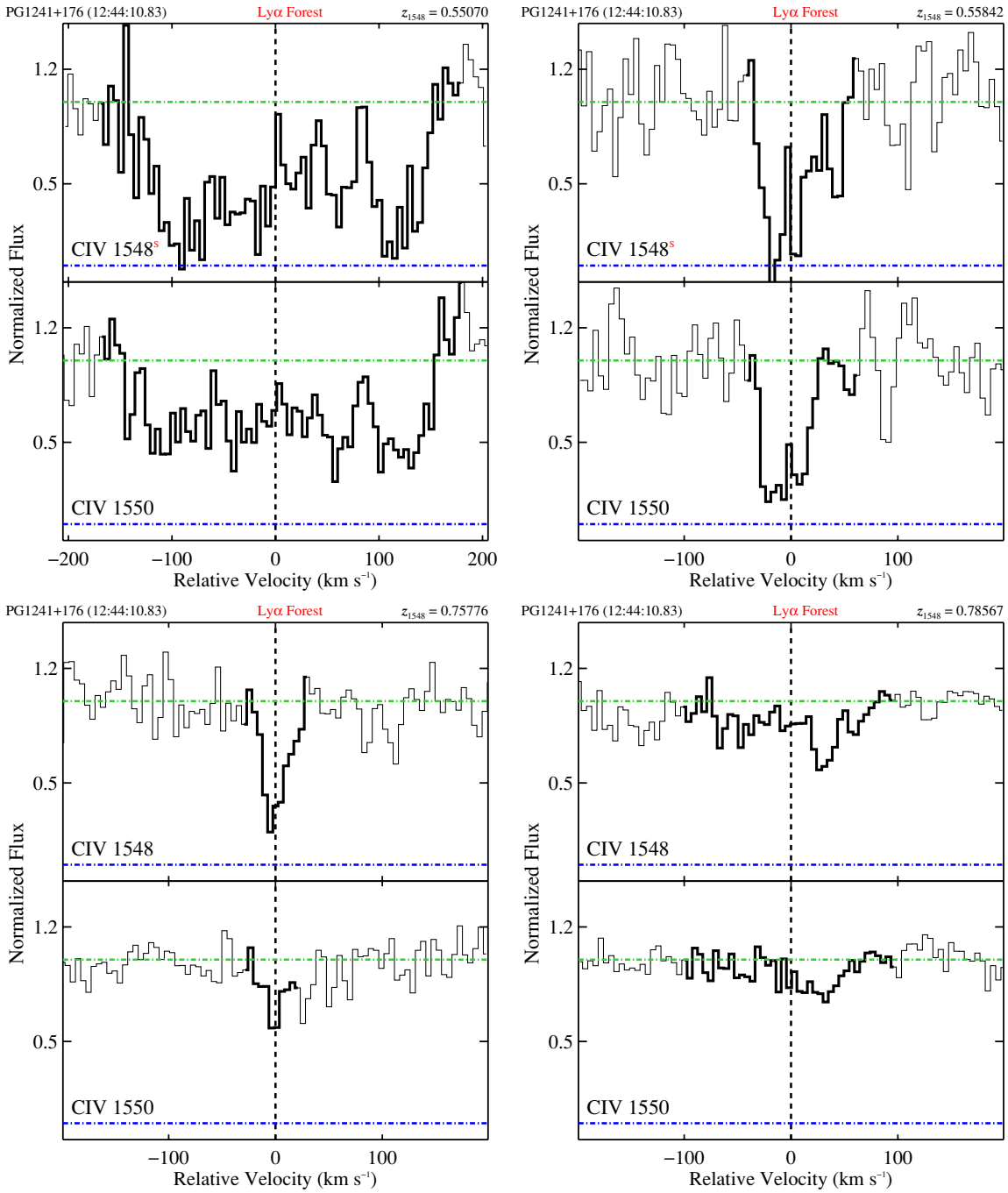

Figure 17. (Continued)

0.8, which underestimates the Barlow & Tytler (1998) results by 1.8σ. The best-fit coefficient and exponent from the maximum likelihood analysis of $f(W_{r,1548})$ were $k_3 = 1.40^{+0.67}_{-0.51}$ mÅ^{-1} and $\alpha_W = -1.51^{+0.39}_{-0.41}$, which lie within 0.5σ of the values in Table 7. For $f(N(C^{+3}))$, the best-fit values were $k_{14} = 0.49^{+0.16}_{-0.13}$ cm^2 and $\alpha_N = -1.71^{+0.22}_{-0.26}$, which were within 1σ of the values in Table 6, respectively. The change in coefficient and exponent change the integrated $\Omega_{C^{+3}} = (3.96^{+1.46}_{-1.15}) \times 10^{-8}$, lower than that from the full sample but a 1.8 ± 0.5 increase over the error-weighted average of the $1 < z < 5$ measurements.

Excluding the 11 C IV doublets possibly associated with known absorption features yields an integrated $\Omega_{C^{+3}}$ within 3σ of the value extrapolated from the model to $1 < z < 5$ (see top panel, Figure 15). However, by excluding the 11 absorbers, most with $\log N(C^{+3}) > 14$, we undersampled the strong doublets as expected from the Barlow & Tytler (1998) study, and the high-$N(C^{+3})$ systems dominate the C^{+3} mass density. In the attempt to eliminate the effects of the sightline selection bias, we introduced a possible bias against strong C IV doublets. We have proceeded, therefore, with the full sample of archival spectra.

6.5. C IV Doublets without Lyα Absorption

We conducted a blind survey for C IV doublets, relying initially on the characteristic wavelength separation of the

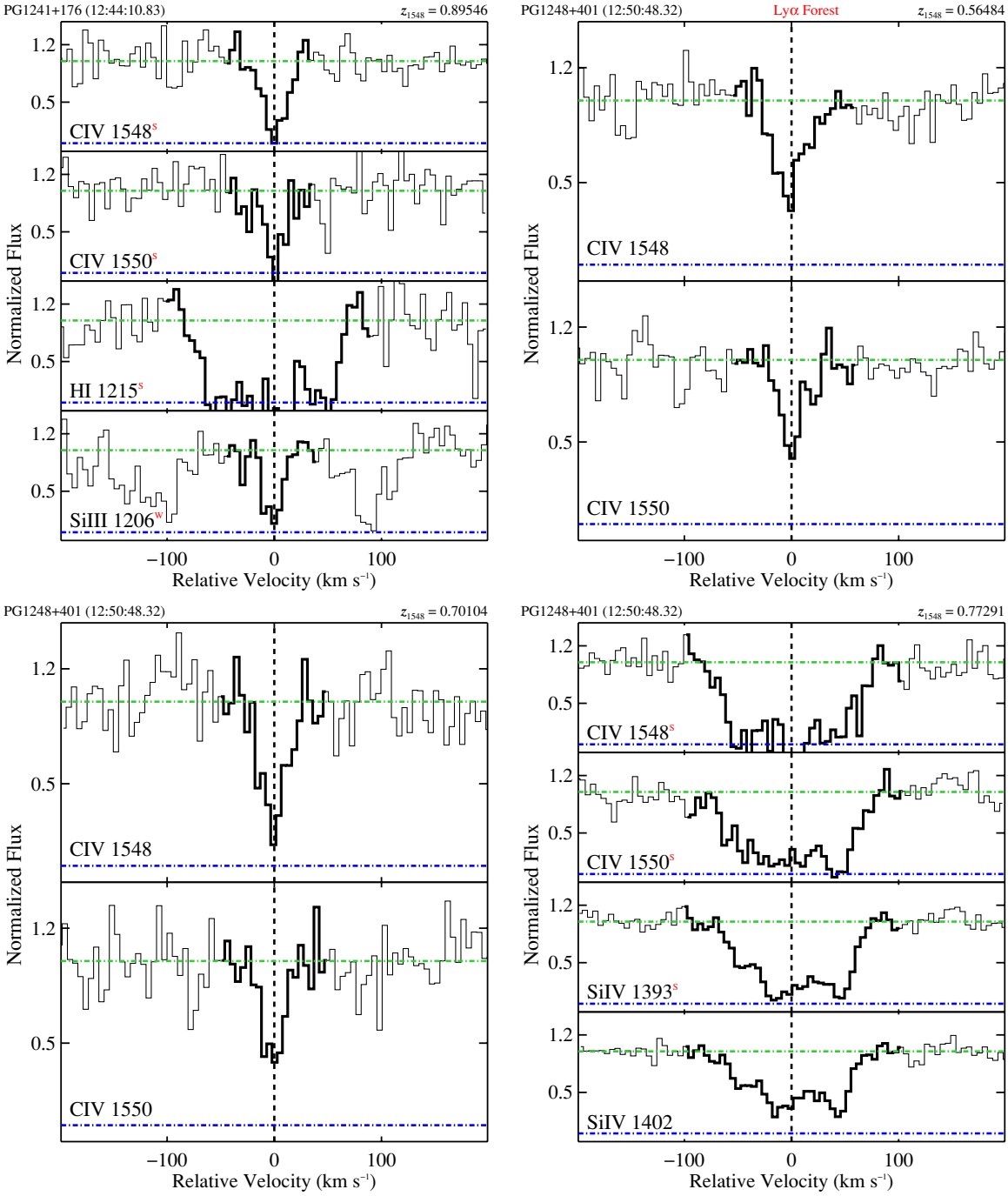

Figure 17. (Continued)

doublet. From the resulting list of candidates, we drew on other known characteristics of C IV doublets to distinguish the final sample (see Section 3 and Table 3). Although the detection of associated Lyα absorption was a diagnostic and based on previous observations (Ellison et al. 1999; Simcoe et al. 2004), it was not required. C IV doublets without Lyα absorption have been observed at $z > 1$ (Schaye et al. 2007). Here we discuss the likelihood that some C IV doublets in our sample were actually due to Lyα forest contamination (see Section 4.3) and if we indeed detect any "naked" C IV absorption.

Our sample includes two G = 2 C IV doublets without Lyα absorption detected ($N_{\rm H\,I} \leqslant 10^{13.4}$ cm^{-2}) that were in the Lyα forest: $z_{1548} = 0.83662$, $\log N(C^{+3}) = 14.2$ doublet toward HS0747+4259 and $z_{1548} = 0.87687$, $\log N(C^{+3}) \approx 14$ doublet in toward HS0810+2554. In the scatter plot of $N(C^{+3})$ versus $N_{\rm H\,I}$, the HS0747+4259 system has the highest C^{+3} column density for any $\log N_{\rm H\,I} < 14$ system (see Figure 16). The HS0810+2554 system does not have a useful constraint on $N_{\rm H\,I}$ (see Table 5) and could not be plotted. Though these two systems could be high-metallicity systems akin to those in Schaye et al. (2007), it is more likely that their atypical column densities are due to their low S/Ns, which increases the uncertainties in continuum fitting and column densities. The HS0747+4259 and HS0810+2554 E230M spectra have S/N = 6 pixel^{-1} and 3 pixel^{-1}, respectively (see Table 1).

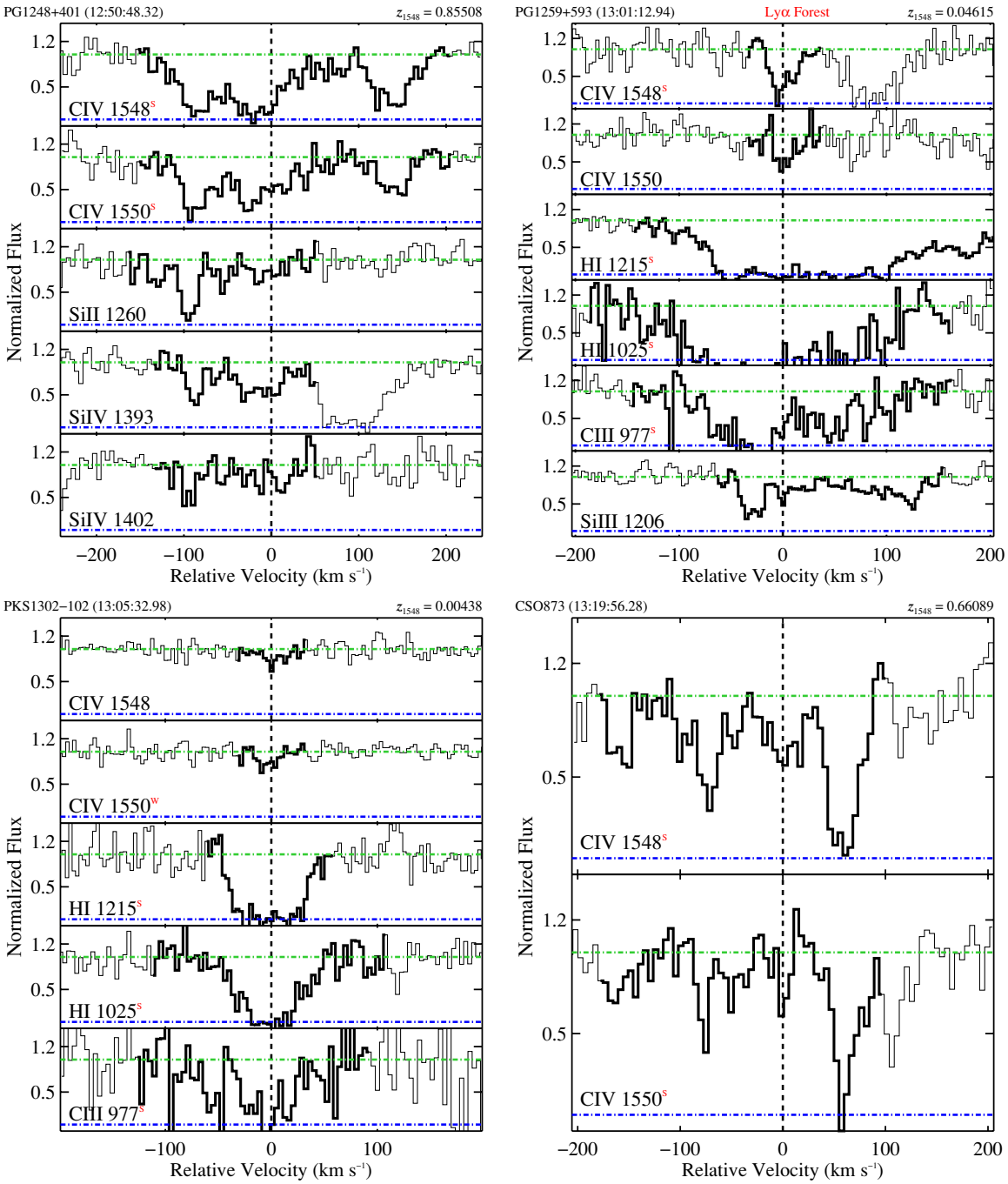

Figure 17. (Continued)

The low S/N also increases the likelihood that Lyα forest lines will be (incorrectly) identified as C IV doublets (see Section 4.3). In the most extreme scenario, the maximum absorption path length in the Lyα forest is $\Delta X = 8.9$ for the strongest Monte Carlo absorbers ($\log N(C^{+3}) \geqslant 14.1$ or $W_{r,1548} \geqslant 157$ mÅ). The estimated rate of Lyα forest lines masquerading as C IV doublets was $d\mathcal{N}/dX \leqslant 0.11$ for $0.8 \leqslant z \leqslant 1.5$ (see Figure 8). Therefore, the maximum expected number of C IV-like Lyα pairs would be 1^{+2}_{-1}, which is consistent with Lyα forest lines coinciding to be the two G = 2 doublets in question.

Next, we evaluate how many of the 25 G = 1+2 C IV doublets detected in the Lyα forest might be false-positive identifications. Two were discussed previously. There were 19 from the "definitely C IV" (G = 1) sample. In 15 of the forest doublets, the detection of other associated transitions[22] and/or multi-component profiles[23] lent credibility to the identification as C IV absorption.

There were eight doublets in the Lyα forest that had no associated transitions, no Lyα coverage, and nondescript profiles.[24]

[22] The G = 1 $z_{1548} = 0.81814$ system toward PG1634+706 is an example of a C IV doublet with associated transitions such as Lyα and the Si IV doublet.
[23] For example, the G = 1 $z_{1548} = 0.57632$ doublet toward PG0117+213 clearly has a multi-component profile, with C IV absorption correlated for almost 200 km s^{-1}.
[24] The G = 1 $z_{1548} = 0.74843$ doublet toward MARK132 has a nondescript profile.

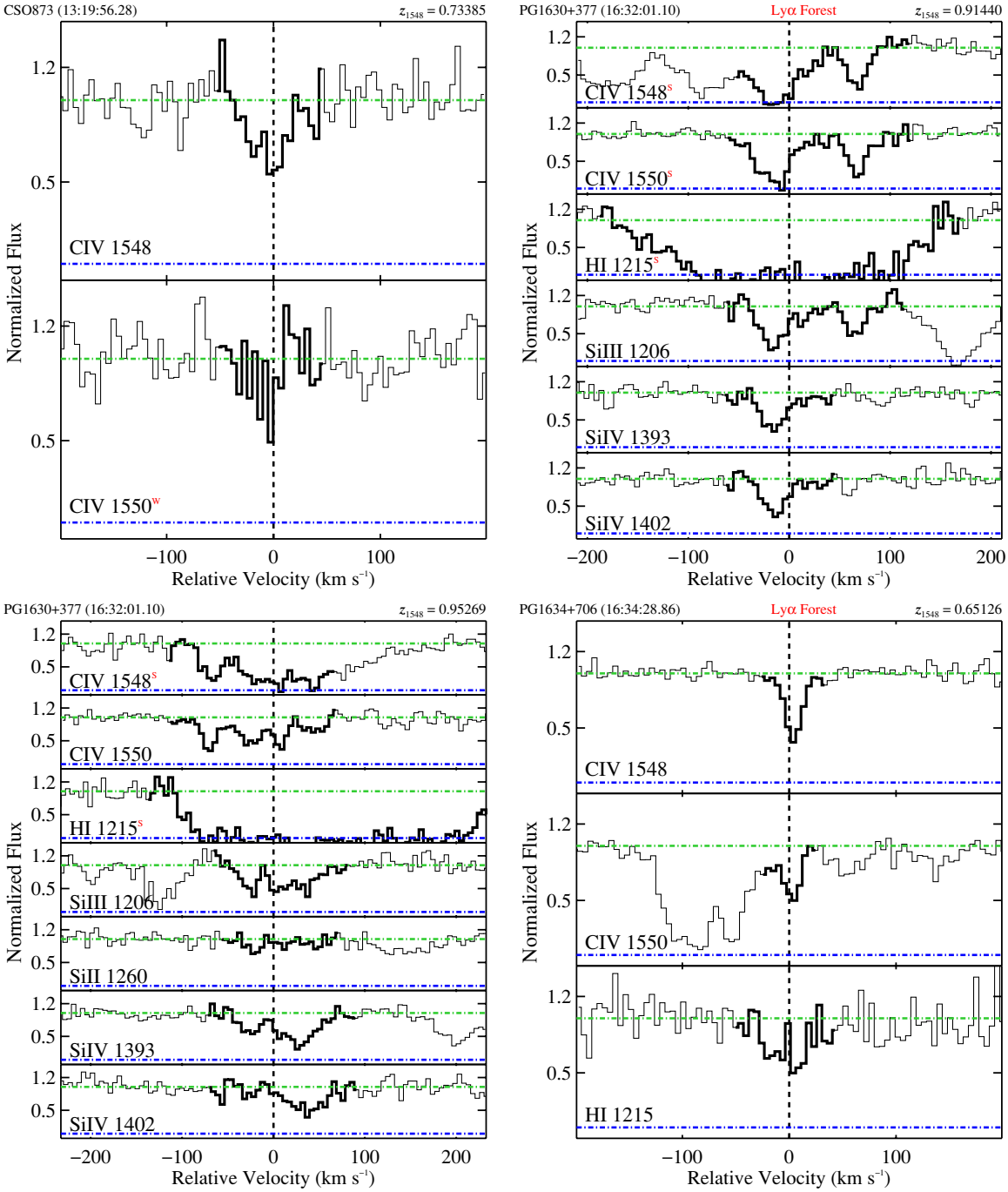

Figure 17. (Continued)

Therefore, there were fewer diagnostics available for evaluating the doublet identification. We include these doublets in our sample because we estimate the Lyα contamination with Monte Carlo simulations (Section 4.3). There is a total of 10 systems in the Lyα forest that satisfy few of the C IV characteristics (see Table 3): the eight doublets with nondescript profiles and the two that lack significant Lyα absorption, discussed previously. The simulations of the Lyα forest contamination rate excludes all 10 from being Lyα forest contamination at the 99.9% confidence level.

Ultimately, there were no definite detections of C IV doublets without associated Lyα absorption.

7. SUMMARY

We conducted the largest survey for $z_{1548} < 1$ C IV absorbers to date. We surveyed 49 sightlines with the *HST* STIS and/or GHRS archival spectra with moderate S/N and resolution. All absorption-line features and actual absorption lines were identified by an automated feature-finding algorithm. From this list, candidate C IV systems were assembled, based solely on the doublet's characteristic wavelength separation (see Table 2).

We visually inspected all candidates with rest equivalent widths $W_{r,1548} \geqslant 3\sigma_{W_r,1548}$. After considering the various diagnostics (e.g., profile; see Table 3), we identified 44 definite

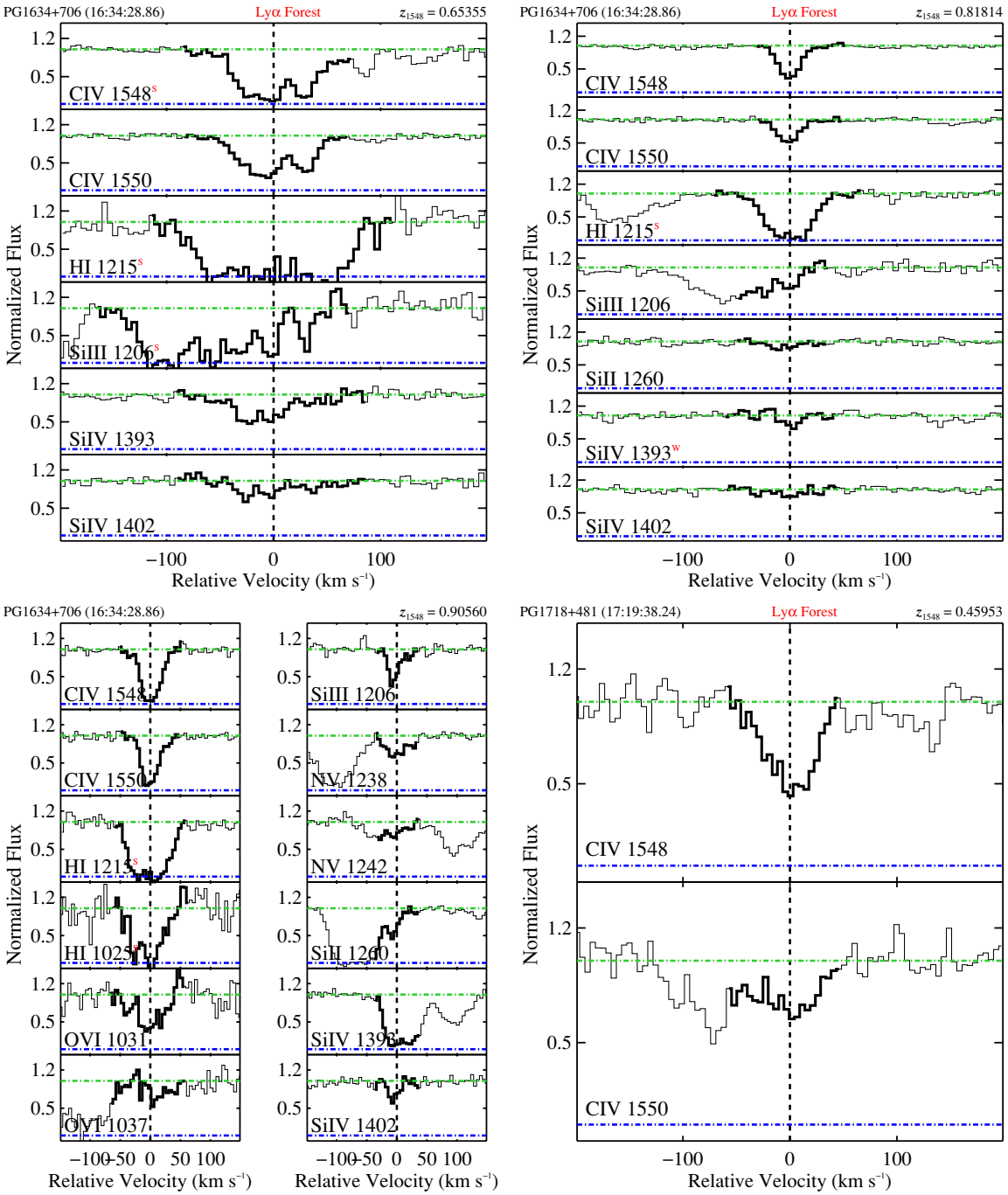

Figure 17. (Continued)

(G = 1) and 19 likely (G = 2) C IV systems. Of these, we only analyzed the 38 G = 1 and five G = 2 doublets where both lines were detected with $W_r \geqslant 3\sigma_{W_r}$. All subsequent analyses considered the full sample and two redshift bins, divided at, approximately, the median redshift: $z_{1548} < 0.6$ (20 G = 1+2 doublets) and $0.6 \leqslant z_{1548} < 1$ (23).

From synthetic spectra, we estimated the unblocked, comoving path length ΔX to which our survey was 95% complete as a function of $N(C^{+3})$ and $W_{r,1548}$ (see Figure 7). For the strongest absorbers ($\log N(C^{+3}) \geqslant 14.1$ and $W_{r,1548} \geqslant 157$ mÅ), $\Delta X = 15.1$.

There were 10 G = 1+2 doublets detected in the Lyα forest that had nondescript profiles, no associated metal lines, and either no Lyα absorption or Lyα coverage did not exist. We estimated the contamination rate that Lyα forest lines would be mistaken for C IV doublets, with Monte Carlo simulations. The rate is small: $dN/dX \leqslant 0.11$. Therefore, it was ruled out at the 99.9% confidence level that all of the 10 doublets were Lyα-as-C IV pairs. However, the two G = 2 doublets without Lyα absorption ($W_{r,\mathrm{Ly}\alpha} < 3\sigma_{W_r}$) were consistent with being Lyα forest lines masquerading as C IV doublets.

With a maximum likelihood analysis, we modeled the column density frequency distribution with a power law: $f(N(C^{+3})) = k_{14}(N_{C^{+3}}/N_0)^{\alpha_N}$. The best-fit exponent was $\alpha_N = -1.75^{+0.28}_{-0.33}$ for the $z_{1548} < 0.6$ sample. For the $0.6 \leqslant z_{1548} < 1$ sample, the best-fit value was $\alpha_N = -1.39^{+0.24}_{-0.27}$. There has been no consensus on the power-law exponent in the various $z_{1548} > 1.5$

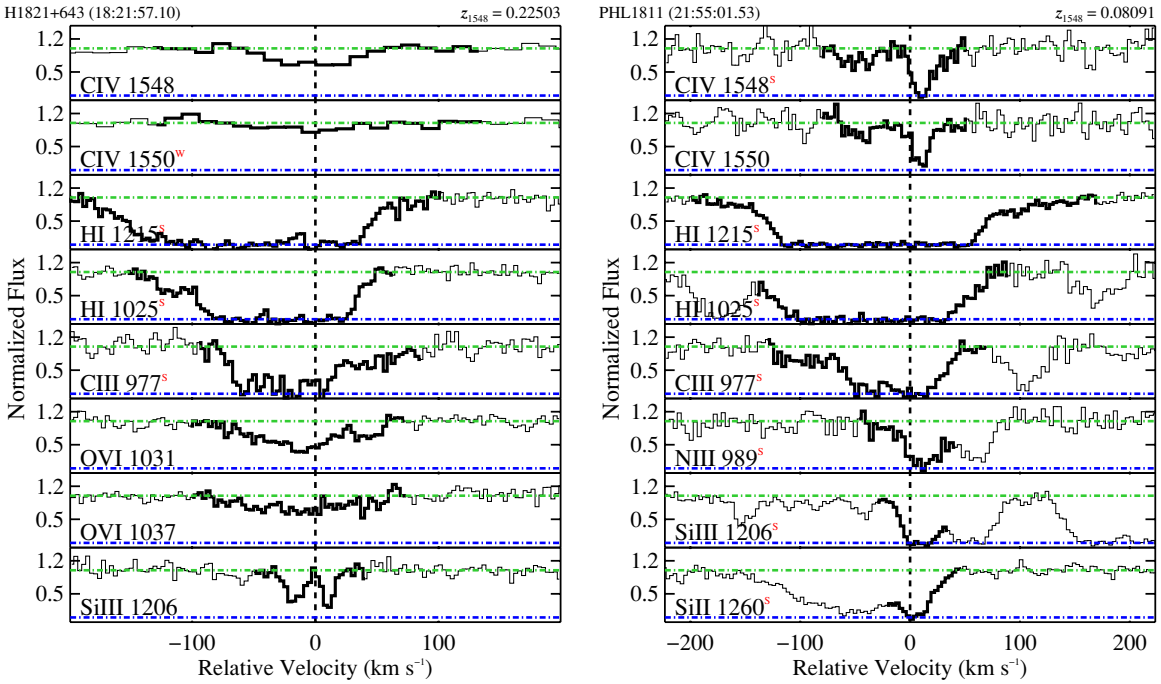

Figure 17. (Continued)

Table 10
Sightline Selection Bias

Target	z_{abs}	$\lvert\delta v_{excl}\rvert$ (km s^{-1})	Bias	$\mathcal{N}_{excl}$	δv_{abs} (km s^{-1})	log $N(C^{+3})$
PG0117+213	0.5763[a]	600	Mg II	1	3	14.52 ± 0.03
	0.72907[b]	600	Mg II	0	...	...
PG1206+459	0.93[c]	1500	Mg II	2	−503	>15.39
					661	14.25 ± 0.09
PG1211+143	0.051	400	D/H	1	39	14.01 ± 0.03
	0.0652	400	D/H	1	−228	13.28 ± 0.05
PG1241+176	0.5504	400	Mg II	1	57	14.60 ± 0.05
	0.5584	400	Mg II	1	3	14.26 ± 0.10
	0.8954	400	Mg II	1	9	<13.81
PG1248+401	0.7729	400	Mg II	1	2	14.66 ± 0.06
	0.8545	400	Mg II	1	94	14.61 ± 0.04
PKS1302–102	0.0940	400	D/H	0	...	...
CSO873	0.66	400	Mg II	1	162	14.27 ± 0.02
PG1634+706	0.701	400	D/H, LLS	0	...	...

Notes. Sightlines targeted for specific absorption systems. We quote the target absorption system redshift z_{abs} from the proposal unless noted otherwise. By default, we excluded absorbers with $|\delta v_{abs}| \leqslant 400$ km s^{-1}, the clustering scale measured by Churchill & Vogt (2001). The exceptions are taken from the literature.

[a] Churchill et al. (2000).

[b] Churchill et al. (1999b).

[c] $z_{abs} = 0.9254$, 0.9276, and 0.9342.

surveys (Ellison et al. 2000; Songaila 2001, 2005; Boksenberg et al. 2003).

We measured the C IV absorber line density to be $d\mathcal{N}_{CIV}/dX = 4.1^{+0.7}_{-0.6}$ for log $N(C^{+3}) \geqslant 13.2$ and $W_{r,1548} \geqslant 52$ mÅ from the full G = 1+2 sample. $d\mathcal{N}_{CIV}/dX$ has not evolved significantly since $z = 5$ (see Figure 14).

The sightlines analyzed in the current study were observed for a variety of reasons, e.g., the targets were UV bright or a known damped Lyα system (DLA) lay along the sightline. The latter reason, and similar ones, might have introduced a bias into our survey, since sightlines with DLAs, Lyman-limit systems, and Mg II absorbers typically correlate with C IV doublets. Assuming that Barlow & Tytler (1998) provide an unbiased survey for C IV absorbers, we first compared our measured redshift densities for $0.2 < z_{1548} < 0.8$ and $W_r > 400$ mÅ. We agreed within 1σ and actually measured a lower incidence of strong absorbers.

We also excluded the 11 doublets close to the redshift of the targeted systems (see Table 10), then re-measured the absorber line density and re-fit the frequency distributions. The "unbiased" absorber line density agreed less well with Barlow & Tytler (1998; 1.7σ). The best-fit $f(N(C^{+3}))$ exponent and coefficient differed by $<1\sigma$, respectively, compared to the values for the full sample. Categorically excluding the C IV doublets possibly associated with, e.g., Mg II absorbers biased

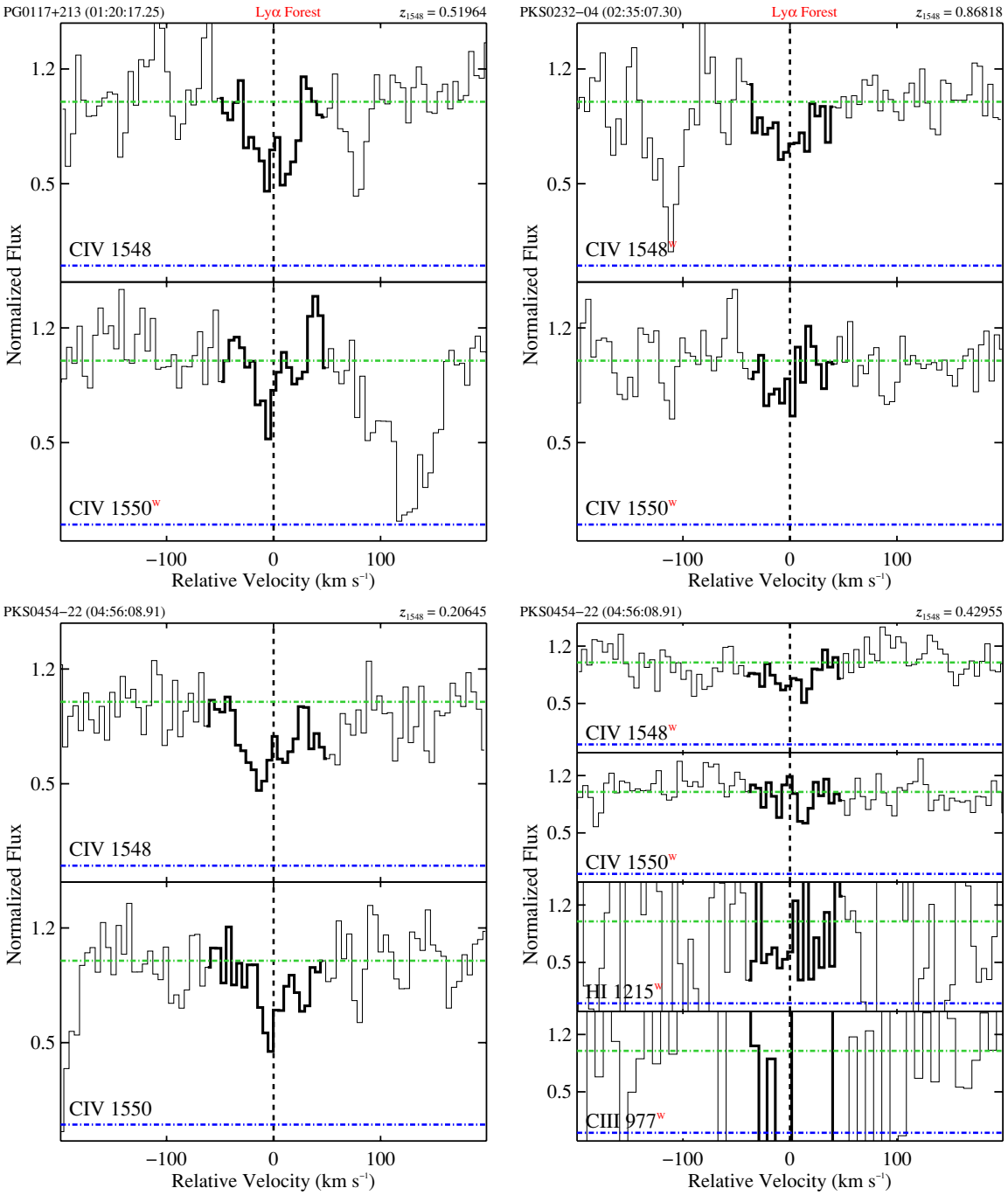

Figure 18. Velocity plots of G = 2 C IV systems. (See Figure 17 for description of velocity plot.) G = 2 velocity plots (continued)
(A color version of this figure is available in the online journal.)

our survey against strong log $N(C^{+3}) > 14$ doublets. Therefore, we concluded that the results for the full C IV sample represented the results of a truly unbiased survey, akin to Barlow & Tytler (1998).

Measuring the C^{+3} mass density relative to the critical density at $z_{1548} < 1$ was a principle aim of this study. High-redshift studies have agreed that $\Omega_{C^{+3}}$ changed little or not at all from $z = 5 \rightarrow 1$, once cosmology was properly taken into account (Songaila 2001, 2005; Boksenberg et al. 2003; Schaye et al. 2003; Pettini et al. 2003; Scannapieco et al. 2006). For the full G = 1 sample with $\langle z \rangle = 0.654$ ($t_{age} = 7.5$ Gyr), the integrated $\Omega_{C^{+3}} = (6.20^{+1.82}_{-1.52}) \times 10^{-8}$ for $13 \leqslant \log N(C^{+3}) \leqslant 15$. This was a 2.8 ± 0.7 increase over the $1 < z < 5$ values.

We assumed a simple linear model for the temporal evolution of $\Omega_{C^{+3}}$ in order to estimate the rate of change in the mass density. The linear regression for the $z < 5$ data indicated a slowly increasing $\Omega_{C^{+3}}$ with increasing age of the universe, at the $>3\sigma$ level: $d\Omega_{C^{+3}}/dt_{age} = (0.42 + 0.2) \times 10^{-8}\,\mathrm{Gyr}^{-1}$. This result relied on the measurements at $z < 1$; without which, the slope was unconstrained ($d\Omega_{C^{+3}}/dt_{age} = (0.15+0.3) \times 10^{-8}\,\mathrm{Gyr}^{-1}$).

Intuitively, it might not appear surprising that $\Omega_{C^{+3}}$ continually increases from $z = 5 \rightarrow 0$, since the overall metallicity of the universe increases. However, increasing metallicity would not translate directly to increasing C^{+3} mass density. The C IV mass density is also subject to the changing ionizing background

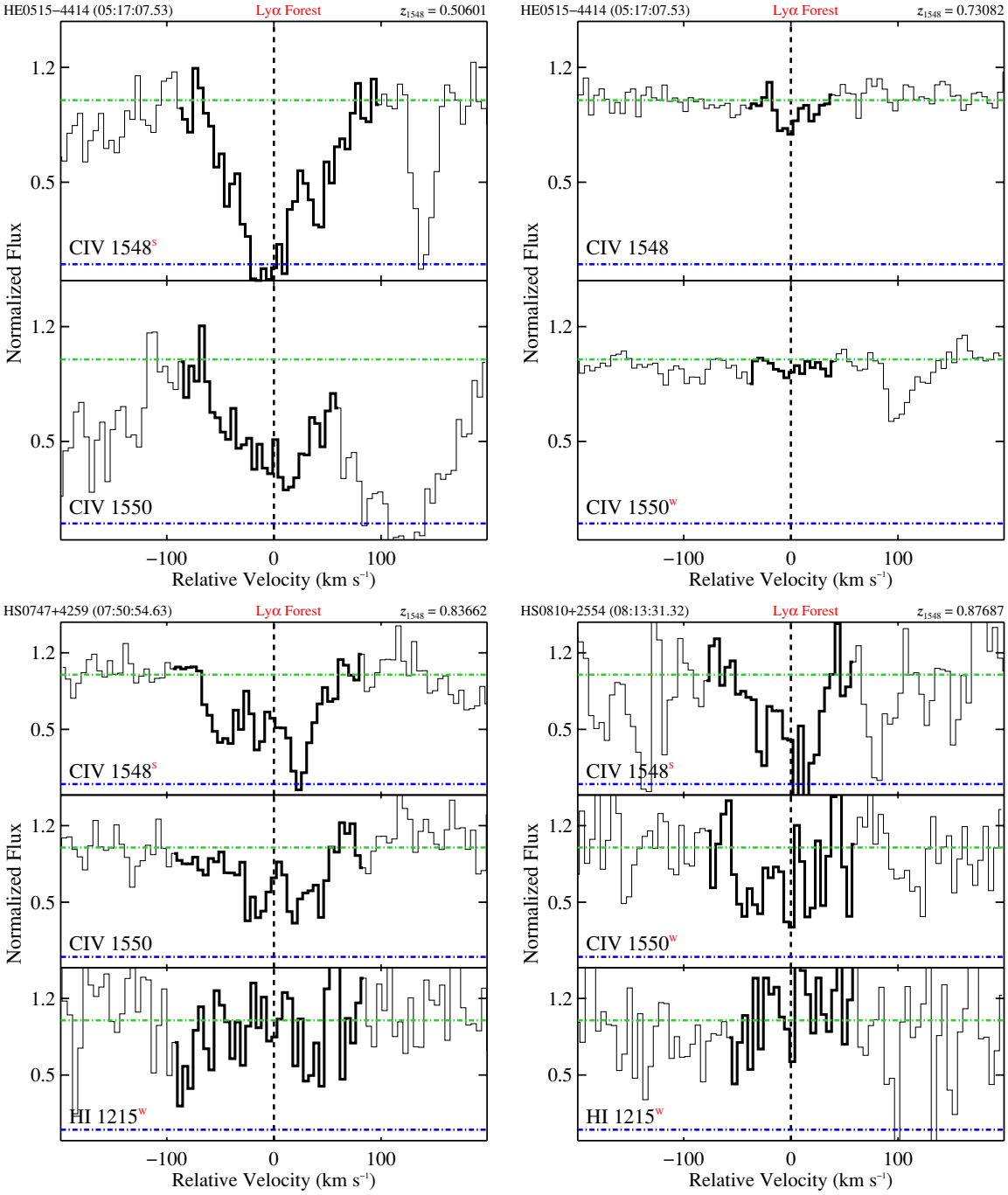

Figure 18. (Continued)

in the universe, which favors the C IV transition *less* at low redshift (see, e.g., Madau & Haardt 2009). Oppenheimer & Davé (2008) concluded that metallicity and ionizing background balanced one another from $z \approx 5 \rightarrow 1$, resulting in a nearly constant $\Omega_{C^{+3}}$.

We emphasized that the simple linear model for $\Omega_{C^{+3}}$ over t_{age} was not physically motivated. The *observed* C^{+3} mass density only accounted for doublets with $13 \leqslant \log N(C^{+3}) \leqslant 15$, and absorbers in this range likely arise in different physical environments at high and low redshifts. We discussed the changing nature of what C IV absorption traces; perhaps it probed the low-density IGM at $z > 1$ and galaxy halos at $z < 1$. We will explore, in a future paper, the physical conditions and environments of C IV absorbers in cosmological simulations with various feedback prescriptions.

We thank P. Jonsson for programming advice on the Monte Carlo simulations and the maximum likelihood analysis. We also thank B. Oppenheimer for useful discussions about the evolution of $\Omega_{C^{+3}}$ and the effects of cosmology. This study is based on observations made with the NASA-CNES-CSA *Far Ultraviolet Spectroscopic Explorer*. *FUSE* is operated for NASA by the Johns Hopkins University under NASA contract NAS5-32985. This work is also based on observations made with the NASA/ESA *Hubble Space Telescope* Space Telescope Imaging Spectrograph and Goddard High-Resolution Spectrograph, obtained from the data archive at the Space Telescope Institute. STScI is operated by the association of Universities for Research in Astronomy, Inc. under the NASA contract NAS 5-26555. The current study was funded by the HST archival grant 10679 and the NSF CAREER grant AST 05_48180.

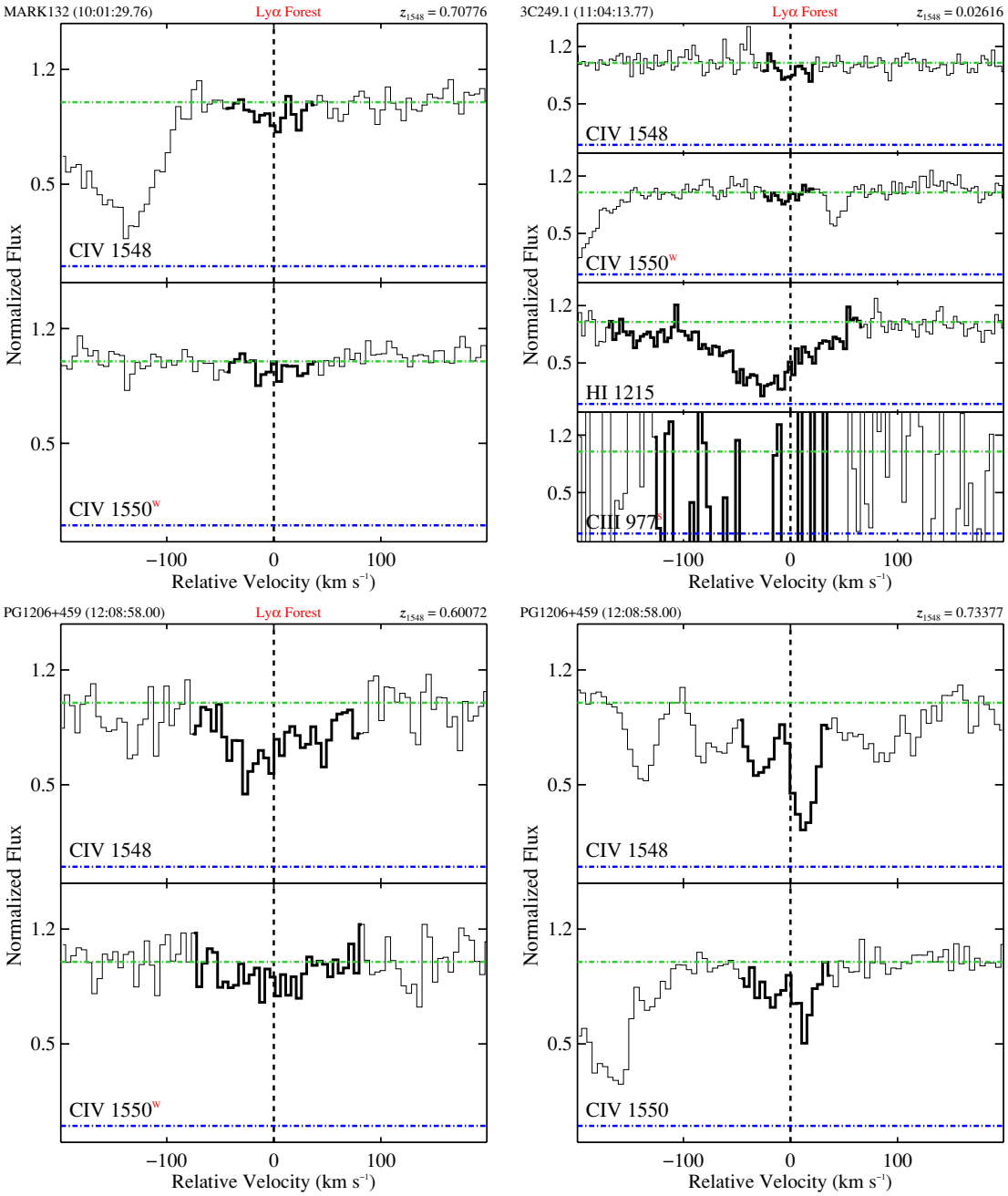

Figure 18. (Continued)

APPENDIX A

VELOCITY PLOTS

The velocity plots for G = 1 and 2 C IV systems are shown in Figures 17 and 18, respectively.

APPENDIX B

MAXIMUM LIKELIHOOD ANALYSIS

We used the maximum likelihood method to fit the frequency distributions with a power-law function. For this discussion, we will focus primarily on deriving the maximum likelihood function for the column densities, where one must account for lower limits due to saturation effects. Saturation obviously does not occur for the equivalent width measurements, and the maximum likelihood function $\mathcal{L}$ derived here reduces to a formalism applicable to W_r. The following derivation draws heavily from Storrie-Lombardi et al. (1996).

Assuming Poisson counting statistics, the probability of detecting $\mathcal{N}(N_i)$ absorbers with column densities N_i is determined by the Poisson probability distribution:

$$P(\mathcal{N}(N_i);\mu_i) = e^{-\mu_i}\frac{\mu_i^{\mathcal{N}(N_i)}}{\mathcal{N}(N_i)!}, \quad \text{(B1)}$$

where μ_i is the expected number, based on the parent distribution. The likelihood function is defined as the product of the probability of observing each absorber with N_i:

$$\mathcal{L} = \prod_i^{\mathcal{N}} P(\mathcal{N}(N_i);\mu_i) = \prod_i^{\mathcal{N}} e^{-\mu_i}\frac{\mu_i^{\mathcal{N}(N_i)}}{\mathcal{N}(N_i)!}. \quad \text{(B2)}$$

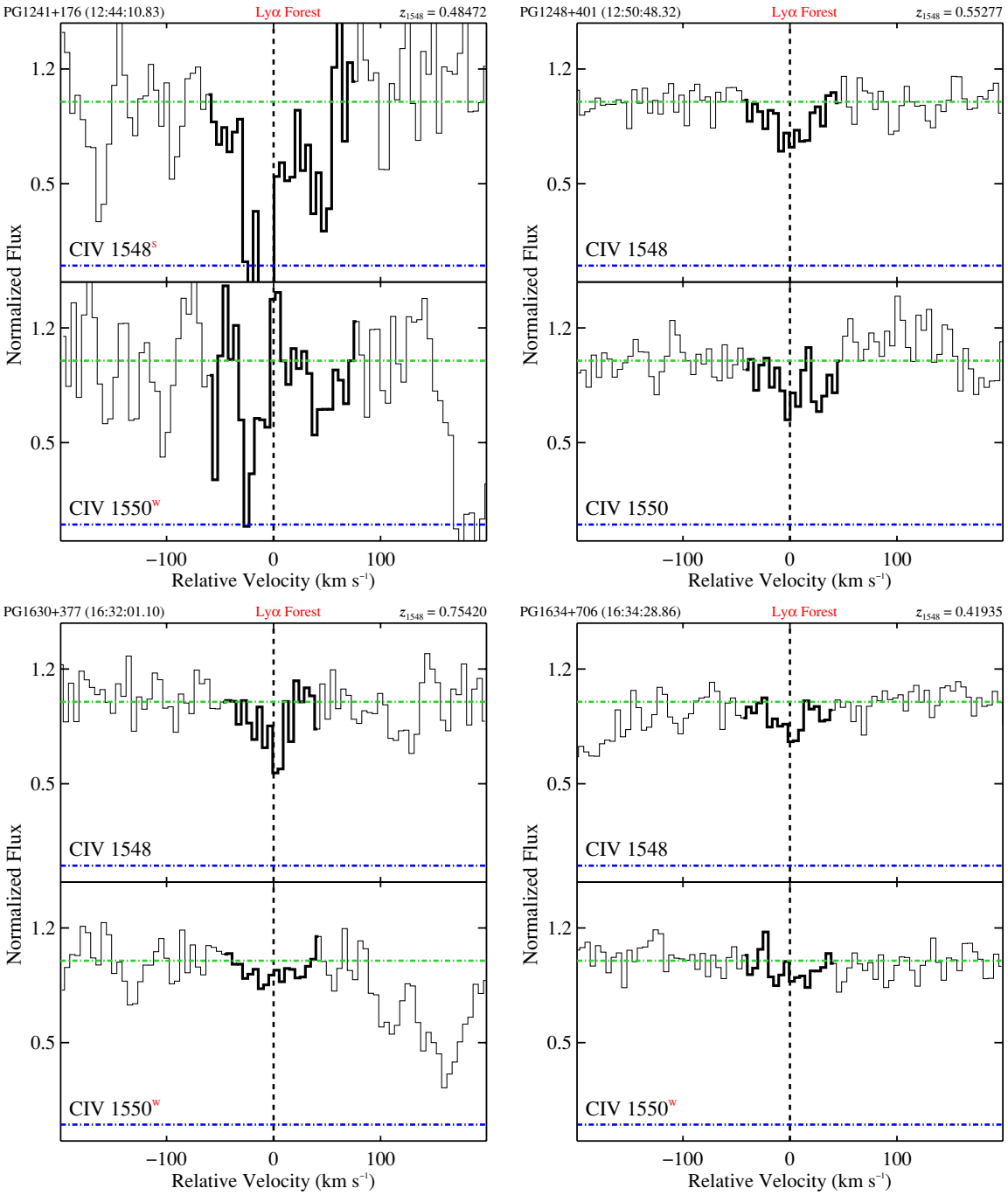

Figure 18. (Continued)

Assume that the expected number μ_i depends on the frequency distribution:

$$\mu_i = f(N_i)\,\Delta X(N_i)\,\Delta N_i \tag{B3}$$

(see Equation (11)). Then, consider the limit where the "volume" $\Delta X(N_i)\,\Delta N_i$ contains at most one absorber. With $\mathcal{N} = p$ (single-detection) $+g$ (no-detection) volumes:

$$\ln \mathcal{L} = -\int_{N_{\rm min}}^{N_{\rm max}} f(N_i)\Delta X(N_i) dN_i + \sum_i^p \ln\left(f(N_i)\Delta X(N_i)\right), \tag{B4}$$

in the limit where $\Delta N_i \rightarrow 0$ ($\Delta X(N_i)$ is essentially a weight and cannot shrink to zero for all N_i).

However, our absorbers include column density measurements where we have only a lower limit on $N_i \geqslant N_{\rm sat}$. We need a probability for detecting q saturated absorbers above the saturation limit $N_{\rm sat} = 10^{14.3}\,{\rm cm}^{-2}$, $P(q;\mu_i')$. Thus, the likelihood function becomes

$$\mathcal{L} = \left(\prod_i^{\mathcal{N}} e^{-\mu_i}\frac{\mu_i^{\mathcal{N}(N_i)}}{\mathcal{N}(N_i)!}\right) P(q;\mu_i'). \tag{B5}$$

The mean number of saturated absorbers is expected to be

$$\mathcal{N}_{\rm sat} = \int_{N_{\rm sat}}^{\infty} f(N_i)\Delta X(N_i) dN_i. \tag{B6}$$

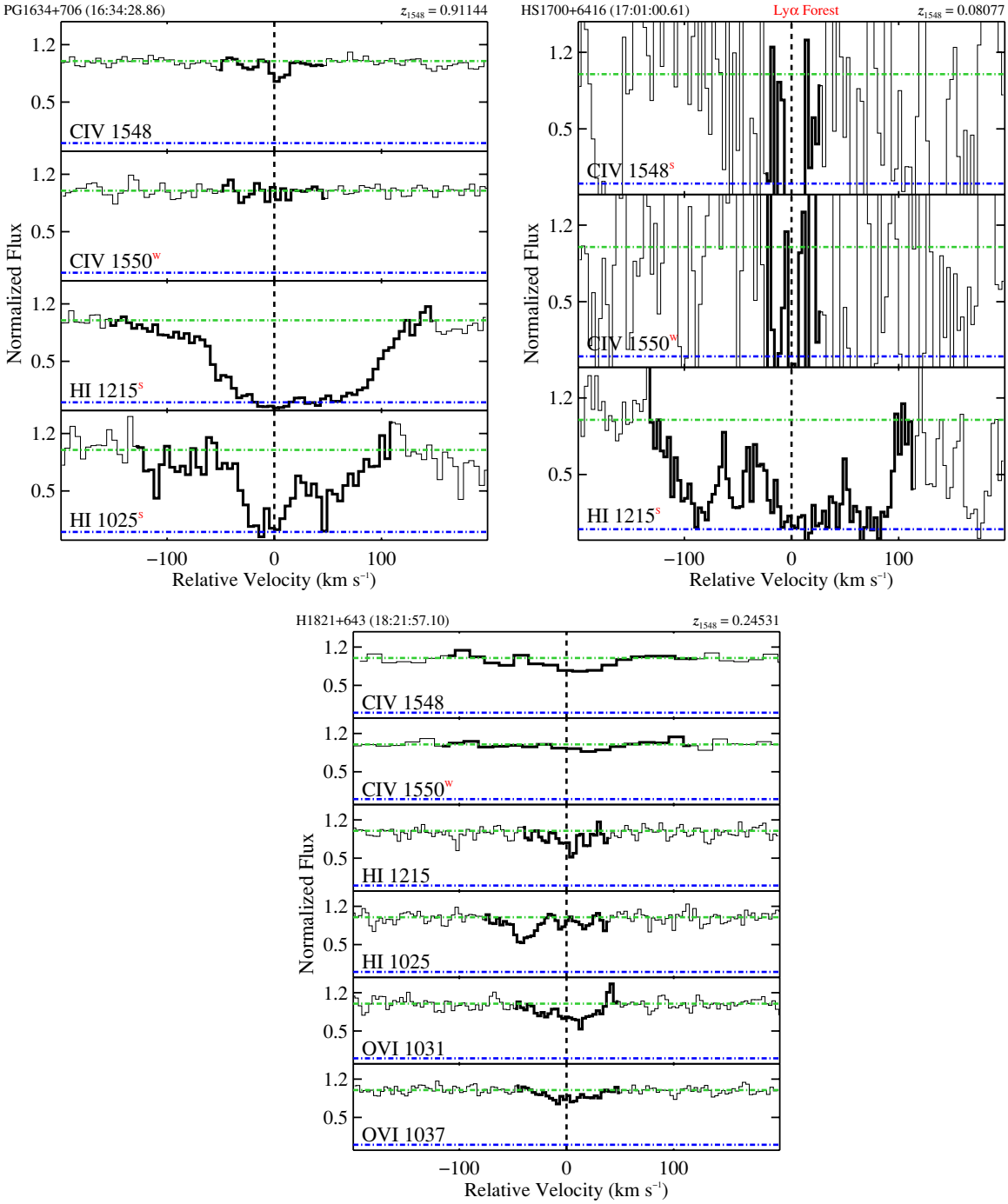

Figure 18. (Continued)

Let $\mu_i' = \mathcal{N}_{\rm sat}$, the expected number of saturated absorbers from the integral of $f(N_i)$ between $N_{\rm sat}$ and infinity. Thus, taking the natural logarithm and expanding Equation (B5) reduces to

$$\ln \mathcal{L} = -\int_{N_{\rm min}}^{N_{\rm max}} f(N_i)\Delta X(N_i) dN_i - \int_{N_{\rm sat}}^{\infty} f(N_i)\Delta X(N_i) dN_i + \sum_{i}^{p} \ln\left(f(N_i)\Delta X(N_i)\right) + q\,\ln\left(\int_{N_{\rm sat}}^{\infty} f(N_i)\Delta X(N_i) dN_i\right). \quad \text{(B7)}$$

Substituting the power-law form of $f(N(C^{+3}))$ (see Equation (13)) provides the maximum likelihood function used in the current study.

APPENDIX C

ADJUSTING C^{+3} MASS DENSITY

In order to compare $\Omega_{C^{+3}}$ from the current study to other studies, we had to account for differences in cosmology and range of $N(C^{+3})$ included in the measurement. Changing the adopted Hubble constant H_0 is a simple matter of scaling $\Omega_{C^{+3}}$ by the ratio of the old H_0 to the new (see Equation (19); recall that $\rho_{c,0} \propto H_0^2$ and ΔX is independent of H_0). Less simple is adjusting for changes in $\Omega_{\rm M}$ and Ω_Λ, since that enters the

computation of $\Omega_{C^{+3}}$ in the estimate of the co-moving path length ΔX (see Equation (9)). Previous authors have frequently scaled the *summed* $\Omega_{C^{+3}}$ by the ratio of the new path length to the old as follows:

$$\frac{\Omega_{C^{+3},\mathrm{new}}}{\Omega_{C^{+3},\mathrm{old}}} = \frac{H_{0,\mathrm{old}}\frac{dX}{dz}(\langle z\rangle; \Omega_{M,\mathrm{old}}, \Omega_{\Lambda,\mathrm{old}})}{H_{0,\mathrm{new}}\frac{dX}{dz}(\langle z\rangle; \Omega_{M,\mathrm{new}}, \Omega_{\Lambda,\mathrm{new}})}, \quad \text{(C1)}$$

where dX/dz is the derivative of Equation (9) evaluated at the median redshift $\langle z\rangle$ and with the appropriate cosmology.

This adjustment is an approximation because ΔX is the sum of parts of spectra that satisfy the redshift and column density constraints (see Equation (10)). Therefore, to correctly adjust for cosmology, each snippet δX must be calculated in the desired cosmology and then added together to re-estimate ΔX. Most published studies do not provide the necessary information to do this, which is why the above equation is the standard adjustment. However, the approximation works well when the redshift bin is small. For values quoted in the text and Figures 13 and 15, we use Equation (C1) to adjust for differences in cosmology.

For most of the studies, the adjustment is small since their adopted cosmology and ours were similar. The results of Songaila (2001) and Pettini et al. (2003) were decreased by ≈55%, since they adopted an Einstein-de Sitter cosmology (EdS) with $H_0 = 65\,\mathrm{km\,s^{-1}\,Mpc^{-1}}$, $\Omega_M = 1$, and $\Omega_\Lambda = 0$. Since we cannot correctly compute their results precisely for our adopted cosmology, we calculated our $\Omega_{C^{+3}}$ in their cosmology, by re-constructing $\Delta X(N(C^{+3}))$ and re-calculating the summed $\Omega_{C^{+3}}$. The difference between the values quoted in Table 6 and our EdS $\Omega_{C^{+3}}$ adjusted by Equation C1 is <8% for the full sample. Thus, Equation (C1) adequately adjusts for differences in cosmology when applied to summed values of $\Omega_{C^{+3}}$.[25]

The column density limits used in the summed $\Omega_{C^{+3}}$ estimation was the other factor we considered when adjusting the values from other studies. As mentioned in Section 5.3, the high column density doublets contain the majority of the mass and dominate the C^{+3} mass density. Since there has been no break in the frequency distribution, we limited the integrated $\Omega_{C^{+3}}$ measurement to $13 \leqslant \log N(C^{+3}) \leqslant 15$. However, Scannapieco et al. (2006) estimated $\Omega_{C^{+3}} = (7.54 \pm 2.16) \times 10^{-8}$ by summing their observed doublets with $12 \leqslant \log N(C^{+3}) \leqslant 16$. To fairly compare their result with the current survey, their measured value was decreased by 45%. This factor was determined by assuming their summed $\Omega_{C^{+3}}$ scaled as the integrated $\Omega_{C^{+3}}$:

$$\frac{\Omega_{C^{+3},\mathrm{new}}}{\Omega_{C^{+3},\mathrm{old}}} = \frac{N_{\mathrm{max,new}}^{2+\alpha_N} - N_{\mathrm{min,new}}^{2+\alpha_N}}{N_{\mathrm{max,old}}^{2+\alpha_N} - N_{\mathrm{min,old}}^{2+\alpha_N}}, \quad \text{(C2)}$$

where the new column density limits are $13 \leqslant \log N(C^{+3}) \leqslant 15$, to match the current work, and α_N is the value measured by the "old" study (also see Equation (22)). For Scannapieco et al. (2006), the best-fit $\alpha_N = -1.8$. We also made adjustments (<30%) to Songaila (2001), Pettini et al. (2003), Boksenberg et al. (2003), and Danforth & Shull (2008) since $N_{\mathrm{min}} < 10^{13}\,\mathrm{cm^{-2}}$ in their studies and, for most, $N_{\mathrm{max}} < 10^{15}\,\mathrm{cm^{-2}}$, which increases the significance of the lower column density absorbers.

We did *not* extrapolate these studies and change N_{max}. These surveys were surely sensitive to doublets with $\log N(C^{+3}) > 14$, but they did not survey a sufficiently large path length to encounter them, since they are rare. The affect of path length is accounted for in the summed $\Omega_{C^{+3}}$ (Equation (20)), where it essentially weights the sum of the column densities. Therefore, for these studies, the summed $\Omega_{C^{+3}}$ values occasionally reflect the fact that the strongest absorbers are rare, though they dominate the C^{+3} mass density.

The result from Ryan-Weber et al. (2009) could have been increased by a factor of 1.4, assuming $\alpha_N = -1.8$ (less for a shallower power law); they were only sensitive to doublets with $13.8 \leqslant \log N(C^{+3}) \leqslant 15$. However, we did not adjust their value since we did not know the appropriate slope and did not include the highest redshift measurements in the linear regressions to $\Omega_{C^{+3}}$ over t_{age}.

The total adjustment for cosmology and/or column density limits for the $z > 1$ studies cited in this paper are as follows: ≈40%, Songaila (2001); 38%, Pettini et al. (2003); 81%, Boksenberg et al. (2003); 45%, Scannapieco et al. (2006); 92%, Danforth & Shull (2008); and 105%, Becker et al. (2009).

APPENDIX D

DETAILED COMPARISON WITH MILUTINOVIC ET AL. (2007) AND DANFORTH & SHULL (2008)

Milutinović et al. (2007) and Danforth & Shull (2008) surveyed archival STIS E230M and E140M spectra, respectively, for intergalactic absorption lines. It is useful, therefore, to compare their results with our own as a consistency check.[26]

In general, our search algorithms and sample selection were consistent with Milutinović et al. (2007) and Danforth & Shull (2008), who used different procedures. The current survey, however, has the advantage of analyzing the largest sample of $z_{1548} < 1$ sightlines in a consistent fashion.

D.1. Milutinović et al. (2007)

Milutinović et al. (2007) focused on eight sightlines with STIS E230M observations and compiled comprehensive line lists for each sightline. There were 24 C IV systems in their survey. We agreed with 19 of these, including the associated transitions (e.g., Lyα, Si II 1260), though we did not search for all of the transitions that they did (e.g., C II 1334, Fe II 1608). We counted the DLA $z_{1548} = 0.92677$ C IV doublet toward PG1206+459 as one system, while Milutinović et al. (2007) divided it into two. Three of the remaining five systems are acknowledged to be questionable identifications by Milutinović et al. (2007) and were not included in our G = 1+2 group at all. Of the other two, the reported doublet at $z_{1548} = 0.7760$ toward PG1248+401 does not show up in our survey because the 1548 line was blended and the 1550 would not be detected with $W_{r,1550} \geqslant 3\sigma_{W_r}$. The other unconfirmed doublet at $z_{1548} = 0.9903$ toward PG1634+706 was associated with the Mg II absorber, which was the motive for observing the sightline (see Section 6.4). This doublet would lie in the highest-wavelength order of the E230M spectrum, which we excluded due to questionable data quality flags.

[25] Using Equation (C1) to adjust our EdS, *integrated* $\Omega_{C^{+3}}$ values introduces errors up to 25%.

[26] Frye et al. (2003) was a conference proceeding, which we do not discuss in detail. To summarize, they surveyed nine sightlines with STIS E140M spectra. We agreed with seven of their nine identified C IV doublets. Though we agreed well with their $d\mathcal{N}_{C\,IV}/dz$ over equivalent width limit, their reported $\Omega_{C^{+3}}$ value was almost double our value for the $z < 0.6$ sample. However, this is likely due to small number statistics, since we agreed ($<1\sigma$) when we focused just on the E140M data (see Table 6).

Considering the opposite comparison, we identified 29 C IV doublets in the eight sightlines that Milutinović et al. (2007) also analyzed. Of these, 11 were identified as other transitions by Milutinović et al. (2007). In nine cases, the absorption lines we list as C IV doublets were either: listed as tentative Lyα lines; not identified; or not listed at all. The two remaining disputed cases are the ones we identify as $z_{1548} = 0.48472$ toward PG1241+176 and $z_{1548} = 0.55277$ toward PG1248+401, both G = 2 doublets. For the PG1241+176 lines, Milutinović et al. (2007) identifies our 1548 line as O VI 1037 at $z = 1.2142$ and 1550 as a tentative Lyα line. The 1548 profile is consistent with being blended, so we conclude that both identifications are valid. For the PG1248+401 lines, Milutinović et al. (2007) lists our 1548 line as Lyα absorption, with no associated transitions, and does not list our 1550 line, which we detect at $>3\sigma_{W_r}$. We stand by our identification and accept the possibility that the $z_{1548} = 0.55277$ doublet is Lyα contamination, as discussed in Section 4.3.

D.2. Danforth & Shull (2008)

Danforth & Shull (2008) focused on 28 sightlines with STIS E140M observations and supplementary *FUSE* spectra. They conducted a Lyα-targeted survey, where they identified Lyα absorbers first, then searched for other, associated intergalactic transitions (e.g., Lyβ, C III). They detected 24 $z_{1548} < 0.12$ C IV doublets with at least one line detected at $\geqslant 4\sigma_{W_r}$ so long as R_W was consistent (see Section 3.2). For a total path length $\Delta z = 2.42$, they measured $d\mathcal{N}_{\rm C\,IV}/dz = 10^{+4}_{-2}$ for $W_r \geqslant 30$ mÅ. They also fit a power law to $d\mathcal{N}_{\rm C\,IV}/dz$ in bins of $\Delta \log N({\rm C}^{+3}) = 0.2$; the best-fit exponent was $\alpha_N = -1.79 \pm 0.17$. They measured a summed $\Omega_{\rm C^{+3}} = (7.78 \pm 1.47) \times 10^{-8}$ for $12.83 \leqslant \log N({\rm C}^{+3}) \leqslant 14.13$.

The current survey included the same 28 sightlines though not all of the *FUSE* data, since some had S/N too low for continuum fitting. Of the 24 doublets in Danforth & Shull (2008), we detected nine also and could neither agree or disagree with three, which were detected in the zeroth order of the STIS E140M spectra, which we did not include due to questionable data quality flags. The zeroth order covered 1711 Å $< \lambda <$ 1729 Å (or $0.105 < z < 0.115$), and the sensitivity of the E140M spectra drops rapidly at $\lambda > 1700$ Å. Therefore, we would not likely have included any doublets in the zeroth order in our analysis, since both lines were not detected with $W_r \geqslant 3\sigma$ in Danforth & Shull (2008).

Of the remaining 11 doublets, two toward NGC7469 were excluded from our sample because they were within 3000 km s^{-1} of the background source. The other nine either did not look like absorption lines or the C IV 1548 line did not have $W_{r,1548} \geqslant 3\sigma_{W_r}$ in our co-added and normalized spectra. As discussed in Cooksey et al. (2008), Danforth & Shull (2008) cited questionably small errors (<5%) for their rest equivalent widths, which led them to consider more lines to be detected at a given significance level.

We detected 12 C IV doublets in the E140M spectra, that includes three doublets not cited in Danforth & Shull (2008). For two cases, we identified the absorption lines as G = 2 C IV doublets with only the 1548 line detected with $W_{r,1548} \geqslant 3\sigma_{W_r}$: $z_{1548} = 0.02616$ toward 3C249.1[27] and $z_{1548} = 0.08077$ toward HS1700+6416. These doublets were not included in our analyses. The last case was the G = 1, $z_{1548} = 0.00574$ doublet toward QSO–123050+011522, which was also associated with a Si IV doublet (another target absorption lines of their study). They did not detect this doublet because the Lyβ line was contaminated by a spurious artifact in the *FUSE* spectra, but they now agree with our identification (C. Danforth 2009, private communication)

Facilities: FUSE, *HST* (STIS), *HST* (GHRS)

[27] Danforth & Shull (2008) identified the $\geqslant 3\sigma_{W_r}$ absorption line (that we list as C IV 1548) as Lyα at $z = 0.30788$, which was their default identification for single lines.

REFERENCES

Aguirre, A., Hernquist, L., Schaye, J., Katz, N., Weinberg, D. H., & Gardner, J. 2001, ApJ, 561, 521
Bahcall, J. N., et al. 1993, ApJS, 87, 1
Barlow, T. A., & Tytler, D. 1998, AJ, 115, 1725
Becker, G. D., Rauch, M., & Sargent, W. L. W. 2009, ApJ, 698, 1010
Boksenberg, A., Sargent, W. L. W., & Rauch, M. 2003, arXiv:astro-ph/0307557
Brandt, J. C., et al. 1994, PASP, 106, 890
Chen, H.-W., Lanzetta, K. M., & Webb, J. K. 2001, ApJ, 556, 158
Churchill, C. W., & Le Brun, V. 1998, ApJ, 499, 677
Churchill, C. W., Mellon, R. R., Charlton, J. C., Jannuzi, B. T., Kirhakos, S., Steidel, C. C., & Schneider, D. P. 1999a, ApJ, 519, L43
Churchill, C. W., Mellon, R. R., Charlton, J. C., Jannuzi, B. T., Kirhakos, S., Steidel, C. C., & Schneider, D. P. 2000, ApJ, 543, 577
Churchill, C. W., Rigby, J. R., Charlton, J. C., & Vogt, S. S. 1999b, ApJS, 120, 51
Churchill, C. W., & Vogt, S. S. 2001, AJ, 122, 679
Cooksey, K. L. 2009, PhD thesis, Univ. California (Santa Cruz)
Cooksey, K. L., Prochaska, J. X., Chen, H.-W., Mulchaey, J. S., & Weiner, B. J. 2008, ApJ, 676, 262
Cowie, L. L., Songaila, A., Kim, T.-S., & Hu, E. M. 1995, AJ, 109, 1522
Cui, J., Bechtold, J., Ge, J., & Meyer, D. M. 2005, ApJ, 633, 649
Danforth, C. W., & Shull, J. M. 2008, ApJ, 679, 194
Ellison, S. L., Lewis, G. F., Pettini, M., Chaffee, F. H., & Irwin, M. J. 1999, ApJ, 520, 456
Ellison, S. L., Mallén-Ornelas, G., & Sawicki, M. 2003, ApJ, 589, 709
Ellison, S. L., Songaila, A., Schaye, J., & Pettini, M. 2000, AJ, 120, 1175
Fernández-Soto, A., Lanzetta, K. M., Barcons, X., Carswell, R. F., Webb, J. K., & Yahil, A. 1996, ApJ, 460, L85
Frye, B. L., Tripp, T. M., Bowen, D. B., Jenkins, E. B., & Sembach, K. R. 2003, in Astrophysics and Space Science Library 281, The IGM/Galaxy Connection: The Distribution of Baryons at $z = 0$, ed. J. L. Rosenberg & M. E. Putman (Dordrecht: Kluwer), 231
Janknecht, E., Reimers, D., Lopez, S., & Tytler, D. 2006, A&A, 458, 427
Kim, T.-S., Cristiani, S., & D'Odorico, S. 2001, A&A, 373, 757
Lanzetta, K. M., McMahon, R. G., Wolfe, A. M., Turnshek, D. A., Hazard, C., & Lu, L. 1991, ApJS, 77, 1
Madau, P., Ferrara, A., & Rees, M. J. 2001, ApJ, 555, 92
Madau, P., & Haardt, F. 2009, ApJ, 693, L100
Milutinović, N., et al. 2007, MNRAS, 382, 1094
Misawa, T., Tytler, D., Iye, M., Storrie-Lombardi, L. J., Suzuki, N., & Wolfe, A. M. 2002, AJ, 123, 1847
Mobasher, B. 2002, in *HST* Data Handbook: Introduction to Reducing *HST* Data, Vol. 1, Version 4.0 (User's Guide, Hubble Space Telescope, 2002 January), ed. B. Mobasher (Baltimore: Space Telescope Science Institute), http://www.stsci.edu/hst/HST-overview/documents/datahandbook/
Oppenheimer, B. D., & Davé, R. 2006, MNRAS, 373, 1265
Oppenheimer, B. D., & Davé, R. 2008, MNRAS, 387, 577
Petitjean, P., & Bergeron, J. 1994, A&A, 283, 759
Pettini, M., Madau, P., Bolte, M., Prochaska, J. X., Ellison, S. L., & Fan, X. 2003, ApJ, 594, 695
Prochaska, J. X., Chen, H.-W., Howk, J. C., Weiner, B. J., & Mulchaey, J. 2004, ApJ, 617, 718
Rauch, M., Sargent, W. L. W., Womble, D. S., & Barlow, T. A. 1996, ApJ, 467, L5
Ryan-Weber, E. V., Pettini, M., & Madau, P. 2006, MNRAS, 371, L78
Ryan-Weber, E. V., Pettini, M., Madau, P., & Zych, B. J. 2009, MNRAS, 395, 1476
Savage, B. D., & Sembach, K. R. 1991, ApJ, 379, 245
Scannapieco, E., Ferrara, A., & Madau, P. 2002, ApJ, 574, 590
Scannapieco, E., Pichon, C., Aracil, B., Petitjean, P., Thacker, R. J., Pogosyan, D., Bergeron, J., & Couchman, H. M. P. 2006, MNRAS, 365, 615
Schaye, J., Aguirre, A., Kim, T.-S., Theuns, T., Rauch, M., & Sargent, W. L. W. 2003, ApJ, 596, 768
Schaye, J., Carswell, R. F., & Kim, T.-S. 2007, MNRAS, 379, 1169

Schaye, J., et al. 2009, arXiv:0909.5196
Simcoe, R. A. 2006, ApJ, 653, 977
Simcoe, R. A., Sargent, W. L. W., & Rauch, M. 2004, ApJ, 606, 92
Songaila, A. 2001, ApJ, 561, L153
Songaila, A. 2005, AJ, 130, 1996
Songaila, A. 2006, AJ, 131, 24
Springel, V., & Hernquist, L. 2003, MNRAS, 339, 289
Steidel, C. C. 1990, ApJS, 72, 1
Storrie-Lombardi, L. J., Irwin, M. J., & McMahon, R. G. 1996, MNRAS, 282, 1330
Tytler, D., Fan, X.-M., Burles, S., Cottrell, L., Davis, C., Kirkman, D., & Zuo, L. 1995, in QSO Absorption Lines, ed. G. Meylan (New York: Springer), 289
Wise, J. H., & Abel, T. 2008, ApJ, 685, 40